SYNCHRONIZATION IN ALL-DIGITAL QAM RECEIVERS

A Dissertation Submitted
to the College of Graduate Studies and Research
in Partial Fulfillment of the Requirements
for the Degree of Doctor of Philosophy
in the Department of Electrical & Computer Engineering
University of Saskatchewan

by

Eric R. Pélet

Saskatoon, Saskatchewan, Canada

PERMISSION TO USE

In presenting this dissertation in partial fulfillment of the requirements for a Post-graduate degree from the University of Saskatchewan, it is agreed that the Libraries of this University may make it freely available for inspection. Permission for copying of this dissertation in any manner, in whole or in part, for scholarly purposes may be granted by the professors who supervised this dissertation work or, in their absence, by the Head of the Department of Electrical & Computer Engineering or the Dean of the College of Graduate Studies and Research at the University of Saskatchewan. Any copying, publication, or use of this dissertation, or parts thereof, for financial gain without the written permission of the author is strictly prohibited. Proper recognition shall be given to the author and to the University of Saskatchewan in any scholarly use which may be made of any material in this dissertation.

Request for permission to copy or to make any other use of material in this dissertation in whole or in part should be addressed to:

Head of the Department of Electrical & Computer Engineering
57 Campus Drive
University of Saskatchewan
Saskatoon, Saskatchewan, Canada
S7N 5A9

ABSTRACT

The recent advance in Field Programmable Gate Array (FPGA) technology has been largely embraced by the communication industry, which views this technology as an effective and economical alternative to the design of Application Specific Integrated Circuits (ASICs). The primary reasons for switching to FPGAs are lower development and non-recurring engineering costs, the flexibility to design to a preliminary standard and adapt the design as the standard evolves, as well as the option of performing software updates in the field.

A sector with strong interest in FPGAs is the coaxial cable TV/Internet distribution industry. The creation of soft preliminary standards by the standards organization governing the industry has been the main catalyst for the massive adoption of FPGAs by small to medium size companies, which see this technology as an opportunity to compete in this open market.

Both the circuit speed and the economy of FPGA technology depend upon using algorithms that map efficiently into its fabric. Often it is prudent to sacrifice performance to improve either clock speed or economy when developing with FPGAs. The purpose of this research is to both revise and devise synchronization algorithms / structures for cable digital receivers that are to be implemented in FPGA.

The main communication scheme used by the coaxial cable distribution industry is digital Quadrature Amplitude Modulation (QAM). The problem of synchronizing to the QAM signal in the receiver is not a new topic and several synchronization-related circuits, which were devised with ASICs implementation in mind, can be found in the open literature. Of interest in this thesis is the non-data-aided digital timing synchronizer that was proposed by D'Andrea to recover timing with no knowledge of the transmitted data. Accurate timing estimation was achieved by reshaping the received signal with a prefilter prior to estimating the timing.

A problem with D'Andrea's synchronizer is that the prefilter for reshaping the signal is a relatively long Finite Impulse Response (FIR) filter, whose implementation requires a large number of multipliers. This may not have been an issue with ASICs in as much as the number of hardwired multipliers on a chip is not limited as it is in an FPGA chip. One contribution in this research is to propose an alternative to D'Andrea's synchronizer by replacing the long FIR filter with two single-pole Infinite Impulse Response (IIR) filters that are directly placed inside the timing recovery loop. This novel architecture, which drastically reduces the number of multipliers, is well suited for FPGA implementation.

Non-data-aided feedforward synchronizers, which use the same prefilter as D'Andrea's synchronizer, have been receiving significant attention in recent years. Detailed performance analysis for these synchronizers can be found in the open literature. These synchronizers have the advantage of using a feedfordward structure rather than a feedback structure, as it is the case in D'Andrea's synchronizer, to estimate the timing. While D'Andrea's synchronizer has an advantage in performance over a non-data-aided feedforward synchronizer, this has not been reported in the literature. In this thesis a second contribution consists of thoroughly analyzing the steady state timing jitter in D'Andrea synchronizer by deriving a closed-form expression for the noise power spectrum and a simple equation to estimate the timing jitter variance.

A third contribution is a novel low-complexity and fast acquisition coherent detector for the detection of Quadrature Phase Shift Keying (QPSK) (i.e., 4-QAM) symbols. This detector performs carrier phase synchronization much faster than a conventional coherent detector. The acquisition time is comparable to that of a differential detector. The fast acquisition comes at the expense of phase jitter, and the end result is a 1 dB performance loss over theoretical coherent detection. This detector can be used in place of the differential detector with no economic penalty. Doing so yields a performance advantage of about 2 dB over differential detection.

ACKNOWLEDGMENTS

First and foremost I would like to express my heart-felt gratitude to my supervisor, Professor J. Eric Salt, for his excellent guidance and tremendous support during my years of study at the University of Saskatchewan. I will remember the thoughtful discussions we had that guided me throughout my Ph.D. research and strongly influence both my thinking and writing. It has been a great privilege and rewarding experience to work under Professor J. Eric Salt.

I would like to extend my deepest gratitude to Professor B. Daku and Professor H. Nguyen from the Department of Electrical and Computer Engineering, as well as Professor M. Bradley from the Department of Physics and Engineering Physics for serving as members of my Ph.D. advisory committee and providing me with valuable comments.

Finally I would like to thank the Natural Sciences and Engineering Research Council (NSERC) and the University of Saskatchewan for providing me with generous fellowships and scholarships. I also wish to thank Telecommunications Research Laboratories (TRLabs) for the financial help and resources they offered me during my pursuit of both the M.Sc. and Ph.D. degrees at the University of Saskatchewan.

To my parents, Jean and Rirette Pélet,

to my wife, **Patricia Karen Pélet**,

and our children,

Camille and Emmarie.

TABLE OF CONTENTS

LIST OF FIGURES

LIST OF ABBREVIATIONS

AWGN	Additive White Gaussian Noise
ASIC	Application Specific Integrated Circuit
BPSK	Binary Phase Shift Keying
CATV	CAble TV
CRB	Cramer-Rao Bound
D/A	Digital-to-Analog converter
DSP	Digital Signal Processing
DTFT	Discrete-Time Fourier Transform
FIR	Finite Impulse Response
FPGA	Field Programmable Gate Array
HDL	Hardware Descriptive Language
I	In-phase
IC	Integrated Circuit
IF	Intermediate Frequency
IIR	Infinite Impulse Response
ISI	InterSymbol Interference
LF	Likelihood Function
LPF	Low-Pass Filter
MCRB	Modified Cramer-Rao Bound
MF	Matched Filter
ML	Maximum Likelihood
MLE	Maximum Likelihood Estimator
PAM	Pulse Amplitude Modulation
PD	Phase Detector
PDF	Probability Density Function

PLL	Phase-Locked Loop
PSD	Power Spectral Density
Q	Quadrature
QAM	Quadrature Amplitude Modulation
QPSK	Quadrature Phase Shift Keying
RAM	Random Access Memory
RF	Radio Frequency
RV	Random Variable
SNR	Signal-to-Noise Ratio
TED	Timing-Error Detector
VCO	Voltage-Controlled Oscillator
VOD	Video-On-Demand

1. Introduction

Digital communication involves sending digital information over some medium. There are basically four types of media to convey the information electrically: twisted pair, coaxial cable, fiber, and air (i.e., wireless transmission). The medium of interest is coaxial cable, where digital Quadrature Amplitude Modulation (QAM) is the most efficient and widely used communication scheme. In this research synchronization-related circuits for various digital QAM systems are devised. The particularity of the QAM system of interest is that the processing in the receiver is done digitally as explained next.

1.1 A QAM system using an all-digital receiver

A communication system comprises a transmitter and a receiver. The transmitter is described first. Description of the receiver follows.

A block diagram of the transmitter is shown in Figure 1.1. The transmitted signal is generated digitally by modulating the amplitude of two digital carriers, $\cos[2\pi f_0 n]$ and $\sin[2\pi f_0 n]$, that are in quadrature. In the digital domain the carrier frequency, f_0, has units of cycles/sample. The quadrature signals are summed and converted to analog with a digital-to-analog (D/A) converter.

The digital low-pass signals, $x_I[n]$ and $x_Q[n]$, modulating the carriers are referred to as the in phase and quadrature signals. Both signals have the same structure in that they are made of a train of signaling Nyquist's pulses [1] whose peak amplitudes take different values to encode the binary data to be transmitted.

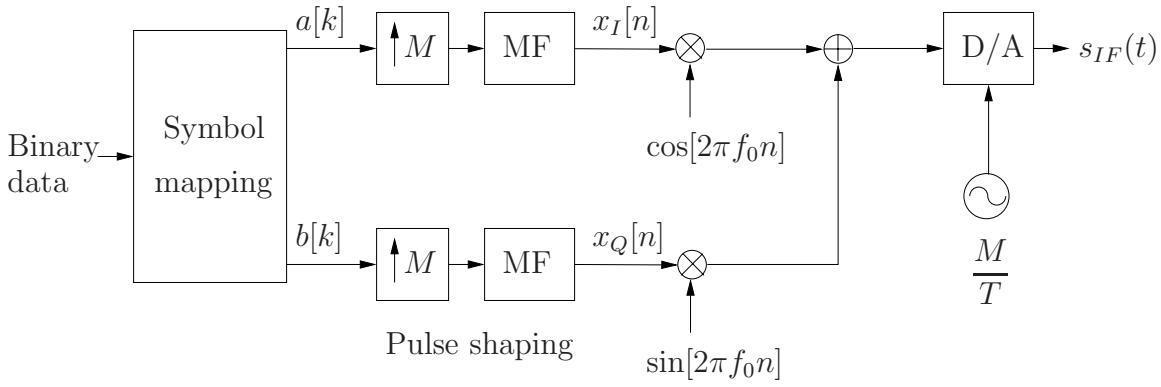

Figure 1.1 Digital QAM transmitter block diagram.

The encoding is done by converting the input binary data stream into symbols. A symbol is a 2-tuple, $(a[k], b[k])$, whose elements represent discrete amplitude levels for the pulses. In 64-QAM there are 8 discrete levels so 64 different symbols are available for encoding the data. The conversion to symbols is performed 6 bits at a time. Each 2-tuple (i.e., symbol) gives rise to the transmission of a pair of signaling pulses: one pulse whose peak amplitude is equal to $a[k]$ is carried by the in phase signal, and a second pulse whose peak amplitude is equal to $b[k]$ is carried by the quadrature signal.

The process to generate $x_I[n]$ and $x_Q[n]$ consists of first upsampling $a[k]$ and $b[k]$ by M to set the interval of time between the pulses to M samples, and then passing the upsampled signals through pulse shaping filters known as Matched Filters (MF). The interval of time between pulses when expressed in seconds is referred to as the symbol interval. It is equal to M times the period of the D/A clock. For a D/A clock of M/T samples per second, the symbol interval is T seconds.

Following digital-to-analog conversion, the analog signal is at an intermediate frequency (IF) of $f_0 \times M/T$ Hz. It is upconverted to the frequency band of interest for the actual transmission over cable. Several sources of noise corrupt the transmitted signal. In this research the noise is modeled as Additive White Gaussian Noise (AWGN). In addition to noise, the signal experiences distortions that are caused by

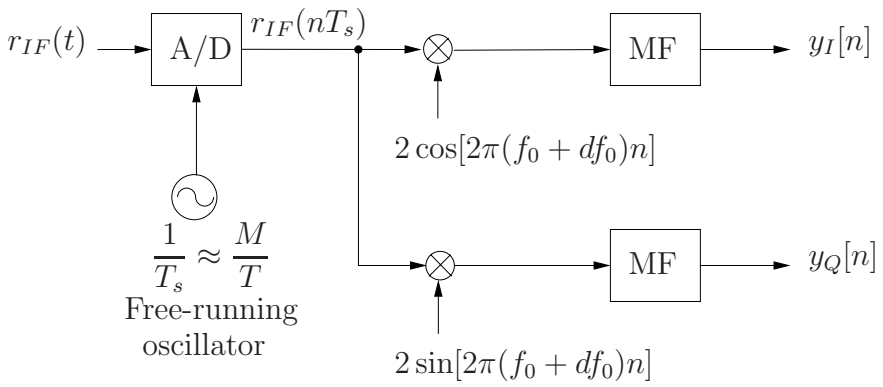

Figure 1.2 All-digital QAM receiver front-end block diagram.

the medium. For example signal fading is very common in wireless transmissions. In cable transmissions the signal distortions are relatively small. The spectrum is channelized with sufficiently small bandwidths that the frequency response of the channel is nearly flat and the channel can be modeled as a delay.

The RF received signal is downconverted to IF and passed to an all-digital receiver for signal sampling and recovery of the transmitted symbols. A block diagram of the front-end of the receiver is shown in Figure 1.2. The particularity of an all-digital receiver is that sampling is performed with a free-running oscillator. The IF signal is sampled at a sampling rate of $1/T_s$ samples/second, and all processing in the receiver is done digitally by processing $r_{IF}(nT_s)$. With a free-running oscillator the sampling rate and symbol rate are incommensurate. A consequence is that sampling does not occur at the correct time (i.e., at the peak of the pulse). The difference between current and correct sampling times is referred to as the timing offset. An internal digital resampling [2] [3] is required to generate samples at the correct times.

In phase and quadrature signals $y_I[n]$ and $y_Q[n]$ are extracted by downconverting $r_{IF}(nT_s)$ to baseband using a pair of quadrature-driven mixers followed by low-pass filtering. For AWGN corrupting the signal and a flat channel, optimum filtering is obtained by using a low-pass filter matched to the filter in the transmitter [4].

Downconversion to baseband is often accompanied with cross-coupling between in

phase and quadrature signals. The problem originates from the up/down conversion between IF and RF, whereby an unknown frequency shift is introduced in the signal. Slight differences in frequency between the oscillators in the transmitter and receiver cause what is referred to as a frequency offset, df_0. This frequency offset is modeled in the receiver by denoting the frequency of the mixers by $f_0 + df_0$.

The digital signals $y_I[n]$ and $y_Q[n]$ are downsampled by M to retain only the samples at index $n = Mk$ and obtain the sequences, $y_I[k]$ and $y_Q[k]$. These sequences are the components of the complex signal, $y_I[k] + jy_Q[k]$, whose elements are referred to as the decision variables. The decision variables serve to recover the transmitted symbols. Note that in the case of perfect synchronization (i.e., no frequency, phase, or timing offsets) and a noise-free channel, the decision variables become the transmitted symbols: the real part is equal to $a[k]$ and the imaginary part to $b[k]$.

The presence of frequency and/or timing offsets make it nearly impossible to recover the transmitted symbols, unless a synchronization circuit has been incorporated into the receiver to mitigate these impediments. In digital QAM the synchronization process is usually implemented as follows [5]. Large frequency offsets are removed first since large offsets frustrate timing recovery, unless the timing recovery circuit is insensitive to a frequency offset. Synchronization to the carrier phase occurs after timing recovery. At this point the receiver is synchronized; however fine tuning of timing and carrier phase often continues during the symbol detection stage.

1.2 Motives for research

Synchronization in QAM receivers has been extensively investigated over the last thirty years and many synchronization algorithms can be found in the open literature. The approach taken in this research is to re-investigate some of the proposed algorithms. The rationale for taking that route has to do with the technology that is available today for the hardware implementation.

Most of the research took place at a time when the target technology was Appli-

cation Specific Integrated Circuit (ASIC). Today there is an alternate technology, the Field Programmable Gate Array (FPGA) [6].

There are several reasons for choosing an FPGA instead of an ASIC. FPGAs are cheaper than ASICs for low-volume productions. They are re-programmable, which is an asset in the development of products with soft specifications. The design cycles are shorter. Development times are on average 55 % less with FPGAs [7]. The availability of pre-made Hardware Descriptive Language (HDL) modules accelerates time to market. In addition FPGA vendors offer devices with embedded hard-wired blocks such as microprocessors, Digital Signal Processing (DSP) functions, and Random Access Memory (RAM).

Another factor contributing to the massive adoption of the FPGA technology by the industry is the creation of standards before products actually exist. Historically an ASIC was developed by a manufacturer. This ASIC served as a proof-of-concept and a standards organization, like the IEEE, incorporated its function into a standard. This approach created problems with patent rights, and limited the number of manufacturers. The new trend is that standards organizations create/update standards before a product exists. The establishment of standards before the technology is available is believed to open doors to small and medium-size companies, and translates into the creation of more innovative products.

One example is the cable industry. Cable TV operators felt they were held hostages by manufacturers that had proprietary technology. Cable operators joined forces by establishing a consortium to define standards for the cable TV industry [8]. This allows them to organize open competitions for the development of new equipment and then have several suppliers for that equipment. The intent was to prevent a manufacturer from developing a proprietary technology and having a monopoly on a piece of equipment. In the days when the manufacturers defined the standard, cable operators had little control over system upgrades, as they would be at the mercy of the manufacturer to improve its technology.

In the new paradigm where the cable operators define the standards, developers can take advantage of the FPGA technology but need algorithms that fit the fabric of the FPGA. One limitation factor in FPGA is the number of hard-wired multipliers. Algorithms to be implemented in an FPGA must be devised with that in mind.

Finally an FPGA may be used in established systems that must be redesigned to comply with new environmental regulations. For example, electronic equipment sold on the European market must be made to comply with the "Restriction of the use of certain Hazardous Substances in electrical and electronic equipment" (ROHS) directive. This directive came into force in July 2006. It bans the sale of electronic equipment with high-levels of lead, mercury, and other hazardous substances. If a product redesign is necessary, an FPGA rather than ASIC is more likely to be used to minimize cost and development times.

Methods and algorithms for synchronization in QAM are discussed next. This literature review provides the background to clearly state in Section 1.4 the problems that are investigated in this research. The ultimate objective is to devise synchronization algorithms that are suitable for FPGA implementation.

1.3 Background

The key component in synchronization is the estimation of the unknown parameters discussed beforehand namely frequency offset, timing offset, and phase offset. A widely applied method, which yields an asymptotically efficient estimator [9], uses the Maximum Likelihood (ML) criterion [10]. The general idea is to jointly estimate the unknown parameters (i.e., timing offset, frequency offset, ...) as well as the transmitted symbols by correlating a finite observation of the received signal with various waveforms. The waveforms, which are generated in the receiver, are attempts at reconstructing a noise-free version of the observed signal by selecting values for both the unknown parameters and the symbols. The best estimate, referred to as the Maximum Likelihood Estimate (MLE), is the one that yields maximum correlation. Mathematically the ML estimate is the one that maximizes the likelihood function of

both the parameters and symbols.

The maximum likelihood synchronizer for an analog QAM receiver was thoroughly described in [11], and was re-investigated in [12] for an all-digital receiver. This synchronizer is not practical due to the requirement of jointly estimating both the parameters and the symbols. The problem was partly solved by using decision feedback to provide knowledge of the received symbols and reduce the search to the estimation of the parameters only [11]. Decision feedback consists of feeding back the symbol decisions to the synchronizer. This technique assumes that the signal is sufficiently synchronized so the symbols can be detected with relatively little error. Decision feedback is normally used to fine tune the estimation of timing and phase offsets. An implementation of a maximum likelihood receiver using decision feedback was proposed in [13]. If decision feedback is not practical, a preamble can be transmitted. A preamble is a sequence of symbols that is known to the receiver, and is regularly transmitted to facilitate synchronization.

A preamble may not always be available and synchronization must occur with no knowledge of the transmitted symbols. This is usually the case in continuous-mode transmissions for example in the downstream links of Cable TV (CATV) networks. Several algorithms known as non-data-aided timing synchronizers, were devised to address the problem of recovering timing when the symbols or simply the data is not known [14] [15] [16] [17] [18] [19]. These algorithms, which are discussed in Section 1.3.2, do not perform as well as the maximum likelihood synchronizer but are better candidates for FPGA implementation, as they do not use an iterative search for estimating the timing offset.

For some non-data-aided timing synchronizers, frequency offsets must be removed prior to using them. This does not limit their use since frequency offset can be estimated and removed before recovering timing and with no knowledge of the symbols [20]. More is said about it in Section 1.3.4, where a block diagram depicting the overall synchronization process in a digital QAM receiver is provided.

Non-data-aided timing synchronizer exhibits a new source of noise known as self-noise. Self-noise is described in Section 1.3.3 as well as methods to mitigate it. In this research a novel technique to reduce self-noise is proposed for a non-data-aided timing synchronizer.

Synchronization in CATV upstream links networks was also investigated in this research. The application of interest was Video-On-Demand (VOD). VOD is a popular application, which allows customers to remotely select a video program from a digital library located at the Headend, and control the streaming from their set-top box located at home. The upstream channels are utilized to accommodate the player controls. A receiver is needed to demodulate the upstream channels.

VOD is a unique low-data-rate application, which uses 4-QAM for the modulation on the upstream channels. The reason for using 4-QAM also known as Quadrature Phase Shift Keying (QPSK), is that it survives the channel impairments [21] and pre-equalization is not necessary. The VOD channels, as opposed to the channels for higher-data-rate applications such as high-speed Internet, do not use ranging [8]. This makes the QPSK demodulator considerably less complicated. The transmission format is burst-mode packet, where a preamble is appended to each packet. The preamble is used for detecting the beginning of the burst (packet), acquiring timing, and performing coarse carrier frequency estimation [22]. The packets are relatively small and preambles are kept short to save bandwidth. The timing offset can be estimated with decent accuracy, but only a coarse estimation of the frequency offset is achievable. Short packets make it difficult to completely eliminate frequency offset and perform coherent detection of the symbols. Several solutions have been proposed to recover the QPSK symbols in presence of small frequency offsets [23] [24] [25] [26] [27]. These solutions are discussed in Section 1.3.5.

1.3.1 Effect of a timing offset

In high-order QAM a small timing offset can significantly degrade the performance of the system. The reason is that bandwidth efficient signaling pulses, such as the

square-root-raised cosine pulse[1] [1] with a small roll off factor, extends over several symbol intervals. No interference between symbols occurs if sampling occurs at the correct sampling time. In presence of a timing offset, the tails from previous and future symbols corrupt the current decision variable.

This phenomenon can be observed on an eye pattern [28] as shown in Figure 1.3 where the underlying continuous-time signal, $y_I(t)$, (defined in Figure 1.2 on page 3) has been plotted. To pinpoint the effect of Inter Symbol Interference (ISI), the plot was generated for 16-QAM with no frequency offset and no AWGN. There is no ISI if the decision variables are taken at the correct times, i.e., at instants of time where the eye is maximally opened, i.e., at $t/T = 0$, $t/T = 1$, ...

The presence of AWGN partly closes the eye as illustrated in Figure 1.4, where the signal to noise ratio, $\frac{E_b}{N_0}$, is 20 dB. E_b is the average energy per bit and N_0 is the one-sided power spectral density constant of the white noise.

1.3.2 Non-data-aided timing synchronizers

In the search for a low-complexity timing synchronizer, one prefers estimating the timing offset recursively rather than iteratively. In an iterative algorithm the timing offset is estimated by trying several values for the timing offset and choosing one of the values. In a recursive algorithm the timing offset is estimated by determining the quantity that must be added to the timing offset to make it zero. This quantity is obtained by changing the value of the timing offset by a small increment at each recursion. The size of the increment and direction (i.e., positive or negative increment) is adjusted at each recursion. In an iterative algorithm the same input data is processed several times with different trial values for the timing offset, whereas in a recursive algorithm new data is used at each recursion but several recursions are required for the algorithm to converge. In an iterative algorithm the input data is several symbol intervals long, whereas in a recursive algorithm the input data used

[1]The expression "square-root raised cosine" refers to the shape of the Fourier transform of the pulse.

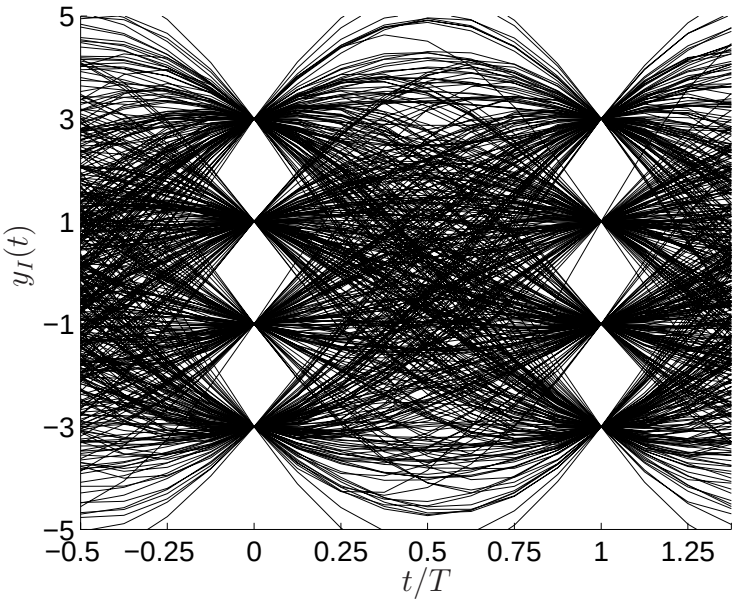

Figure 1.3 Eye pattern of the 16-QAM in phase signal in the receiver with no frequency offset and with no AWGN.

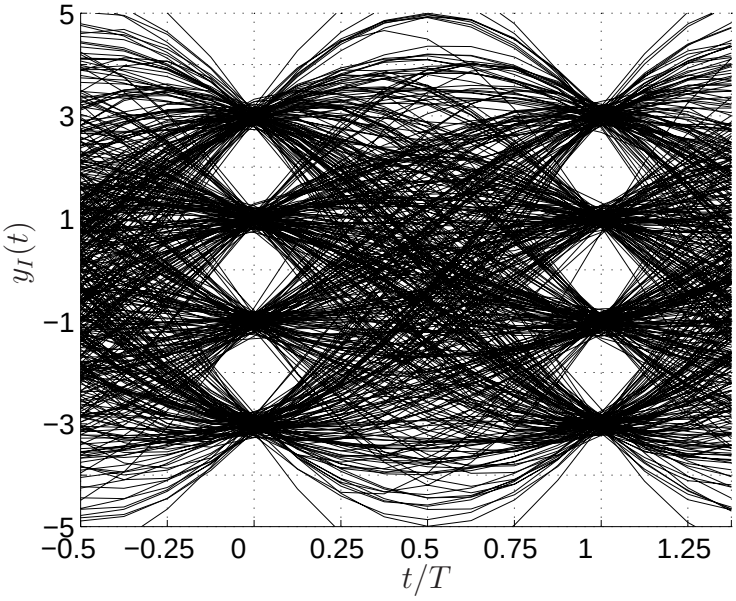

Figure 1.4 Eye pattern of the 16-QAM in phase signal in the receiver with no frequency offset and with $\frac{E_b}{N_0} = 20$ dB.

at each recursion is usually one symbol interval long only. A maximum likelihood algorithm is an iterative algorithm since it involves a search by processing the input data several times with different values for the unknown parameter to seek the value of the parameter that maximizes a likelihood function.

A suitable structure for a recursive algorithm is a feedback loop. In the case of a timing synchronizer, the feedback loop is placed after the matched filters in the receiver as shown in the block diagram of Figure 1.5. The recovery of the timing is performed as follows. A circuit known as a Timing Error Detector (TED), is inserted into the timing recovery loop to estimate the timing error between current and optimum sampling times. Two detectors are needed, one to process the upper branch referred to as the in phase branch, and one to process the lower branch referred to as the quadrature branch. The TEDs process the signals over one symbol interval to produce an estimate of the timing offset. A correction term that is proportional to this estimate is used to control the resamplers and adjust the timing. The new timing is the current timing minus the correction term. On average the adjustments are made in the direction so as to decrease the timing offset. Convergence will occur as the number of passes through the loop (i.e., number of recursions) becomes large. The rate of convergence depends on the loop gain. A small loop gain slows the convergence but reduces random fluctuations in the timing known as timing jitter. After convergence the timing offset, which is very small, continues to be estimated.

The resampler is a time-varying filter that interpolates between the receiver's samples [3]. The purpose is to produce samples at the sampling rate established in the transmitter. Depending on whether the receiver's crystal runs at a slightly higher or lower frequency than the transmitter's crystal, the resampler will produce samples at a slightly lower or higher rate than the A/D converter respectively. Most of the time the resampler produces a sample every two system's clock cycles, where the system's clock cycle runs at twice the rate of the A/D converter. However if the relative error between the transmitter's clock and receiver's clock is such that the resampling rate is higher than the sampling rate, the resampler produces on occasion

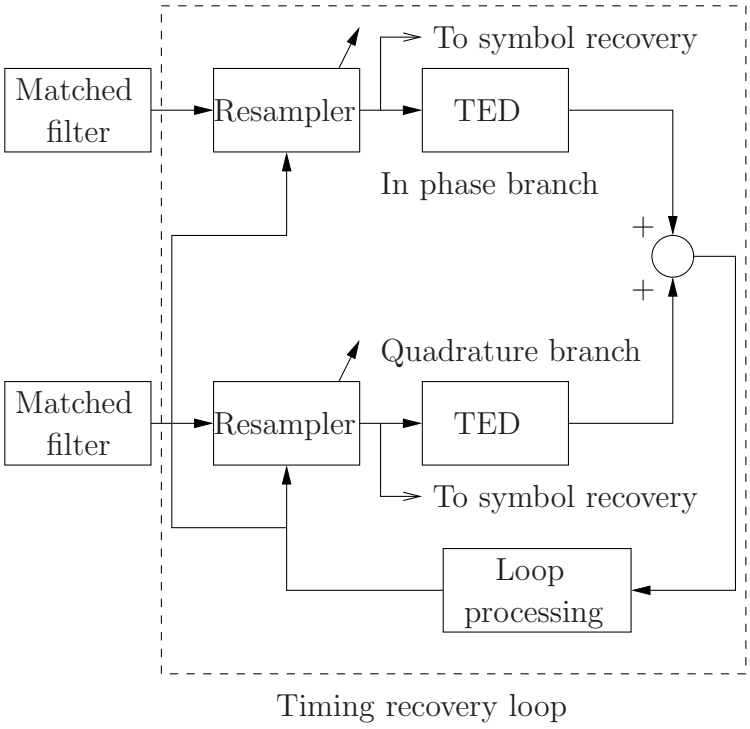

Figure 1.5 Timing recovery loop block diagram.

a sample on two consecutive system clock edges. If the resampling rate is less than the receiver's sampling rate, the resampler on occasion has samples separated by three system clock edges.

The coefficients of the resampler are a function of the required sample time with respect to the receiver's samples, and so must be adjusted prior to producing each sample. This adjustment is done to control the location of the interpolation.

A timing estimator that uses a feedback loop is called a feedback synchronizer. An alternative to the feedback structure is the feedforward structure. The main difference is that the Timing Error Detector (TED) in the feedforward synchronizer produces an estimate of the timing offset independently of the size of the offset, whereas the TED in a feedback synchronizer only produces an error signal, which can be of large variance when the offset is large. This error signal is used in a feedback loop to adjust the sampling and ultimately find the correct timing. Figure 1.6 shows

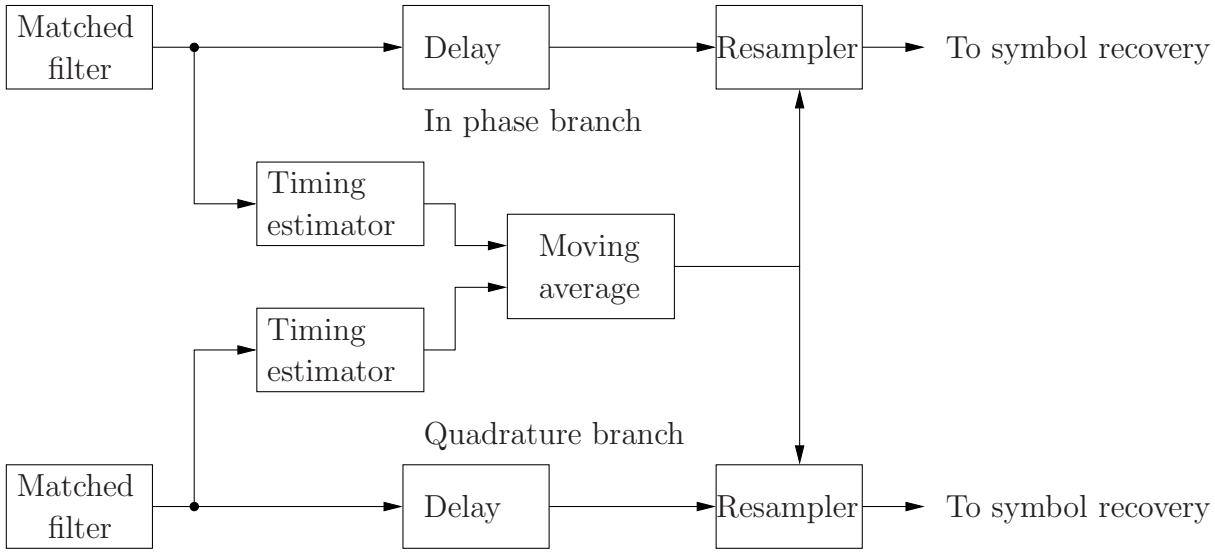

Figure 1.6 Feedforward timing synchronizer block diagram.

the general structure of a feedfoward estimator. A delay that is equal to the time (in samples) required to estimate the timing offset precedes the resampler. A more accurate timing offset estimate is obtained by averaging several estimates produced by the timing estimator. As in the case of the feedback synchronizer, both in phase and quadrature branches are processed simultaneously to estimate the timing.

Feedforward synchronizers can produce an estimate from a relatively small number of samples, which makes them well-suited for burst communication [29]. In contrast feedback loops suffer the ills of stochastic descent algorithms, one of which is hangups [30]. Hangups cause the descent to dwell on incorrect sample points for short period of times thereby lengthening acquisition times.

Feedforward synchronizers are not investigated in this research; however they received significant attention in recent years [31] [32] [33] [34]. Feedback and feedforward synchronizers are discussed below.

Feedback synchronizers

It was recognized many years ago that squaring a cyclostationary [35] signal such as a baseband Pulse Amplitude Modulation[2] signal produced a spectral line at the symbol rate [36] (PAM). The squarer is followed by a Phase-Locked Loop (PLL) to lock onto the spectral line and reject the noise. Timing is produced by detecting the zero-crossings of the regenerated clock. Such synchronizers, which are referred to as clock regenerating synchronizers, can be constructed from analog circuits.

Sampled systems have advantages and disadvantages over analog circuits. One disadvantage is that zero-crossings are not easily detected digitally, and a clock regenerating synchronizer with a zero-crossing detector can not be easily built. There are basically two digital feedback synchronizers, the early-late and Gardner synchronizers, that can be easily constructed. Both of them are briefly described below.

In [14] [37] the likelihood function of the timing offset parameter was approximated by the output of the matched filter after it had been squared. Using the squared signal, a Timing Error Detector (TED), referred to as the early-late detector [14] [15] was proposed. The main idea of the early-late detection scheme is to find where the likelihood function reaches its maximum by finding recursively where its derivative is zero using a feedback loop. At each recursion, the derivative of the likelihood function is estimated at the decision time, and this estimate is used to adjust the timing in the loop. The decision time is the instant of time when the eye diagram is believed to be maximally opened. The decision times are the times of the decision variables. An estimate of the derivative of the likelihood function is computed by using the samples at the output of the matched filter that precede (i.e., early) and follow (i.e., late) the decision variable. The difference between the early and late samples after squaring them is used as an estimate of the derivative of the likelihood function. The circuit computing this estimate is the early-late detector. This TED is used in a feedback loop to adjust the timing and force the output of the early-late detector to zero [38].

[2]In Pulse Amplitude Modulation (PAM), only one carrier is modulated in amplitude. This differs from QAM where two carriers (in quadrature) are modulated.

The synchronizer made of the feedback loop, the associated control and the TED is referred to as the early-late synchronizer.

A digital version of a zero-crossing based detector was proposed by Gardner as an improvement to the early-late detector [16]. Zero-crossings based detectors are more prone to errors when the slope of the signal at the zero-crossings is small, since Gaussian noise has more effect on small amplitude signals. In his digital detector, Gardner [16] proposed to weight the time estimates of the zero-crossings by the square of the slope at the zero-crossings. The Gardner detector operates on samples taken at twice the symbol rate[3] to produce timing offset estimates at the symbol rate. Samples half-way between decision variables are used as estimates of the timing offset multiplied by the slope. These estimates are further weighted by multiplying them with an estimate of the slope at the time of the zero-crossing. The slope is estimated by taking the difference between two decision variables: the one preceding the zero-crossing estimate and the one following it.

Feedforward synchronizers

A popular feedforward synchronizer for QAM is the digital counterpart of the analog clock regenerating synchronizer in which the PLL following the squarer is replaced by a block that computes digitally the phase of the spectral line [18]. Essentially this is the computation of a Fourier coefficient, the one that corresponds to the frequency of the symbol rate.

Modifications to Oerder's estimator [18] were proposed in [19] and [39] with the purpose of reducing the sampling rate. Lee's estimator [19] operates at twice the symbol rate (i.e., half the sampling rate of Oerder's estimator) but is biased. An unbiased version is proposed in [39].

[3]The symbol rate is the inverse of the symbol interval. In the analog domain the symbol rate is $1/T$ Hz. In the digital domain the symbol rate is T_s/T cycles / sample, so is $1/M$ cycles / sample if the sampling rate of the A/D converter is M/T samples / second.

1.3.3 Self-noise in non-data aided timing synchronizers

Non-data-aided timing synchronizers work well for certain sequences of transmitted symbols and poorly for other sequences. For example the Gardner detector produces an accurate timing estimate if the pattern is made of alternating symbols of same magnitude but opposite polarities. In that case the in phase and quadrature signals exhibit regular zero-crossings with large slopes. The repetition of the same symbol (or symbols with the same polarity) yields noisy estimates. This noise, which finds its roots in the data itself, is referred to as pattern dependent noise, self-noise [40], or systematic noise.

Self-noise was extensively studied in the case of analog spectral line regenerators [40] [41] [42], where self-noise caused fluctuations in the position of the zero-crossings, and gave rise to timing jitter. The self-noise was modeled as a cyclostationary process to analyze the jitter [41]. Power spectra expressions were derived in [42].

Self-noise reduction techniques

A natural approach to mitigate self-noise in feedback synchronizers is to operate the feedback loop with a small loop gain (narrow closed-loop bandwidth). This is equivalent to averaging a large number of detector outputs to obtain a less noisy estimate. The trade-off is longer acquisition times.

Franks [43] took a different approach by tackling the problem at its source. Franks realized that self-noise depended on the signaling pulse in addition to the data pattern. Franks discovered that certain signaling pulse shapes produced a signal that crossed zero or became zero exactly halfway between symbols, independently of the symbols that were transmitted. Franks derived a sufficient condition for non-causal signaling pulses for this to occur. A condition can be derived for causal pulses to produce similar signals. To differentiate them from Nyquist's pulses, pulses meeting Franks' condition are referred to as Franks' pulses.

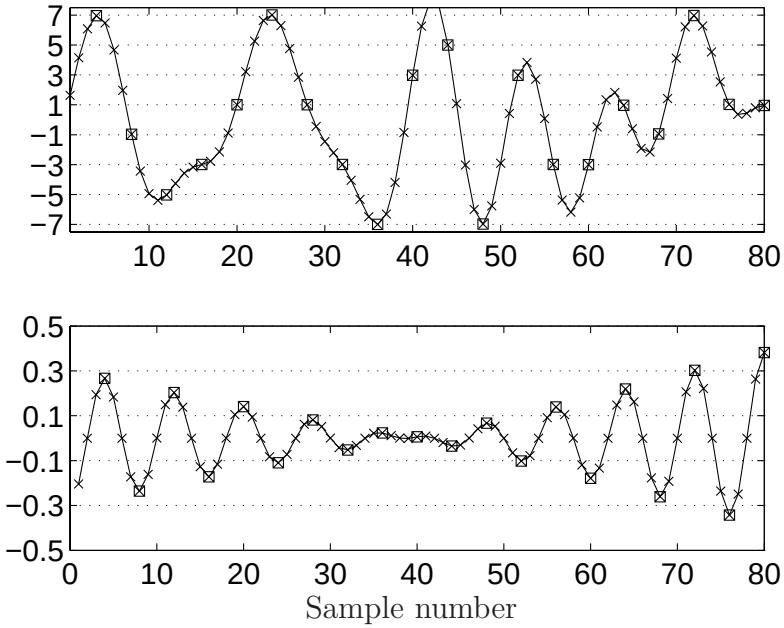

Figure 1.7 8-PAM signals generated with different signaling pulses. Top waveform: raised cosine Nyquist's pulse. Bottom waveform: Franks' pulse.

Examples of waveforms obtained with a Franks' pulse and a Nyquist's pulse are shown in Figure 1.7. The plot at the top was generated using a raised cosine signaling pulse. The plot at the bottom was produced using a Franks' pulse. The same sequence of input symbols[4], $7, -1, -5, -3, \ldots, 7, 1, 1$ was used to generate both plots. The samples, which are taken at 4 times the symbol rate, are marked with an x. There is no timing offset. The samples at the correct sampling times are surrounded by a square.

In the top plot there is no ISI at the decision times. The samples surrounded by a square hold the symbol values, $7, -1, -5, -3, \ldots, 7, 1, 1$. In the bottom plot the samples halfway between symbols are zero. The amplitude of the waveform is not constant but varies slowly with respect to the symbol rate. In contrast with the top waveform, significant ISI is present at the decision times, and the symbols can not be

[4]The symbols are real ($a[k]$ and not ($a[k]$, $b[k]$) since PAM is used instead of QAM (only one carrier is transmitted instead of two.))

recovered using that waveform.

The Gardner detector performs very well on digital signals that are produced using a Franks' pulse. This was reported in [17], where D'Andrea proposed a feedback synchronizer that uses the Gardner detector as the TED, and a prefilter that is placed in front of the feedback loop to reshape the QAM signal. The reshaping was performed by cascading the matched filters in the transmitter and receiver with the prefilter. This turned the Nyquist's pulse into a Frank's pulse. This synchronizer, referred to as the Franks/Gardner synchronizer in this thesis, does not produce self-noise after converging to the right timing. In the case of no AWGN, the middle sample half-way between symbols is zero, and the Gardner detector output remains zero. The system is nearly clock jitter free when the SNR is high. AWGN causes the middle sample to fluctuate around zero, which creates timing jitter.

Franks' pulses can also be effectively employed in feedforward synchronizers, as reported in [33].

1.3.4 Non-data-aided frequency offset estimation

Frequency offset is estimated with no knowledge of the timing and the received symbols by measuring the average power at the output of the matched filter [20]. The average power is maximum when there is no frequency offset.

There are basically two algorithms to estimate the frequency offset, an iterative algorithm and a recursive algorithm. In the iterative algorithm the frequency offset parameter is quantized and a power measurement is computed for each value of the quantized parameter. A power measurement is obtained by despinning the input signal using the trial value and feeding the resulting signal to the matched filter. The trial value that yields maximum average power at the matched filter output is the estimate.

The frequency offset estimate obtained with the iterative algorithm described previously has a special meaning since it is an estimate of the maximum likelihood

estimate of the likelihood function obtained by averaging out the data and timing offset unwanted parameters. In the recursive algorithm the frequency offset for which the derivative of the likelihood function is zero is recursively found by using a feedback loop. Such frequency offset estimator is referred to as a quadricorrelator, and has been extensively investigated [44] [45] [46] [47]. A spectral analysis of the noise can be found in [44]. A condition to avoid a Gaussian noise-induced bias is reported in [45]. Design criteria for self-noise free operation in tracking mode as well as optimum performance in presence of Gaussian noise are derived in [46] [47].

A block diagram depicting the synchronization process in an all-digital QAM receiver is given in Figure 1.8. The frequency offset, df_0, can be estimated using a quadricorrelator. The quadricorrelator produces an estimate, $\hat{df}_0$, of the frequency offset by processing the matched filters' and Frequency Matched Filters' (FMF) outputs. A small residual frequency offset, $df_0 - \hat{df}_0$, remains after downconversion to baseband. Timing can be recovered in the presence of this small frequency offset. The downsamplers isolate the decision variables after timing has been recovered. The decision variables, shown in Figure 1.8 as $x_I[k]$ and $x_Q[k]$, are estimates of $a[k]$ and $b[k]$. Coherent detection of the transmitted symbols requires removing the residual frequency offset $df_0 - \hat{df}_0$. This offset is removed by applying phase corrections to the NCO. The phase corrections are provided by a decision directed loop that estimates the angle between the vectors $x_I[k] + jx_Q[k]$ and $\hat{a}[k] + j\hat{b}[k]$, where $(\hat{a}[k], \hat{b}[k])$ is the symbol decision at the output of the slicers.

1.3.5 QPSK symbol recovery in presence of a frequency offset

Quadrature Phase Shift Keying (QPSK) is a special case of QAM, where the symbols have the same magnitude. By magnitude it is meant that the magnitude of the complex number, $a[k] + jb[k]$, where $(a[k], b[k])$ is the symbol. In the sequel symbols are written as complex numbers (i.e., $a[k] + jb[k]$) instead of as a 2-tuples (i.e., $(a[k], b[k])$). QPSK has 4 symbols. It is customary to set the magnitude of the

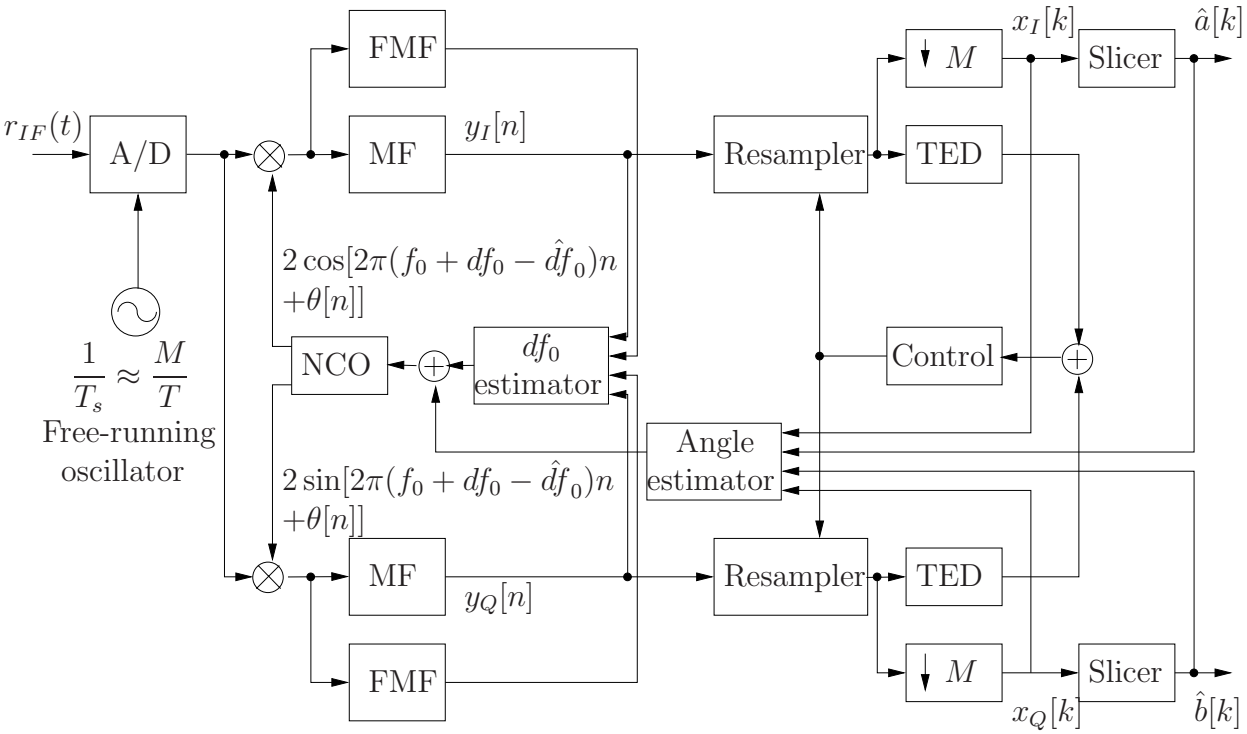

Figure 1.8 Synchronization in an all-digital QAM receiver.

transmitted symbols to 1, which makes the values of the symbols for QPSK equal to $\frac{\sqrt{2}}{2}(1+j)$, $\frac{\sqrt{2}}{2}(1-j)$, $\frac{\sqrt{2}}{2}(-1+j)$, and $\frac{\sqrt{2}}{2}(-1-j)$. A plot in the complex plane of the vectors corresponding to the transmitted symbols is shown in Figure 1.9. Clearly all four vectors have a magnitude of 1. The vector angle is either 45^o, -45^o, 135^o or -135^o. The angle between two symbols is either $\pm 90^o$ or 180^o.

The effect of a phase or a frequency offset on the detection of the transmitted symbols can be visualized by plotting the decision variables in the complex plane. Such a plot, often referred to as a constellation plot, is shown in Figure 1.10 for three cases. Figure 1.10(a) is the case of perfect synchronization, Figure 1.10(b) is the case of a phase offset of 20 degrees, and Figure 1.10(c) is the case of a frequency offset of 1 % of the symbol rate. The SNR, E_b/N_0, was equal to 20 dB for all three constellation plots and each plot was drawn using 2000 decision variables.

In Figure 1.10(a) the constellation consists of 4 clouds of points, each of them being

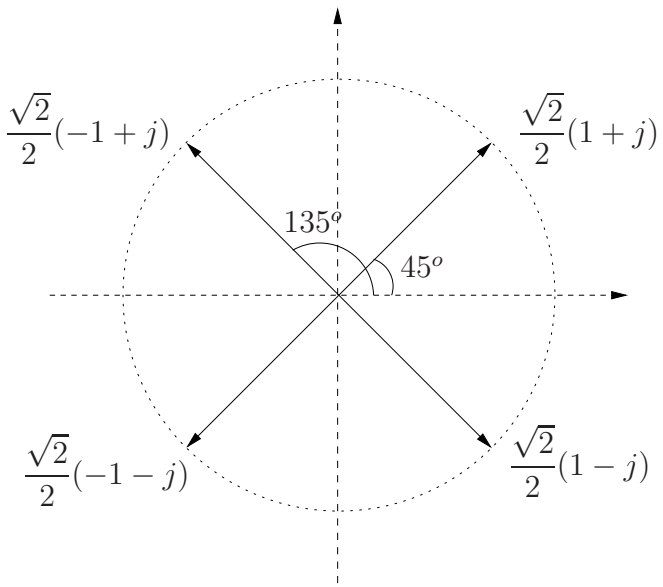

Figure 1.9 QPSK symbols plotted as vectors in the complex plane.

centered at one of the 4 symbol locations. The deviations of the decision variables from the symbol locations are due to the Gaussian noise corrupting the signal. Clearly from Figure 1.10(b), a phase offset of 20 degrees causes a rotation of the constellation by 20 degrees. It can be seen from Figure 1.10(c) that a frequency offset causes the constellation to spin. For a frequency offset of 1 % of the symbol rate, the spinning rate is equal to $0.01 * 360^o = 3.6^o$ per symbol interval.

In the QPSK system of interest in this research, the preamble in the packet is used to find timing [22]. Residual timing offsets may be present after the preamble has been processed, but they will be small and can be neglected. The problem is the residual frequency offset that remains after processing the preamble. This will cause the constellation to spin during the processing of the payload.

A widely-used method to recover the data in presence of a phase offset or even a small frequency offsets is differential detection. This method requires differential encoding in the transmitter. Differential encoding consists of mapping the data bits over two transmitted symbols instead of one. The angle between the two transmitted symbols is used as a means to convey the information. The angle between symbols is

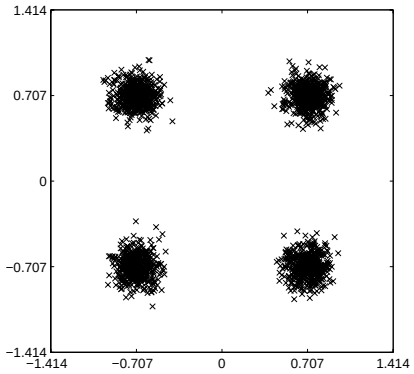

(a) Perfect synchronization

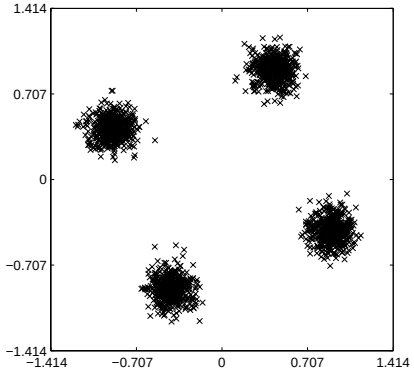

(b) 20 degrees phase offset

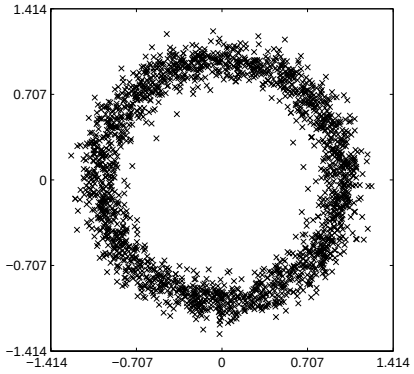

(c) 1 % of the symbol rate frequency offset

Figure 1.10 QPSK constellations with (a) perfect synchronization, (b) presence of a phase offset equal to 20^o , (c) presence of a frequency offset equal to 1 % of the symbol rate, $E_b/N_0 = 20$ dB.

referred to as the modulating phase. From Figure 1.9 this angle can take on values 0^o, $+90^o$, -90^o, and 180^o.

Systems that use differential encoding have a transient at start-up. The system is initialized by first transmitting one of the four symbols. This first symbol will serve as the reference for the transmission of the second symbol, which then will act as the reference for the transmission of the third symbol, and so on. If the modulating phase is equal to 0^o, the reference symbol is sent a second time. If the modulating phase is equal to $+90^o$ (respectively -90^o, 180^o), the symbol that is $+90^o$ (respectively -90^o, 180^o) away from the reference symbol is transmitted. In the receiver, the modulating phase is recovered by simultaneously processing the current and previous decision variables. The processing consists of generating a new decision variable, referred to as the differential decision variable, whose angle is the angle between the two successive decision variables. It is obtained with a complex multiplication of the current decision variable and the complex conjugate of the previous decision variable. The differential decision variable is rounded to the closest of 0^o, $+90^o$, -90^o, or 180^o, and that rounded phase is taken to be the transmitted modulating phase.

Differential detection is insensitive to a phase offset, but is sensitive to a frequency offset. A frequency offset in differential detection translates into a rotation of the differential decision variables. This rotation places the differential decision variables closer to the decision boundaries, which increases the likelihood of making an error when detecting the modulating phases. This point reinforces the importance of estimating the frequency offset as accurately as possible, with the information in the preamble. Several nearly efficient algorithms were proposed in that regard [25] [24] [23] [48] [49]. These algorithms were devised under the assumption that timing had been perfectly recovered. This does not restrict the use of these algorithms. From an implementation point of view timing is usually found before complete reception of the preamble. All samples that have been received to that point are stored in memory. Timing information is then used to resample the stored signal before it is passed to the frequency offset estimator.

Under the conditions of perfect timing and knowledge of the symbols, the problem of estimating the frequency offset reduces to the estimation of the frequency of a complex sinusoid. Tretter derived an estimator that approaches the Cramer-Rao Bound (CRB) for reasonably large SNRs [25].

Tretter's estimator requires phase unwrapping. Kay [24] derives an estimator, which also approaches the CRB for reasonably large SNRs, but does not need phase unwrapping. The angle between two consecutive samples is used instead of the angles of the samples. Taking the difference colors the noise. However the noise is whitened by using a window, which makes Kay's algorithm mathematically equivalent to Tretter's algorithm.

Tretter's and Kay's estimators attain the CRB for high SNRs. Improvements to these estimator were proposed in [23] [48] [49]. The proposed estimators approach the CRB at lower SNRs. Improvements come from extending the computation of phase differences to samples that are 2 symbol intervals apart, 3 symbol intervals apart and so on.

A different strategy to reduce the probability of making an error is to improve the differential detection scheme. In differential detection, which is referred to in the sequel as the conventional differential detection, the previous decision variable, which is corrupted by noise, serves as the reference to detect the current modulating phase. In coherent detection the reference is noise-free so for moderate to high SNRs the noisy reference in conventional differential detection results in a 3 dB performance loss over coherent detection.

In [27] a technique referred to as multiple-symbol differential detection, is proposed to recover some of the loss associated with the conventional differential detection. The algorithm consists of jointly processing M decision variables to find using an iterative search the most likely $M-1$ modulating phases that were transmitted.

Timing/frequency estimators for QPSK have also been proposed for a preambleless coherent demodulator [50] [51]. The received burst is stored in memory for a

two-pass scheme. Timing recovery and frequency offset estimation occur in the first pass. Following resampling and despinning, phase acquisition occurs in the second pass by using only the first half of the burst. Demodulation starts in the middle of the burst with two feedback loops. One loop processes the second-half of the burst by moving forward through the RAM. The other loop processes the first half of the burst by moving backward through the RAM.

1.4 Research problems and thesis outline

Three synchronization-related problems are investigated in this research:

- Self-noise reduction in non-data-aided feedback synchronizers.
- Timing jitter analysis of the Franks/Gardner synchronizer.
- Detection of QPSK symbols in presence of a frequency offset.

1.4.1 Self-noise reduction in non-data-aided feedback synchronizers

A block diagram of the Franks/Gardner synchronizer is shown in Figure 1.11. Notice that the resampler of the timing recovery loop follows the prefilter. The reshaping of the signal by the prefilter causes distortions in the form of ISI, so the output of the resampler in the timing recovery loop does not recover the symbols even if the sampling occurs at the correct times. In the Franks/Gardner synchronizer a second resampler is placed after the matched filter. The delay block mirrors the delay of the prefilter.

More is said at this point about the prefiltering performed in the Franks/Gardner synchronizer. The reason is that an alternative method to Franks' that also mitigates self-noise is proposed in Chapter 2.

The nice feature of waveforms produced with a Franks' pulse is the presence of zeros half-way between symbols (see Figure 1.7 on page 17). A condition for this to

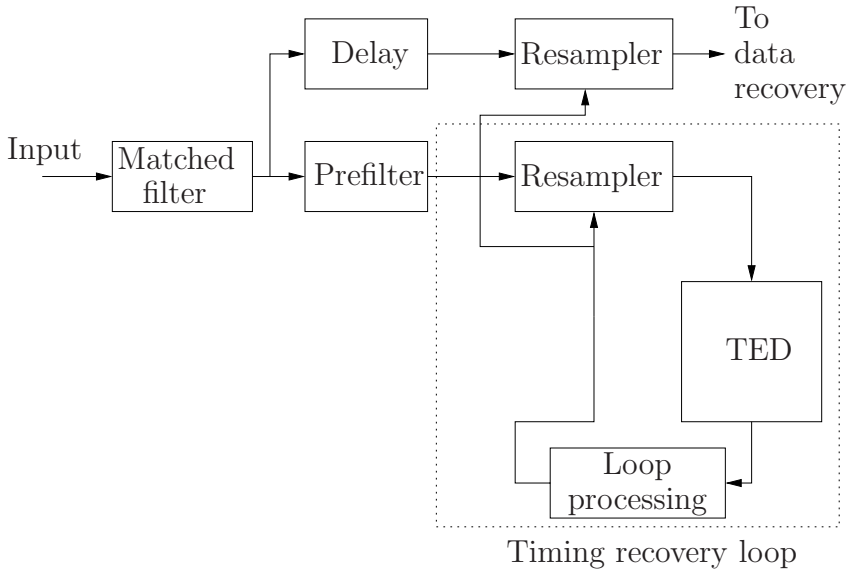

Figure 1.11 Gardner / Franks' synchronizer block diagram.

occur at the output of the prefilter is that the overall pulse, $p(t)$, of the cascaded matched filters and prefilter verifies $p(kT + \frac{T}{2}) = 0$ for all k. Applying the inverse Fourier transform relation yields

$$\begin{aligned} p(kT + \frac{T}{2}) &= \frac{1}{2\pi} \int_{-\infty}^{+\infty} P(j\Omega) e^{j\Omega(kT+\frac{T}{2})} d\Omega \\ &= \frac{1}{2\pi} \sum_{l=-\infty}^{+\infty} \int_{\frac{-2\pi l}{T}-\frac{\pi}{T}}^{\frac{-2\pi l}{T}+\frac{\pi}{T}} P(j\Omega) e^{j\Omega(kT+\frac{T}{2})} d\Omega, \end{aligned}$$

where $P(j\Omega)$ is the Fourier transform of $p(t)$.

Applying the change of variable $\Omega = \Omega + \frac{2\pi l}{T}$ results in

$$\begin{aligned} p(kT + \frac{T}{2}) &= \frac{1}{2\pi} \int_{-\frac{\pi}{T}}^{+\frac{\pi}{T}} \sum_{l=-\infty}^{+\infty} P(j(\Omega - \frac{2\pi l}{T})) e^{j(\Omega - \frac{2\pi l}{T}))(kT+\frac{T}{2})} d\Omega \\ &= \frac{1}{2\pi} \int_{-\frac{\pi}{T}}^{+\frac{\pi}{T}} \sum_{l=-\infty}^{+\infty} (-1)^l P(j(\Omega - \frac{2\pi l}{T})) e^{j\Omega(kT+\frac{T}{2})} d\Omega. \end{aligned} \tag{1.1}$$

A sufficient condition for (1.1) to be zero for all k is that $\sum_{l=-\infty}^{+\infty} (-1)^l P(j(\Omega - \frac{2\pi l}{T})) = 0$.

For $P(j\Omega)$ limited to a bandwidth that is less than $2\pi/T$, the condition reduces to

$$P(j\Omega) = P(j(\Omega - \frac{2\pi}{T})),\ 0 \leq \Omega < \frac{2\pi}{T}. \tag{1.2}$$

This condition, which was initially derived by Franks [43], applies to a non-causal pulse, and states that the Fourier transform of the pulse must be even around $\frac{\pi}{T}$.

For matched filters with a square-root raised cosine frequency response with roll off factor r, D'Andrea proposed in [17] the following frequency response

$$H_P(j\Omega) = \begin{cases} \frac{1}{T}G_N(j(\Omega - \frac{2\pi}{T})) & 0 \leq \Omega < \frac{2\pi}{T} \\ \frac{1}{T}G_N(j(\Omega + \frac{2\pi}{T})) & -\frac{2\pi}{T} < \Omega < 0, \end{cases} \tag{1.3}$$

for the prefilter, where $G_N(j\Omega)$ is the raised cosine function.

With a prefilter defined as in (1.3), the Fourier transform of the overall shaping pulse $p(t)$ is

$$P(j\Omega) = \begin{cases} \frac{T}{4}\cos^2\left[\frac{\pi}{2r}\left(\frac{|\Omega|T}{\pi} - 1\right)\right], & \frac{\pi}{T}(1-r) \leq |\Omega| \leq \frac{\pi}{T}(1+r) \\ 0, & \text{elsewhere} \end{cases} \tag{1.4}$$

and in the time-domain the shaping pulse is given by [17]

$$p(t) = \frac{\sin r\pi t/T}{4\pi t/T(1-(rt/T)^2)}\cos\frac{\pi t}{T}. \tag{1.5}$$

The pulse $p(t)$ was used to generate the bottom waveform shown in Figure 1.7.

Plots of $G_N(j\Omega)$, $H_P(j\Omega)$, and $P(j\Omega)$ are shown in Figure 1.12 for $r = 0.5$ and $T = 1$. Only the positive frequencies are shown. Clearly $P(j\Omega)$ verifies (1.2) since it is even about $\Omega = \pi$.

Practical systems require $p(t)$ to be causal. $p(t)$ can be made causal by delaying and truncating it. Delaying $p(t)$ by t_0 yields $p_{t_0}(t) = h(t-t_0)\cos(\frac{\pi t}{T} - \frac{\pi t_0}{T})$, whose Fourier transform is $P_{t_0}(j\Omega) = P(j\Omega)e^{-j\Omega t_0}$. $P_{t_0}(j\Omega)$ does not verify (1.2), but a

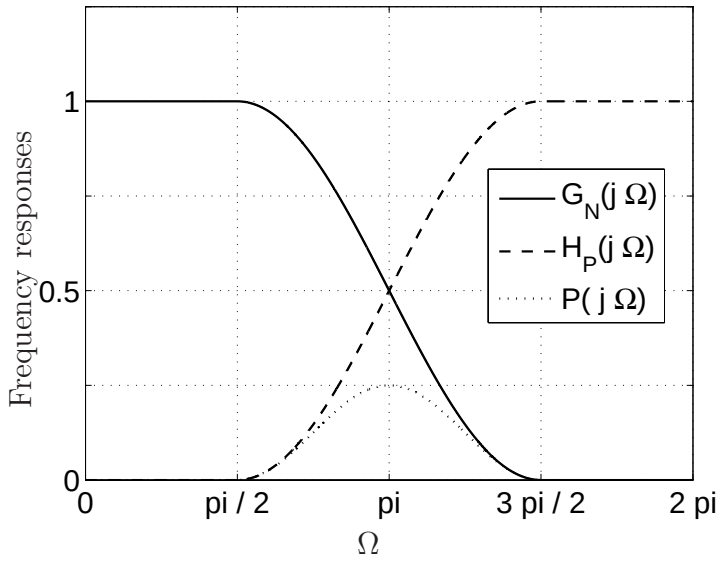

Figure 1.12 Frequency responses of D'Andrea's prefilter ($H_P(j\Omega)$) along with raised cosine function ($G_N(j\Omega)$), and frequency response of shaping pulse ($P(j\Omega)$) with $r = 0.5$ and $T = 1$.

condition (for causal pulse) is derived by observing that waveforms produced with $p_{t_0}(t)$ are zero at times $t_0 + T/2 + kT$. From (1.1) with $kT + \frac{T}{2}$ replaced by $kT + \frac{T}{2} + t_0$ produces

$$p(kT + \frac{T}{2} + t_0) = \int_{-\frac{\pi}{T}}^{+\frac{\pi}{T}} \sum_{l=-\infty}^{+\infty} (-1)^l P(j(\Omega - \frac{2\pi l}{T})) e^{j(\Omega - \frac{2\pi l}{T}))(kT + \frac{T}{2} + t_0)} d\Omega. \qquad (1.6)$$

and the condition becomes

$$P_{t_0}(j\Omega) = e^{-j\frac{2\pi}{T}t_0} P_{t_0}(j(\Omega - \frac{2\pi}{T})),\ 0 \leq \Omega < \frac{2\pi}{T}. \qquad (1.7)$$

Therefore by delaying and truncating a non-causal impulse, a practical FIR prefilter can be built such that the frequency response of the overall pulse verifies (1.7).

The problem with reshaping the signal to force zero-crossings is that a relatively long Finite Impulse Response (FIR) filter is required to implement the prefilter. From (1.3) a digital implementation of the prefilter requires its length to be equal

to the length of the filter resulting from cascading matched filters in transmitter and receiver. It is common to use a matched filter in the transmitter that is 20 symbols long to limit leakage to the adjacent frequency bands.

In addition to the long FIR filter, the symbols are lost in this reshaping and an additional resampler is required for recovering the data. In this research a different approach than D'Andrea's is taken to reveal an economical way to reduce the self-noise.

In Chapter 2 a novel filtering technique to mitigate self-noise in the early-late and Gardner detectors is proposed. This technique consists of incorporating a few single-pole filters inside the detector instead of using a prefilter, as in the Franks/Gardner synchronizer. The modified detectors are referred to as enhanced detectors. An analysis of the steady state self-noise of the enhanced early-late detector is also carried out. In Chapter 3 the increase in performance obtained with the enhanced early-late detector is assessed in closed-loop operation. Performance comparisons with other detectors is also the object of Chapter 3.

1.4.2 Timing jitter analysis of the Franks/Gardner synchronizer

The impact of applying Franks' prefilter to feedforward synchronizers has been recently analyzed in [33] [31], where it is shown that the modified Lee's feedforward synchronizer [39] is nearly self-noise free when the prefilter is used. In [31] it is found that the square detector proposed by Oerder and Meyr [18] performs the best in the class of non-data aided feedforward synchronizer. These papers also provide thorough analyses of the timing jitter by deriving closed-form expressions for the jitter variance.

No thorough analysis of the timing jitter could be found in the literature for the class of non-data-aided feedback synchronizers that are equipped with Franks' prefilter. In this class the Franks/Gardner synchronizer exhibits the best performance [52]. In Chapter 4 the timing jitter of the Franks/Gardner synchronizer is analyzed to yield a closed-form expression for the detector's noise power spectrum. From

this expression the power spectrum of the timing jitter can be determined from knowledge of the frequency response of the timing recovery loop. A simple equation to estimate the timing jitter variance in closed-loop systems with small bandwidths is also derived. Performance comparisons between the Franks/Gardner feedback synchronizer and the Oerder/Meyr feedforward synchronizer show that the Franks/Gardner synchronizer outperforms the Oerder/Meyr feedforward synchronizer.

The increase in performance of the Franks/Gardner synchronizer over the Oerder/Meyr synchronizer was established by plotting the timing jitter variances of both synchronizers as well as the Modified Cramer-Rao Bound (MCRB). The MCRB is a looser bound than the Cramer-Rao Bound (CRB). However it is often used as it is simpler to evaluate than the CRB. The MCRB was derived by D'Andrea [53]. The derivation was done in the case of a continuous-time signal. This thesis deals with digital signals, so the MCRB for timing offset is rederived in Appendix A in the case of a discrete-time signal that is sampled at a rate greater than or equal to the Nyquist rate.

1.4.3 Detection of QPSK symbols in presence of a frequency offset

An improvement to the conventional differential detection scheme was proposed by Divsalar in [27]. In conventional differential detection the k^{th} transmitted modulating phase, denoted by φ_k, is detected in the receiver by essentially selecting for φ_k the value, $\hat{\varphi}_k$, that maximizes the metric, $\mathcal{R}e\left\{r_k r_{k-1}^* e^{-j\hat{\varphi}_k}\right\}$, where $\hat{\varphi}_k$ can be either 0^o, 90^o, -90^o or 180^o, r_k and r_{k-1} are the current and previous decision variables, and $\mathcal{R}e\{\cdot\}$ returns the real part. Divsalar expands this metric to allow for the detection of multiple modulating phases simultaneously.

Divsalar proposed a decision rule to jointly detect $M-1$ modulating phases in presence of a phase offset. This rule, which for $M=2$ is the same as the decision rule previously given for conventional differential detection, was obtained by using the maximum likelihood criterion. The probability of making an error is minimized

if Divsalar's rule is applied to jointly detect $M-1$ modulating phases in presence of an unknown phase offset. For $M=5$ and a SNR of $E_b/N_0 = 13$ dB, an improvement in performance of 1.5 dB over conventional differential detection was reported in [27].

Essentially the improvement in performance comes from observing more than two decision variables before making a decision on the modulating phases. This is illustrated with an example where numerical values were chosen for decision variables, r_k, r_{k-1}, and r_{k-2}, and Divsalar's decision rule [27] with $M=3$ was applied to detect φ_k and φ_{k-1}. For $M=3$ the decision rule is: select the values $\hat{\varphi}_k$ and $\hat{\varphi}_{k-1}$ from the possible values for φ_k and φ_{k-1} that maximizes $\mathcal{R}e\left\{d_{\hat{\varphi}_k,\hat{\varphi}_{k-1}}\right\}$, where

$$d_{\hat{\varphi}_k,\hat{\varphi}_{k-1}} = r_k r_{k-1}^* e^{-j\hat{\varphi}_k} + r_{k-1} r_{k-2}^* e^{-j\hat{\varphi}_{k-1}} + r_k r_{k-2}^* e^{-j(\hat{\varphi}_k+\hat{\varphi}_{k-1})}.$$

Figure 1.13 is a plot that shows three values for the decision variables, r_k, r_{k-1}, and r_{k-2}, and three vectors. The three $d_{\hat{\varphi}_k,\hat{\varphi}_{k-1}}$ vectors shown are $d_{0^o,90^o}$, $d_{90^o,90^o}$, and $d_{0^o,180^o}$.

If conventional differential detection is used to decide φ_k and φ_{k-1} then from Figure 1.13, the values obtained would be $\hat{\varphi}_k = 90^o$ and $\hat{\varphi}_{k-1} = 0^o$ since $r_k r_{k-1}^*$ has an angle of 110^o and $r_{k-1} r_{k-2}^*$ has an angle of 40^o. Divsalar's rule with $M=3$ yields $\hat{\varphi}_k = 90^o$ and $\hat{\varphi}_{k-1} = 90^o$, which differ from the values obtained with conventional differential detection. The reason $d_{90^o,90^o}$ is chosen over both $d_{0^o,90^o}$ and $d_{0^o,180^o}$ is that it has the largest real part. In this case Divsalar's rule yields different values for φ_k and φ_{k-1} than the conventional detection.

An intuitive explanation for the difference is that the angle of $r_k r_{k-2}^*$ should be close to 90^o if $\varphi_k = 90^o$ and $\varphi_{k-1} = 0^o$. However the angle is equal to 150^o, which is closer to 180^0 than 90^o, and $\hat{\varphi}_k = 90^o$ and $\hat{\varphi}_{k-1} = 90^o$ seems to be a better choice as confirmed by the decision rule.

Despite the iterative search, which can be easily implemented in QPSK as 90^o rotations do not require multiplications, a significant number of multiplications is

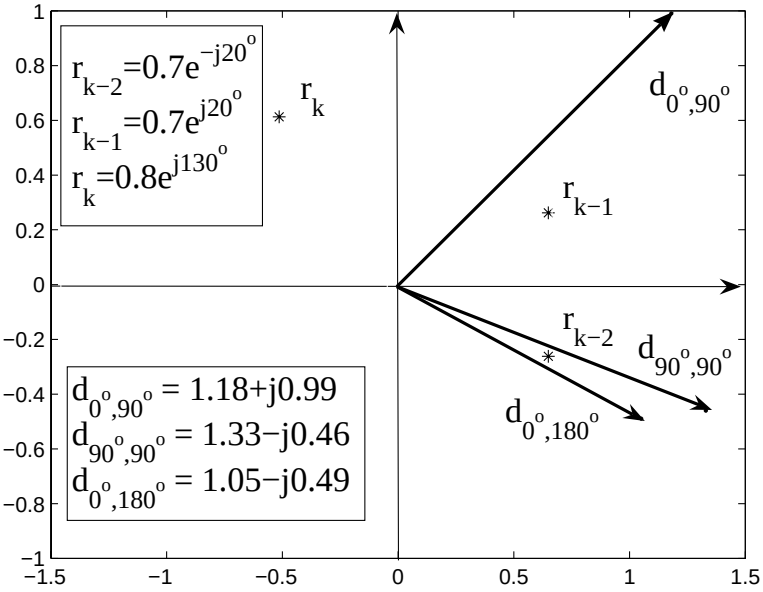

Figure 1.13 Example using Divsalar's rule with $M = 3$ to detect modulating phases, φ_k and φ_{k-1}, using decision variables, r_k, r_{k-1}, and r_{k-2}.

required to implement Divsalar's decision rule especially if M is large. For $M = 5$ 10 complex multiplications are needed to detect 4 modulating phases, which gives a ratio of 2.5 complex multiplications per modulating phase.

In this research a different approach than Divsalar is taken. The proposed detector offers fast carrier synchronization and 2 dB improvement over differential detection [54], while it still remains a low-complexity detector that is suitable for FPGA implementation. The proposed detector is described in Chapter 5.

2. Enhanced Feedback Synchronizers

2.1 Introduction

The problem with non-data-aided feedback synchronizers is that they produce self-noise. An efficient solution to mitigate self-noise is Franks' prefiltering technique. However the prefilter takes the form of a long FIR filter, which consumes significant hardware resources.

In this research an approach different from Franks' is taken to reduce self-noise in feedback synchronizers. Franks' technique consists of reshaping the signaling pulse to force mid-symbol zero-crossings into the signal. In his approach Franks does not consider whether or not the reshaping removes timing information. Should the reshaping remove timing information, then the channel noise would have a greater effect on the timing jitter.

The approach taken here is to derive an equation for the input-output characteristic of the detector. The detector is isolated from the timing recovery loop. The input signal has a fixed timing offset. The early-late detector was chosen for the derivation as the mathematic was believed to be more manageable than with the Gardner detector. The derivation of an equation for the input-output characteristic reveals the spectral location of the timing information and an inexpensive way to reduce the self-noise while preserving most of the timing information [52].

Chapter 2 is organized as follows. A description of the early-late detector operation is given in Section 2.2. This description is followed by an analysis of the early-late detector in Section 2.3. The closed-form expression for the input-output characteristic

or S-curve is also given in that section. From this analysis a novel filtering technique to mitigate self-noise is proposed in Section 2.4 to enhance the early-late detector. The performance of the enhanced detector is measured with a computer simulation. A closed-form expression for the steady state self-noise power spectrum of the enhanced detector is derived in Section 2.5. In Section 2.6 it is shown how to incorporate the proposed self-noise reduction technique into the Gardner detector.

2.2 Principle of operation of the early-late detector

The early-late detector estimates the timing offset using two samples per symbol. One sample is taken before the decision variable. One sample is taken after the decision variable. The timing offset, εT, is estimated with $[x_I^2(kT+D+\varepsilon T) - x_I^2(kT-D+\varepsilon T)] + [x_Q^2(kT+D+\varepsilon T) - x_Q^2(kT-D+\varepsilon T)]$, where $x_I(kT+\varepsilon T)$ and $x_Q(kT+\varepsilon T)$ are the in phase and quadrature decision variables, kT are the instants of time when the eye is maximally opened, and D specifies the difference in time between the decision variables and the early/late samples. Usually $D = 0.25T$. This choice makes the detector the most sensitive to a timing offset.

The amount of self-noise produced by the early-late detector depends on the transmitted symbol sequence. The early-late detector works very well if the symbol sequence is such that the signal is a sinusoid. This is illustrated in Figure 2.1, where a noise-free BPSK signal with alternating $+1, -1$ symbols[1] is shown. The samples are marked with either a circle or a star. The sampling rate is exactly four times the symbol rate. In Figure 2.1(a) timing is perfect (i.e., $\varepsilon T = 0$). The decision variables are marked with a star. The sampling times are correct so the decision variables hold the symbols. The early sample and late sample that form a pair are on either side of the decision variables. The difference between late and early samples after squaring is $x^2(kT + 0.25T) \; - \; x^2(kT - 0.25T)] \; = \; 0$ for all k.

In Figure 2.1(b) the sampling rate is still four times the symbol rate, but the timing offset is $\varepsilon T = -0.125T$. The difference between the squares of the late and early

[1] In BPSK, one carrier is transmitted and the symbols reduce to $a[k]$, where $a[k] = \pm 1$.

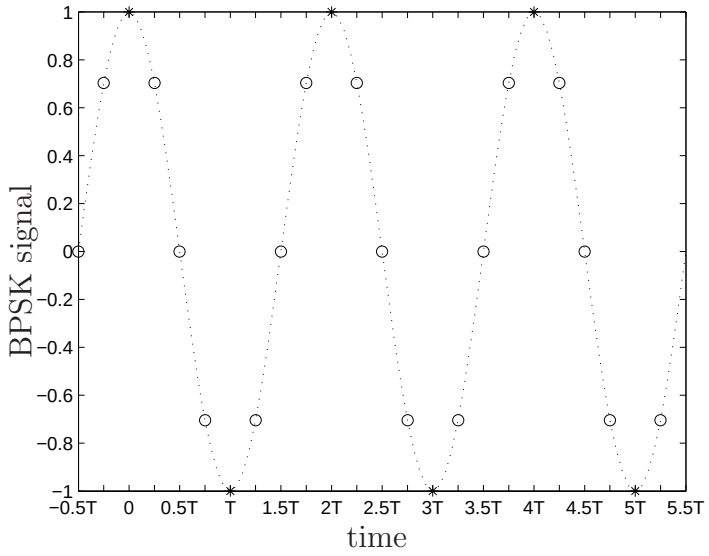

(a) $\varepsilon T = 0$

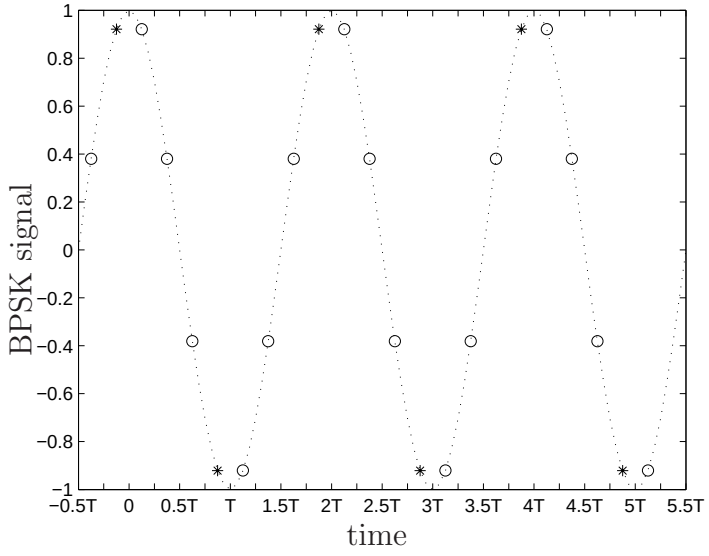

(b) $\varepsilon T = -0.125T$

Figure 2.1 Examples of waveforms producing no self-noise.

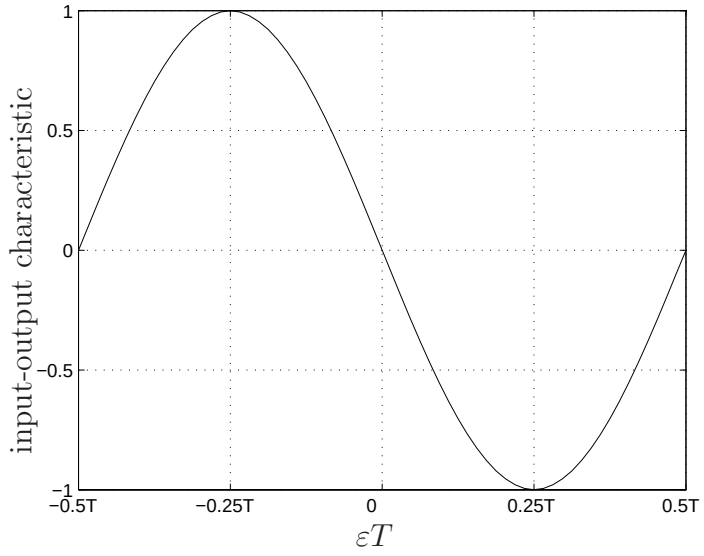

Figure 2.2 Input-output characteristic of early-late detector in the case of an alternating $+1, -1$ symbol pattern.

samples on either side of the decision variable is $x^2(kT + 0.25T - 0.125T) - x^2(kT - 0.25T - 0.125T)] = 1/\sqrt{2}$ for all k.

Note that in the case of an alternating symbol pattern, the sampled waveform can be mathematically expressed as $\cos(\frac{\pi}{T}(\frac{T}{4}n + \varepsilon T))$. For that particular symbol pattern the early-late detector output remains constant, free of self-noise. The input-output characteristic of the detector is simply obtained by evaluating $x^2(kT+0.25T-\varepsilon T) - x^2(kT - 0.25T - \varepsilon T)]$ for different timing offsets, εT. This curve is shown in Figure 2.2. The curve is zero at $\varepsilon T = 0$ and odd about zero. Note that the point, $\varepsilon T = 0$, serves as the equilibrium point of the feedback loop. Timing is adjusted inside the loop to force the timing offset toward zero. The sensitivity of the detector to the timing offset depends on the slope of the input-output characteristic at $\varepsilon T = 0$. This curve, which was obtained for an input signal with alternating symbols, characterizes the amount of timing information contained in this particular signal.

In the case of interest in this thesis, which is the transmission of random data (i.e., non-data-aided timing recovery), the input-output characteristic curve, which

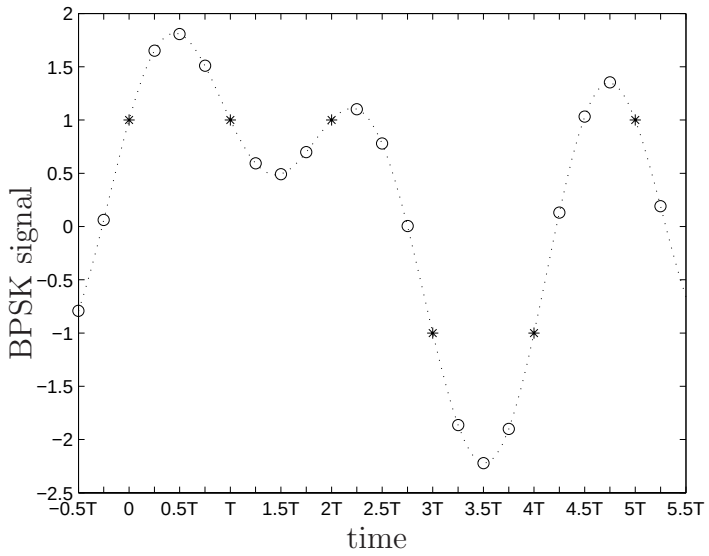

Figure 2.3 Example of a waveform producing self-noise ($\varepsilon T = 0$).

in this case is commonly referred to as the S-curve [55], is not derived as easily as in the case of an alternating symbol pattern. The reason is that the output of the detector is noisy. Several outputs of the detector are needed to estimate the S-curve at one point. The detector outputs are averaged as a means to reduce the noise and estimate the S-curve at that timing offset. Theoretically if the average is long enough, this is equivalent to taking the expectation of the detector output.

The necessity of averaging several detector outputs to find the S-curve becomes obvious when looking at a signal generated with random symbols. In Figure 2.3 a noise-free BPSK signal is shown, where the displayed symbols are $1, 1, 1, -1, -1, 1$. It can be seen from Figure 2.3 that even though the timing is correct, the detector output varies widely. The large variations at the output depend on the data sequence that generated the received signal. For this reason the detector noise is referred to as data-dependent or pattern-dependent noise or self-noise. The origin of the self-noise is the lack of correlation between the early and late samples in the case of random symbols. An analysis of the detector output in the case of the transmission of random symbols is the object of Section 2.3. This analysis leads to of a closed-form expression

for the S-curve equation.

2.3 Analysis of the early-late detector

An early-late detector circuit is shown in Figure 2.4. Two early-late detectors are shown. The detector at the top of the figure processes the in phase branch signal and is referred to as the in phase detector. The detector at the bottom of the figure processes the quadrature branch signal and is referred to as the quadrature detector. Both detectors are identical.

There are two system parameters, M and m, both of which are positive integers. The early and late signals are obtained by downsampling the input signal by M. The system parameter, m, which is less than M, sets the time between the early and late samples to $2m$ samples. Therefore the early signal is produced by delaying the input signal by $2m$ samples before downsampling by M. Typically M is 4 and m is 1. After being delayed by m samples the decision variable is also downsampled by M. The decision variable is not used by the early-late detector, but the purpose of the detector is to control the sample time of the decision variable.

The in phase branch input signal is $x_I((n+m)T/M + \varepsilon T)$ and the quadrature branch input signal is $x_Q((n+m)T/M + \varepsilon T)$. The late signal (after downsampling by M to retain only the samples at index $n = Mk$) is $x_I((k + \frac{m}{M} + \varepsilon)T)$ for the in phase branch and $x_Q((k + \frac{m}{M} + \varepsilon)T)$ for the quadrature branch. The early signals (again after downsampling by M) are $x_I((k - \frac{m}{M} + \varepsilon)T)$ and $x_Q((k - \frac{m}{M} + \varepsilon)T)$. The decision variables are $x_I(kT + \varepsilon T)$ and $x_Q(kT + \varepsilon T)$.

The output of the in phase detector is denoted by $\hat{\varepsilon}_I[k]T$ and the output of the quadrature detector is denoted by $\hat{\varepsilon}_Q[k]T$.

The in phase early-late detector output is noisy due to the random nature of the data. A convenient representation for $\hat{\varepsilon}_I[k]T$ involves separating the noise component from the timing information. The timing information is provided by the S-curve of

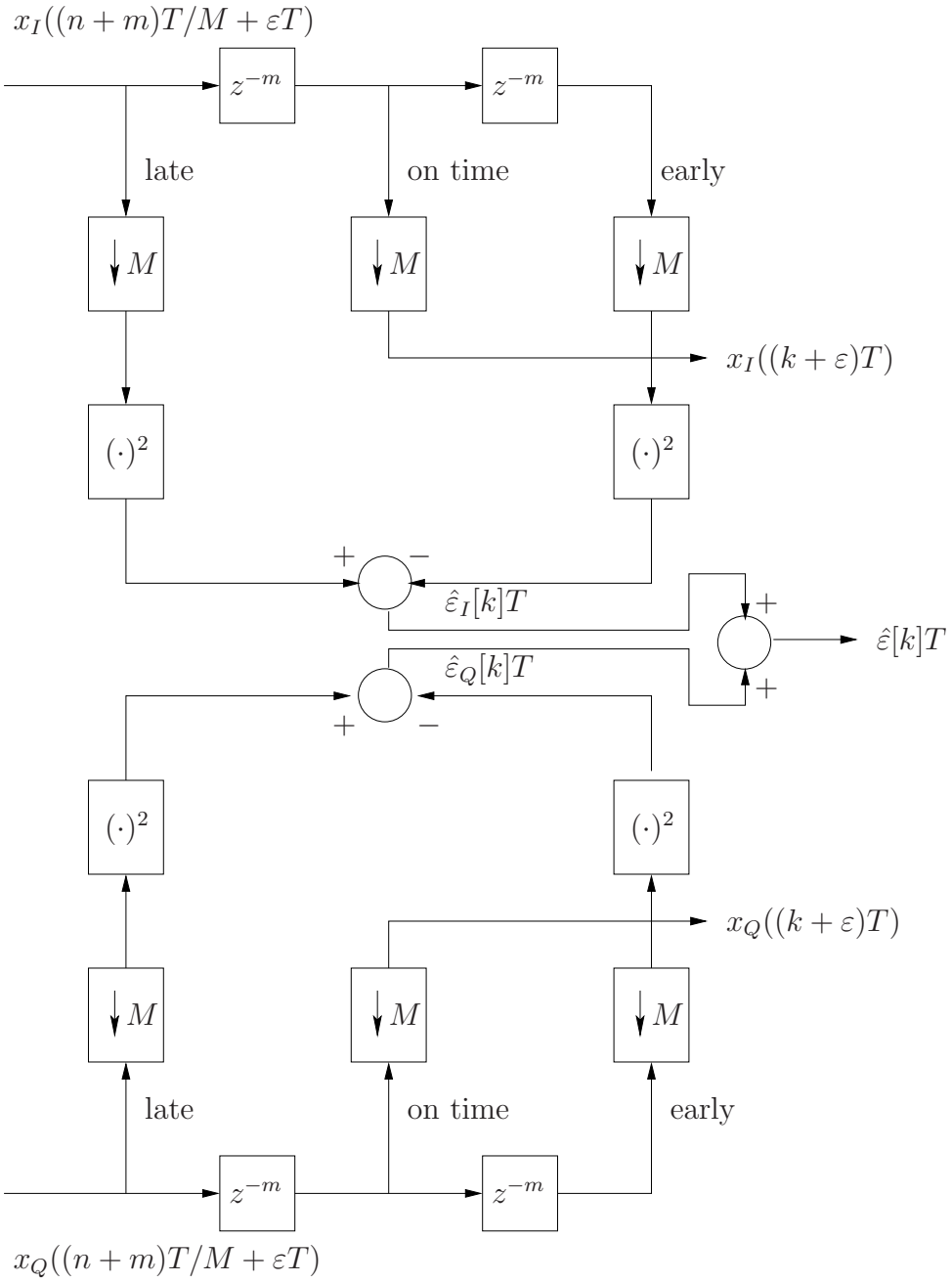

Figure 2.4 Early-late detector circuit.

the detector, and $\hat{\varepsilon}_I[k]T$ can be written as

$$\hat{\varepsilon}_I[k]T = g_I(\varepsilon T) + n_I(kT),$$

where $g_I(\varepsilon T)$ is the S-curve of the in phase detector evaluated at εT, and $n_I(kT)$ is the detector's self-noise, which is equal to $\hat{\varepsilon}_I[k]T - g_I(\varepsilon T)$. Other sources of noise, such as Additive White Gaussian Noise (AWGN), are normally present. The analysis that follows only considers self-noise, which is the dominant noise, and the AWGN has been neglected.

The S-curve is the expected value of the detector output and

$$g_I(\varepsilon T) = E\left\{x_I^2((k + \frac{m}{M} + \varepsilon)T)\right\} - E\left\{x_I^2((k - \frac{m}{M} + \varepsilon)T)\right\}, \tag{2.1}$$

where $E\{\cdot\}$ denotes the expectation operator.

Similarly the S-curve equation for the quadrature detector is given by

$$g_Q(\varepsilon T) = E\left\{x_Q^2((k + \frac{m}{M} + \varepsilon)T)\right\} - E\left\{x_Q^2((k - \frac{m}{M} + \varepsilon)T)\right\}, \tag{2.2}$$

and the S-curve for the combined detectors obtained by summing both outputs is

$$\begin{aligned} g(\varepsilon T) &= g_I(\varepsilon T) + g_Q(\varepsilon T) \\ &= E\left\{x((k + \frac{m}{M} + \varepsilon)T)x^*((k + \frac{m}{M} + \varepsilon)T)\right\} \\ &- E\left\{x((k - \frac{m}{M} + \varepsilon)T)x^*((k - \frac{m}{M} + \varepsilon)T)\right\} \\ &= P((k + \frac{m}{M} + \varepsilon)T) - P((k - \frac{m}{M} + \varepsilon)T), \end{aligned} \tag{2.3}$$

where $x(t) = x_I(t) + j * x_Q(t)$ is the complex signal at the output of the matched filters, and $P(t) = E\{x(t)x^*(t)\}$ is the average power of $x(t)$ evaluated at t.

From (2.3) finding an equation for the S-curve, $g(\varepsilon T)$, boils down to finding an expression for the average power, $P(t)$, of $x(t)$. In the presence of a frequency

offset, Δf, the complex signal becomes $x(t)e^{j2\pi\Delta ft}$. The average power is then $E\{x(t)e^{j2\pi\Delta ft}x^*(t)e^{-j2\pi\Delta ft}\} = P(t)$, which is the average power of $x(t)$. This shows that the detector is insensitive to a frequency offset, and timing recovery can take place in presence of a frequency offset with no performance degradation.

2.3.1 Theoretical derivation of S-curve

An expression for the average power, $P(t)$, of the baseband QAM signal is obtained as follows.

$$\begin{aligned} P(t) &= E\{x(t)x^*(t)\} \\ &= E\{x_I^2(t)\} + E\{x_Q^2(t)\}. \end{aligned} \tag{2.4}$$

Since $x_I(t)$ and $x_Q(t)$ are independent with identical statistics then $P(t) = 2E\{x_I^2(t)\}$.

The continuous-time signal, $x_I(t)$, is given by

$$x_I(t) = \sum_{l=-\infty}^{+\infty} a[l]h(t - lT), \tag{2.5}$$

where $h(t)$ is the impulse response of the cascaded matched filters in the transmitter and receiver.

Replacing $x_I(t)$ in $P(t)$ by the expression for $x_I(t)$ given in (2.5) produces

$$P(t) = 2E\left\{\left[\sum_{l=-\infty}^{+\infty} a[l]h(t - lT)\right]^2\right\}. \tag{2.6}$$

Expanding the sums and using the linearity property of the expectation operator yields

$$P(t) = 2\sum_{l=-\infty}^{+\infty}\sum_{m=-\infty}^{+\infty} E\{a[l]a[m]\}h(t - lT)h(t - mT). \tag{2.7}$$

The symbols $(a[k], b[k])$ are independent and

$$E\{a[l]a[m]\} = \begin{cases} 0, & l \neq m \\ \sigma_a^2, & l = m, \end{cases}$$

so

$$P(t) = 2\sigma_a^2 \sum_{l=-\infty}^{+\infty} h^2(t - lT). \tag{2.8}$$

From (2.8) $P(t) = P(t+T)$ so $P(t)$ is periodic with period T and $P(\varepsilon T) = P(kT + \varepsilon T)$. From (2.8)

$$P(\varepsilon T) = 2\sigma_a^2 \sum_{l=-\infty}^{+\infty} h^2((l+\varepsilon)T). \tag{2.9}$$

From Parseval's theorem [56] with the integration over 2π beginning at $-(1-r)\pi$

$$P(\varepsilon T) = \frac{2\sigma_a^2}{2\pi} \int_{-(1-r)\pi}^{(1+r)\pi} |H(e^{j\omega}; \varepsilon T)|^2 d\omega, \tag{2.10}$$

where $H(e^{j\omega}; \varepsilon T)$ is the Discrete-Time Fourier Transform (DTFT) of $h((l+\varepsilon)T)$. A closed-form expression for $H(e^{j\omega}; \varepsilon T)$ is derived in Appendix B for the case that $h(t)$ is a square-root raised cosine pulse.

Using (B.4) in Appendix B the integrand in (2.10) can be expressed as

$$|H(e^{j\omega}; \varepsilon T)|^2 = \begin{cases} 1, & -(1-r)\pi \leq \omega \leq (1-r)\pi, \\ \cos^2(\pi \dfrac{\varepsilon T}{T}) + \sin^2(\pi \dfrac{\varepsilon T}{T}) \sin^2(\dfrac{\pi}{2r}(\dfrac{\omega}{\pi} - 1)), & (1-r)\pi \leq \omega \leq (1+r)\pi. \end{cases} \tag{2.11}$$

Substituting (2.11) into (2.10) results in the closed-form expression for $P(\varepsilon T)$

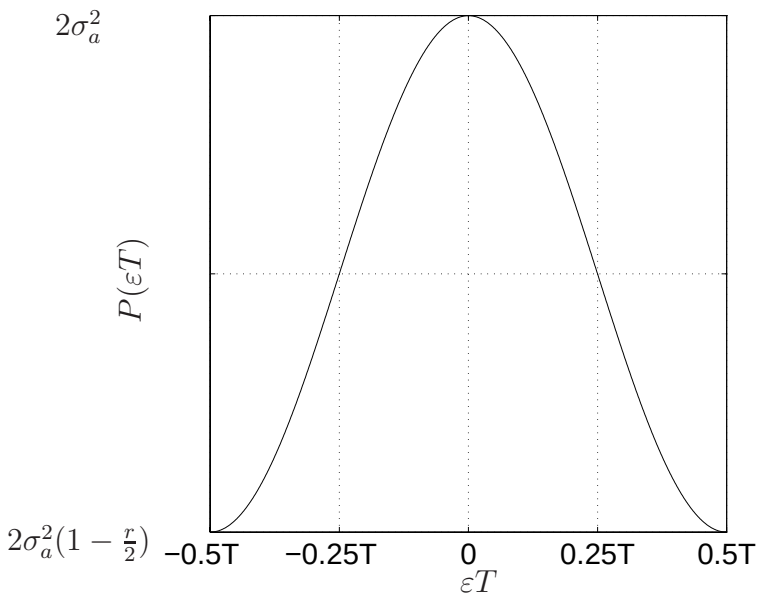

Figure 2.5 QAM signal average power curve as a function of εT.

given by

$$\begin{aligned} P(\varepsilon T) &= 2\sigma_a^2 \left[\frac{1}{2\pi} \int_{-\pi(1-r)}^{\pi(1-r)} 1 d\omega \right. \\ &\quad \left. + \frac{1}{2\pi} \int_{\pi(1-r)}^{\pi(1+r)} \cos^2(\pi \frac{\varepsilon T}{T}) + \sin^2(\pi \frac{\varepsilon T}{T}) \sin^2(\frac{\pi}{2r}(\frac{\omega}{\pi} - 1)) d\omega \right] \\ &= 2\sigma_a^2 \left[1 - \frac{r}{2} \sin^2(\pi \frac{\varepsilon T}{T}) \right]. \end{aligned} \tag{2.12}$$

A plot of the average power, $P(\varepsilon T)$, as a function of εT is shown in Figure 2.5. The average power is maximum at $\varepsilon T = 0$ (instant of time when the eye is maximally opened), is even about $\varepsilon T = 0$, and is decreasing for $|\varepsilon T| < 0.5T$. The early-late detector exploits the property that the average power of the QAM signal is an even concave down function around the correct decision time.

A closed form expression for the S-curve can now be derived using (2.12).

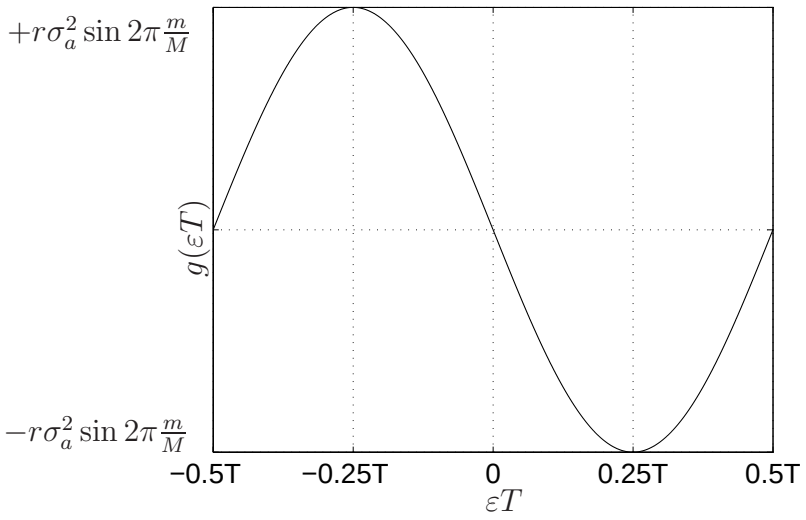

Figure 2.6 S-curve of the detector.

From (2.12) and (2.3) the S-curve of the detector is given by

$$g(\varepsilon T) = -r\sigma_a^2 \left[\sin^2\left(\pi\left(\frac{\varepsilon T}{T} + \frac{m}{M}\right)\right) - \sin^2\left(\pi\left(\frac{\varepsilon T}{T} - \frac{m}{M}\right)\right)\right] \tag{2.13}$$

After applying the trigonometric identities $\sin^2(a) = \frac{1}{2} - \frac{1}{2}\cos(2a)$ and $\cos(a \pm b) = \cos(a)\cos(b) \mp \sin(a)\sin(b)$, (2.13) reduces to

$$g(\varepsilon T) = -r\sigma_a^2 \sin(2\pi\frac{m}{M}) \sin(2\pi\frac{\varepsilon T}{T}). \tag{2.14}$$

A plot of the S-curve, $g(\varepsilon T)$, as a function of εT is shown in Figure 2.6. The S-curve is the same, except for a scaling factor, as the curve obtained in the case of the deterministic symbol pattern of $+1, -1$ (see Figure 2.2 on page 36). From (2.14) the scaling factor depends on the variance of the transmitted symbols, the ratio $\frac{m}{M}$, and the roll off factor, but is not affected by the order of the modulation.

2.4 Novel self-noise reduction technique for the early-late detector

2.4.1 Enhancing the early-late detector

The frequency response of an undersampled (sampled at the symbol rate) raised cosine impulse response is given in (B.4). From (2.11), it can be seen that $|H(e^{j\omega};\varepsilon T)|^2$ only depends on εT in the interval $(1-r)\pi \leq \omega \leq (1+r)\pi$ radians/sample. The latter means that the power in the frequency band from $-(1-r)\pi$ to $(1-r)\pi$ radians/sample is independent of the sample time. Suppressing the early and late signals in that frequency band does not change the difference, $P((\varepsilon+\frac{m}{M})T) - P((\varepsilon-\frac{m}{M})T)$, and therefore does not change the S-curve of the detector.

If the detector is enhanced with ideal high-pass filters placed after the downsamplers but prior to the squarer as illustrated in Fig. 2.7, and if the ideal high-pass filters have pass band corner at $(1-r)\pi$ radians/sample, then the term, $\int_{-\pi(1-r)}^{\pi(1-r)} 1 d\omega$, in (2.12) is replaced with $\int_{-\pi(1-r)}^{\pi(1-r)} 0 d\omega$, and the average power, which applies to the signals inside the enhanced detector, is equal to

$$P_E(\varepsilon T) = 2\sigma_a^2[r - \frac{r}{2}\sin^2(\pi\frac{\varepsilon T}{T})], \tag{2.15}$$

where the subscript E symbolizes enhanced.

Since $P_E(\varepsilon T)$ and $P(\varepsilon T)$ only differ by the constant $2\sigma_a^2(1-r)$, the difference, $P_E((\varepsilon+\frac{m}{M})T) - P_E((\varepsilon-\frac{m}{M})T)$, is equal to the difference, $P((\varepsilon+\frac{m}{M})T) - P((\varepsilon-\frac{m}{M})T)$. Therefore the S-curve for the enhanced detector is the same and is given by (2.14). However the average power is reduced by $2\sigma_a^2(1-r)$, which translates into a significant reduction in self-noise as discussed in Section 2.4.3.

2.4.2 Verification of theoretical results

Equation (2.14) was verified with a computer simulation using the Simulink/Matlab program for both the early-late and enhanced early-late detectors.

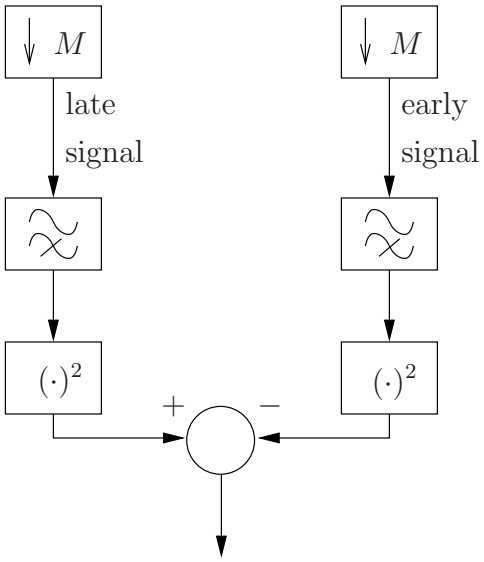

Figure 2.7 Early-late detector enhanced with high-pass filters.

The in phase and quadrature components of a 64QAM signal were generated with four samples per symbol (i.e., $M = 4$). The early and late signals were taken from samples adjacent to the decision variables (i.e., $m = 1$). The roll off factor was set to $r = 0.1$. The symbols, $(a[k], b[k])$, were mutually independent with $a[k]$ and $b[k]$ uniformly distributed over the alphabet $\{-7, -5, -3, -1, 1, 3, 5, 7\}$.

To validate (2.14) the simulation was performed with a nearly ideal high-pass filter placed in the early-late detector (see Figure 2.7 for the placement of the high-pass filters). The high-pass filter does not require a linear phase response since the detector estimates the timing offset with a power measurement (see (2.10)). The high-pass filter was implemented with an efficient structure, specifically a 12^{th} order elliptic filter with a natural frequency of $(1 - r)\pi = 0.9\pi$ radians/symbol, 0.1 dB ripple in the pass-band, and 60 dB attenuation in the stop-band. The frequency response of the filter is shown in Figure 2.8.

The 64QAM signal was generated with a timing offset. The timing offset was varied from $-0.5T$ to $0.5T$ seconds in steps of $0.0625T$ seconds. A Plot of the S-curve and the simulation results is shown in Fig. 2.9. The simulation results for the

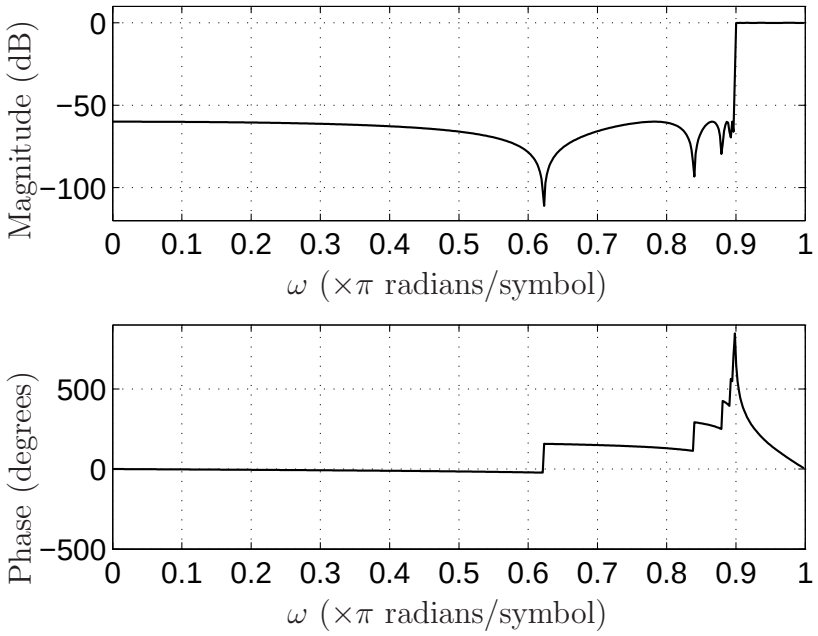

Figure 2.8 Frequency response of the 12^{th} order elliptic filter.

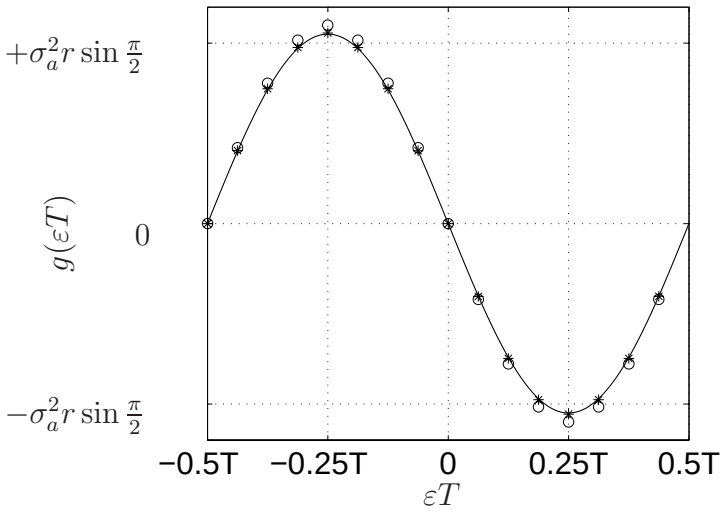

Figure 2.9 S-curve of the detector with two sets of simulation results marked with '*' and 'o'.

early-late detector are marked with a star. The simulation results for the enhanced early-late detector are marked with a circle. Each point is the average of $500,000$ detector outputs. Close agreement between simulation and theoretical results confirm the validity of the theoretical results.

2.4.3 Practical implementation of the enhanced early-late detector

The early-late detector is operated inside a feedback loop. Enhancing the early-late detector with high-order high-pass filters will affect the stability of the loop in addition to increasing the complexity of the implementation. A more practical approach is to approximate the ideal high-pass filter with a single-pole high-pass filter to enhance the detector. Four single-pole filters are required, two for the in phase detector (one to filter the early signal and another one to filter the late signal) and two for the quadrature detector.

In this Section the timing error variance of the enhanced early-late detector is measured with a computer simulation, and compared to that of the conventional early-late detector (i.e., detector with no enhancement in the form of high-pass filters). The measurement is performed by applying a digital QAM signal with no timing offset (i.e., $\varepsilon T = 0$) to the early-late detector circuit shown in Figure 2.4 on page 39. The measurement performed is not the same as measuring the timing jitter of the closed loop system (early-late detector operated in a feedback loop) since the filtering effect of the loop is not taken into account in this measurement. However such measurement is performed to isolate the performance of the enhanced detector. The performance of the enhanced detector in a closed-loop system is the object of Chapter 3.

Self-noise is normally reduced by adding a low-pass filter at the output of the detector. In the closed-loop system the feedback loop acts as the low-pass filter. To better assess the improvement gained by adding filters to the detector's structure, the simulations are performed by placing a low-pass filter at the detector's output. The timing error variance is measured by estimating the variance at the output of the

low-pass filter, and dividing it by the square of the slope of the S-curve at $\varepsilon T = 0$ to obtain a measurement with units T^2. The input signal was a 64QAM signal generated with random data, and with 4 samples per symbol interval.

The low-pass filter was a single-pole low-pass filter. Simulations were performed by varying the bandwidth of the low-pass filter from 0.12 radians/symbol-interval down to 0.05 radians/symbol-interval. In terms of the position of the pole in the z-plane, the pole was moved from $z_{\text{LPF}} = 0.88$ to $z_{\text{LPF}} = 0.98$ in steps of 0.01.

One set of measurement was generated with the conventional detector, and four sets of measurements were generated with the enhanced detector. The pole of the single-pole high-pass filters in the enhanced detector was placed at $z = -0.85$ for the first set of measurements, at $z = -0.9$ for the second set, and $z = -0.95$ for the third set of measurements. The fourth set of measurements used a 12^{th} order elliptic (high-pass) filter, i.e., the filter used in Section 2.4.2 to approximate an ideal high-pass filter.

The variance of the (zero-mean) output of the low-pass filter was estimated by squaring and averaging $500,000$ outputs. Dividing it by the square of the slope of the S-curve at $\varepsilon T = 0$ was straightforward in the case of the conventional system since the S-curve equation was known. In the case of the enhanced system, the S-curve slope at $\varepsilon T = 0$ was determined through simulations. In contrast with the ideal high-pass filter, the single-pole high-pass filter alters the S-curve because its magnitude response is not constant for $(1-r)\pi < \omega < \pi$ radians/sample. This means that some timing information is lost when filtering the detector's signals.

The measurements obtained with the conventional detector were used as a reference to determine the improvement in performance (in dB) obtained with the enhanced detector.

In Figure 2.10 the improvements in dB (reduction of the timing error variance) obtained with the enhanced detectors are plotted against the bandwidth of the low-pass filter following the detector. Four curves are shown. The dotted curve, which

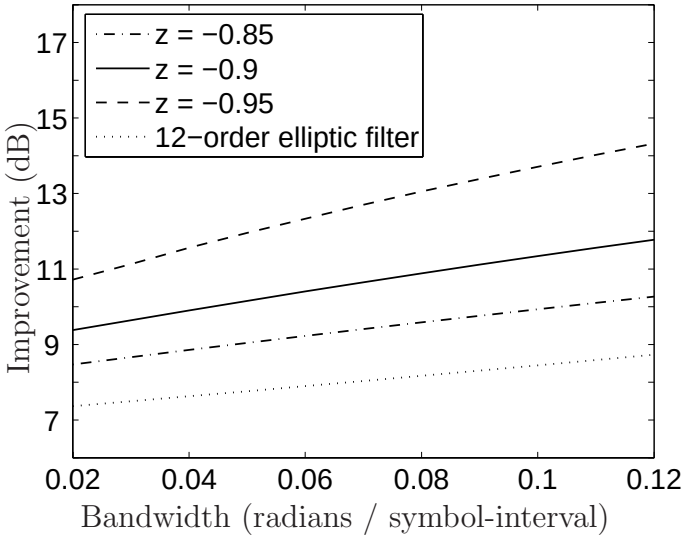

Figure 2.10 Performance of enhanced detector as a function of the bandwidth of the low-pass filter.

is at the bottom, is the improvement in performance when the 12^{th} order high-pass filter is used. The three other curves show the increase in performance when the single-pole high-pass filters are used. The dash-dotted curve shows the improvement when the pole is placed at $z = -0.85$. The solid line shows the improvement when the pole is at $z = -0.9$, and the top curve (dashed line) shows the improvement when the pole is located at $z = -0.95$.

Significant reduction in timing jitter is obtained by enhancing the detector with single-pole high-pass filters. This graph shows that improvement is gained even when the low-pass filter has a bandwidth of 0.3 % of the symbol rate. The increase in performance is significantly better with the single-pole high-pass filter than with the 12^{th} order elliptic filter despite the loss in timing information resulting from using that filter. Also, the performance increases as the pole is moved toward $z = -1$. This suggests that most of the timing information is concentrated near $\omega = \pi$ radians / symbol-interval.

2.5 Steady state self-noise analysis

The improvement in self-noise reduction is also assessed by finding a closed-form expression for the steady state self-noise of the enhanced detector. To simplify the analysis, an ideal high-pass filter is considered in place of the single-pole high-pass filter. The analysis that follows assumes the timing offset is zero, i.e., $\varepsilon T = 0$. The detector's output, in the absence of AWGN, is self-noise only. This output is given by

$$\begin{aligned} y_{sn}(kT) &= n_I(kT) + n_Q(kT) \\ &= x_I^2((k+\frac{m}{M})T) + x_Q^2((k+\frac{m}{M})T) - x_I^2((k-\frac{m}{M})T) - x_Q^2((k-\frac{m}{M})T). \end{aligned} \tag{2.16}$$

An expression for the steady state self-noise power spectrum is obtained by evaluating an ensemble average in the frequency domain [57]. The power spectrum of the self-noise, denoted by $S_{sn}(e^{j\omega})$, is given by

$$S_{sn}(e^{j\omega}) = \lim_{N\to\infty} \frac{1}{2N+1} E\{|Y_{sn}(e^{j\omega})|^2\}, \tag{2.17}$$

where $Y_{sn}(e^{j\omega}) = \sum_{k=-N}^{N} y_{sn}(kT)e^{-j\omega k}$ is the discrete-time Fourier Transform of $y_{sn}(kT)$ truncated at $k = \pm N$. It is shown in Appendix C that

$$\begin{aligned} S_{sn}(e^{j\omega}) = \sigma_d^4 \Bigg\{ &\frac{2}{\pi} \int_{-\pi}^{\pi} \left[U_+(\theta,\omega) - U_-(\theta,\omega)\right] \left[U_+(\theta,\omega) - U_-(\theta,\omega)\right]^* d\theta \\ &- \frac{12(A+1)}{5(A-1)} \left| H_+(e^{j\omega}) \otimes H_+(e^{j\omega}) - H_-(e^{j\omega}) \otimes H_-(e^{j\omega}) \right|^2 \Bigg\}, \end{aligned} \tag{2.18}$$

where $\otimes$ denotes the circular convolution operation, the star, *, denotes the conjugate,
$U_+(\theta,\omega) = H(e^{j\theta}; +\frac{m}{M}T)H(e^{j(\omega-\theta)}; +\frac{m}{M}T)$,
$U_-(\theta,\omega) = H(e^{j\theta}; -\frac{m}{M}T)H(e^{j(\omega-\theta)}; -\frac{m}{M}T)$, $H_+(e^{j\omega}) = H(e^{j\omega}; +\frac{m}{M}T)$,
$H_-(e^{j\omega}) = H(e^{j\omega}; -\frac{m}{M}T)$, and A is the modulation order (i.e., $A = 64$ for 64QAM).

A closed-form expression for (2.18) was derived for the early-late detector en-

hanced with an ideal high-pass filter. It is derived under the restriction that the roll off factor is less than 0.5, i.e., $r \leq 0.5$. With $r \leq 0.5$, the circular convolutions in (2.18) reduce to linear convolutions, which make the mathematic easier to manage.

The details of the derivations are given in Appendix D. The expression obtained is

$$
S_{sn}(e^{j\omega}) = \begin{cases}
\sigma_d^4 \times \frac{r}{\pi} \left\{ \left[p_1(\frac{m}{M}) + p_2(\frac{m}{M}) \cos(\frac{\omega}{r}) \right] \left[2\pi - \frac{|\omega|}{r} \right] \right. \\
- \left[p_3(\frac{m}{M}) + p_2(\frac{m}{M}) \cos(\frac{\omega}{r}) + p_4(\frac{m}{M}) \cos(\frac{\omega}{2r}) \right] \cos(2\frac{m}{M}\omega) \left[2\pi - \frac{|\omega|}{r} \right] \\
- \left[p_5(\frac{m}{M}) + p_6(\frac{m}{M}) \cos(2\frac{m}{M}\omega) + p_7(\frac{m}{M}) \sin(2\frac{m}{M}|\omega|) \right] \sin(\frac{|\omega|}{r}) \\
\left. - \left[-2p_4(\frac{m}{M}) \cos(2\frac{m}{M}\omega) + p_8(\frac{m}{M}) \sin(2\frac{m}{M}|\omega|) \right] \sin(\frac{|\omega|}{2r}) \right\} \\
-\sigma_A^4 \times \frac{12(A+1)}{5\pi^2(A-1)} \left\{ \left[p_9(\frac{m}{M}) + p_{10}(\frac{m}{M}) \cos(\frac{\omega}{2r}) \right] [2r\pi - |\omega|] \sin(\frac{m}{M}|\omega|) \right. \\
\left. - \left[2p_{10}(\frac{m}{M}) \sin(\frac{m}{M}|\omega|) + p_{11}(\frac{m}{M}) \cos(\frac{m}{M}\omega) \right] r \sin(\frac{|\omega|}{2r}) \right\}^2, \qquad |\omega| < 2r\pi, \\
0, \qquad 2r\pi \leq |\omega| < \pi,
\end{cases}
\tag{2.19}
$$

where

$$
\begin{aligned}
& r \leq 0.5, \\
p_1(\frac{m}{M}) &= \cos^4(\pi\frac{m}{M}) + 2\cos^2(\pi\frac{m}{M}) + 1, \\
p_2(\frac{m}{M}) &= \frac{1}{2}\cos^4(\pi\frac{m}{M}) - \cos^2(\pi\frac{m}{M}) + \frac{1}{2}, \\
p_3(\frac{m}{M}) &= 9\cos^4(\pi\frac{m}{M}) - 6\cos^2(\pi\frac{m}{M}) + 1, \\
p_4(\frac{m}{M}) &= -8\cos^4(\pi\frac{m}{M}) + 8\cos^2(\pi\frac{m}{M}), \\
p_5(\frac{m}{M}) &= -\frac{3}{2}\cos^4(\pi\frac{m}{M}) - \cos^2(\pi\frac{m}{M}) + \frac{5}{2}, \\
p_6(\frac{m}{M}) &= -\frac{13}{2}\cos^4(\pi\frac{m}{M}) + 9\cos^2(\pi\frac{m}{M})) - \frac{5}{2}, \\
p_7(\frac{m}{M}) &= \frac{32}{3}\sin(\pi\frac{m}{M}) \left(-\cos^3(\pi\frac{m}{M}) + \cos(\pi\frac{m}{M}) \right), \\
p_8(\frac{m}{M}) &= \frac{32}{3}\sin(\pi\frac{m}{M}) \left(4\cos^3(\pi\frac{m}{M}) - \cos(\pi\frac{m}{M}) \right),
\end{aligned}
$$

$$p_9(\frac{m}{M}) = \cos^2(\pi\frac{m}{M}),$$
$$p_{10}(\frac{m}{M}) = -\frac{1}{2}\cos^2(\pi\frac{m}{M}) + \frac{1}{2},$$
$$p_{11}(\frac{m}{M}) = 4\cos(\pi\frac{m}{M})\sin(\pi\frac{m}{M}).$$

The validity of (2.19) was verified with a computer simulation. The system described in Section 2.4.3 was simulated to estimate the steady state self-noise power spectrum of the early-late detector when it is enhanced with the high-pass 12^{th} order filter whose frequency response was plotted in Figure 2.8 on page 47. The data was collected at the output of the detector prior to the low-pass filter.

The spectrum was estimated using Welch's 50% overlapping method with Blackman windowed blocks of length 8192 symbol intervals [58]. The Blackman window was chosen to largely decrease the ripple in the stop band. The spectrum estimate is plotted in Fig. 2.11 (solid curve) along with the theoretical curve (dashed line) for an ideal high-pass filter. The close agreement between the curves strongly suggests that (2.19) is correct.

An approximation to the steady state self-noise for small ω can be obtained with a second-order MacLaurin Series. This approximation has only a second order term since $S_{sn}(e^{j\omega})$ and its first derivative are zero at $\omega = 0$. The approximation is

$$S_{sn}(e^{j\omega}) \approx \left(\frac{p_{12}(\frac{m}{M})}{r} + p_{13}(\frac{m}{M}) + \frac{A+1}{A-1}p_{14}(\frac{m}{M}) + \left(p_{15}(\frac{m}{M}) + \frac{A+1}{A-1}p_{16}(\frac{m}{M})\right)r + \frac{A+1}{A-1}p_{17}(\frac{m}{M})r^2\right)\omega^2, \tag{2.20}$$

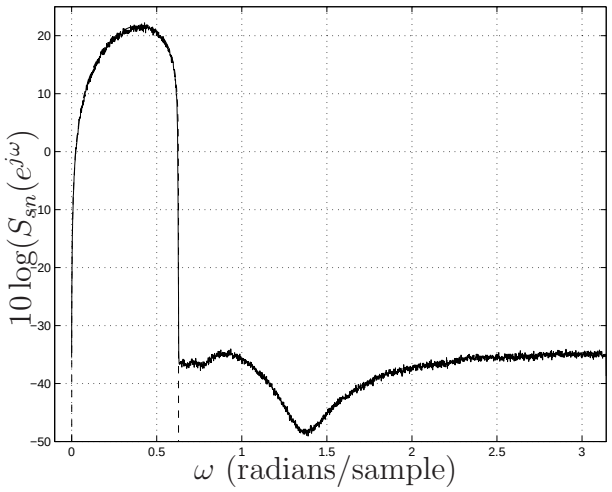

Figure 2.11 Power spectra of early-late detectors enhanced with ideal (dashed curve) and real (solid curve) high-pass filters with $m = 1$, $M = 4$, $r = 0.1$, and $A = 64$.

where

$$
\begin{aligned}
p_{12}(\frac{m}{M}) &= -2\cos^4(\pi\frac{m}{M}) + 2\cos^2(\pi\frac{m}{M}),\\
p_{13}(\frac{m}{M}) &= -\frac{32m}{3\pi M}\sin(\pi\frac{m}{M})\left(2\cos^3(\pi\frac{m}{M}) + \cos(\pi\frac{m}{M})\right),\\
p_{14}(\frac{m}{M}) &= -\frac{48}{5\pi^2}\left(-\cos^4(\pi\frac{m}{M}) + \cos^2(\pi\frac{m}{M})\right),\\
p_{15}(\frac{m}{M}) &= \left(\frac{m}{M}\right)^2\left(6\cos^4(\pi\frac{m}{M}) + 4\cos^2(\pi\frac{m}{M}) + 6\right),\\
p_{16}(\frac{m}{M}) &= \frac{48m}{5\pi M}\sin(\pi\frac{m}{M})\left(\cos^3(\pi\frac{m}{M}) + \cos(\pi\frac{m}{M})\right),\\
p_{17}(\frac{m}{M}) &= -\frac{12m^2}{5M^2}\left(\cos^2(\pi\frac{m}{M}) + 1\right)^2.
\end{aligned}
$$

For commonly used $\frac{m}{M} = \frac{1}{4}$, (2.20) reduces to

$$
S_{sn}(e^{j\omega}) \approx \left(\frac{1}{2r} - \frac{8}{3\pi} - \frac{12(A+1)}{5\pi^2(A-1)} + \left(\frac{19}{32} + \frac{9(A+1)}{5\pi(A-1)}\right)r - \frac{27(A+1)}{80(A-1)}r^2\right)\omega^2, \tag{2.21}
$$

for small ω.

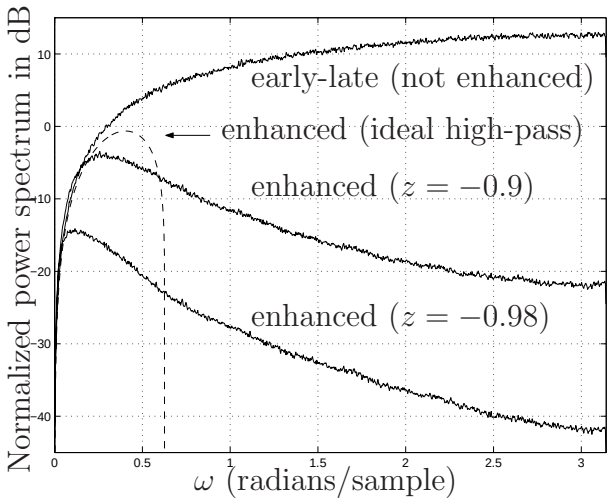

Figure 2.12 Power spectra of early-late detector and enhanced early-late detector when the pole is at $z = -0.9$ and $z = -0.98$ and $\frac{m}{M} = 0.25$, $r = 0.1$ and $A = 64$.

Fig. 2.12 shows the self-noise power spectra (after dividing by the square of the S-curve slope at $\varepsilon T = 0$) for both the early-late detector in its conventional form and in its enhanced form when the pole of the single-pole high-pass filters is placed at $z = -0.9$ and $z = -0.98$. All three power spectrum curves were obtained through simulations. The theoretical curve, which applies to an enhancement in the form of an ideal high-pass filter, is shown with a dashed line. Simulations showed that this theoretical curve approaches the curve for the conventional early-late detector as ω tends to 0. This means that equation (2.19) or the low-frequency approximations, (2.20) or (2.21), can be used to estimate the power spectrum of the self-noise in the conventional (not enhanced) early-late detector for ω near zero.

2.6 Applying the self-noise reduction technique to the Gardner detector

The early-late and the Gardner detectors operate on similar principles. The early-late detection exploits the property that the average power of the QAM signal is an even concave down function about the correct decision times (Figure 2.5 on page 43). The Gardner detector exploits the property that the average power of the QAM signal

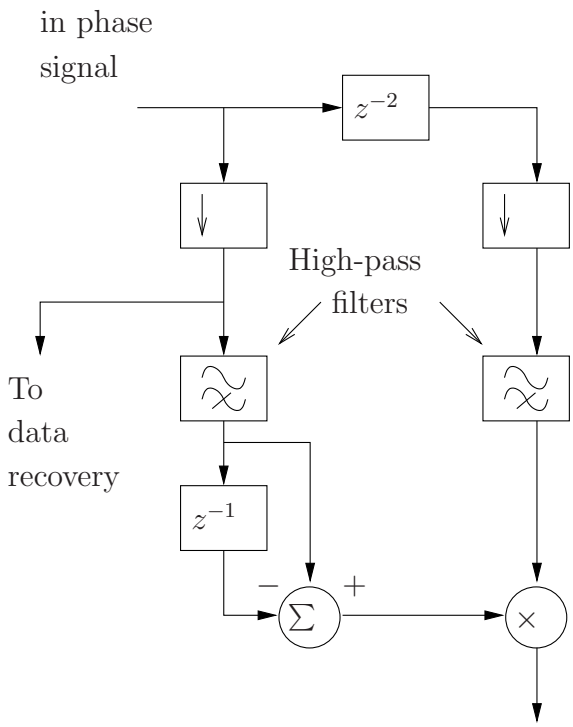

Figure 2.13 Gardner detector enhanced with high-pass filters.

is an even concave up function around the time midway between correct decision times. Since both estimators use the power curve, the proposed enhancement for the early-late detector can also be applied to the Gardner detector. Figure 2.13 shows where the high-pass filters are placed inside the Gardner detector.

3. Performance of Enhanced Synchronizers and Other Feedback Systems

3.1 Introduction

The primary objective of this chapter is to evaluate the performance of the enhanced early-late detector in closed-loop operation. The early-late detector provides timing estimates at the symbol rate, which are processed by the loop filter before being used to control the resampler. The primary interest of this thesis is the steady state operation, i.e., timing has been acquired and the resampling rate is synchronized to (an exact multiple of) the symbol rate.

The quality of the enhanced detector is assessed by using the variance of the timing jitter as the performance measure. A simulation of the timing recovery loop using the Simulink / Matlab software is performed to determine at the symbol rate the timing error of the resampled signal after the loop has reached steady state. A large number of measurements are collected to obtain an accurate estimate of the timing jitter variance.

Also in Chapter 3 the performance of the enhanced detector is compared to the performance of other feedback systems. To establish fair comparisons among the different systems, the systems are operated with identical noise bandwidths. Building a loop to operate at a given bandwidth is a tedious task especially if the order of the loop is high. Design equations and algorithms are provided to relate the parameters of the feedback loop to the closed-loop bandwidth in the cases of first, second, and third-order loops.

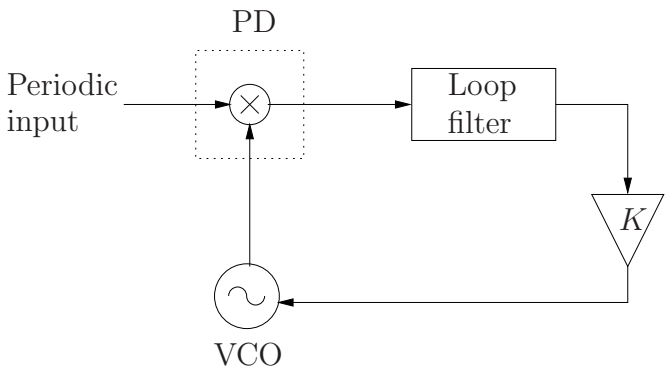

Figure 3.1 Analog phase-locked loop block diagram.

Chapter 3 is organized as follows. A description of the principle of operation of a timing recovery loop is given in Section 3.2. The mode of interest is steady state and the functional operation of the loop can be described with a linear model. Linear models for the non-linear detectors, which are the conventional, the enhanced early-late detectors, the Gardner detector and the enhanced Gardner detectors are given in Section 3.3. The systems of interest, which are described in Section 3.6, include loops of order 1, 2, and 3. Linear analyses of first, second, and third-order loops are given in Section 3.4. The results of a computer simulation to verify the validity of the loops and detector models are reported in Section 3.5. The performance results of the simulated systems are given in Section 3.6.

3.2 Principle of operation of a timing recovery loop

Insight into the functional operation of a digital timing recovery loop is gained by describing a classical analog phase-locked loop. The term "classical" refers to a loop that is used to recover a single tone.

A block diagram of a classical phase-locked loop is shown in Figure 3.1, where the block labeled PD is the phase detector and the block labeled VCO is the voltage-controlled oscillator. The PD produces an error signal by comparing the phase of the periodic input signal against the phase of the VCO signal. This error signal is filtered by the loop filter. The filtered signal is used to adjust the frequency of the

VCO in a direction that reduces the phase error [59]. After the loop has locked, the error signal (PD output) has a DC component if the frequency of the input signal and the nominal frequency of the VCO (i.e., the frequency when the control voltage is 0) are not equal. This DC error serves to adjust the VCO frequency so it is the same as the frequency of the input. A phase difference between the input signal and the VCO output is necessary to generate the DC error.

A block diagram of a digital timing recovery loop is shown in Figure 3.2. In an actual QAM system the loop contains two resamplers, one to process the in phase signal and one to process the quadrature signal. Also there are two TEDs, one to produce a timing offset estimate of the signal at the output of the "in phase" resamper and one to produce a timing offset estimate of the signal at the output of the "quadrature" resampler. The sum of both estimates is fed to the loop filter. Here, the diagram is simplified by only showing one resampler and one TED.

The digital loop includes two closed-paths, labeled as primary path and secondary path. The primary path is the path that includes gain K. The secondary path is the path that includes gain K_2. All blocks in the primary path of the digital loop have an equivalent block in the analog loop. The equivalent of the loop filter and gain K blocks are obvious. The equivalent of the timing error detector (TED) is the phase detector (PD). The equivalent of the VCO takes the form of two blocks in the digital loop: the resampler block and the control block.

The TED, which is either the early-late or Gardner detector, estimates the time difference between the current sampling points and the correct sampling points. The TED's estimate is used to increase or decrease the rate at which the accumulator in the control block rolls over. This accumulator serves to generate the new sampling times. The roll over rate is increased or decreased in a direction that reduces the timing offset. As shown in Figure 3.2 the accumulator is incremented by 1 at each positive edge of the system clock, equal to $1/T_r$[1]. The value 1 corresponds to the VCO

[1]In reality, the accumulator is clocked at twice the sampling rate (i.e., $2/T_r$) to allow resampling at a faster rate than $1/T_r$. The explanation given here is simplified by only considering the case of

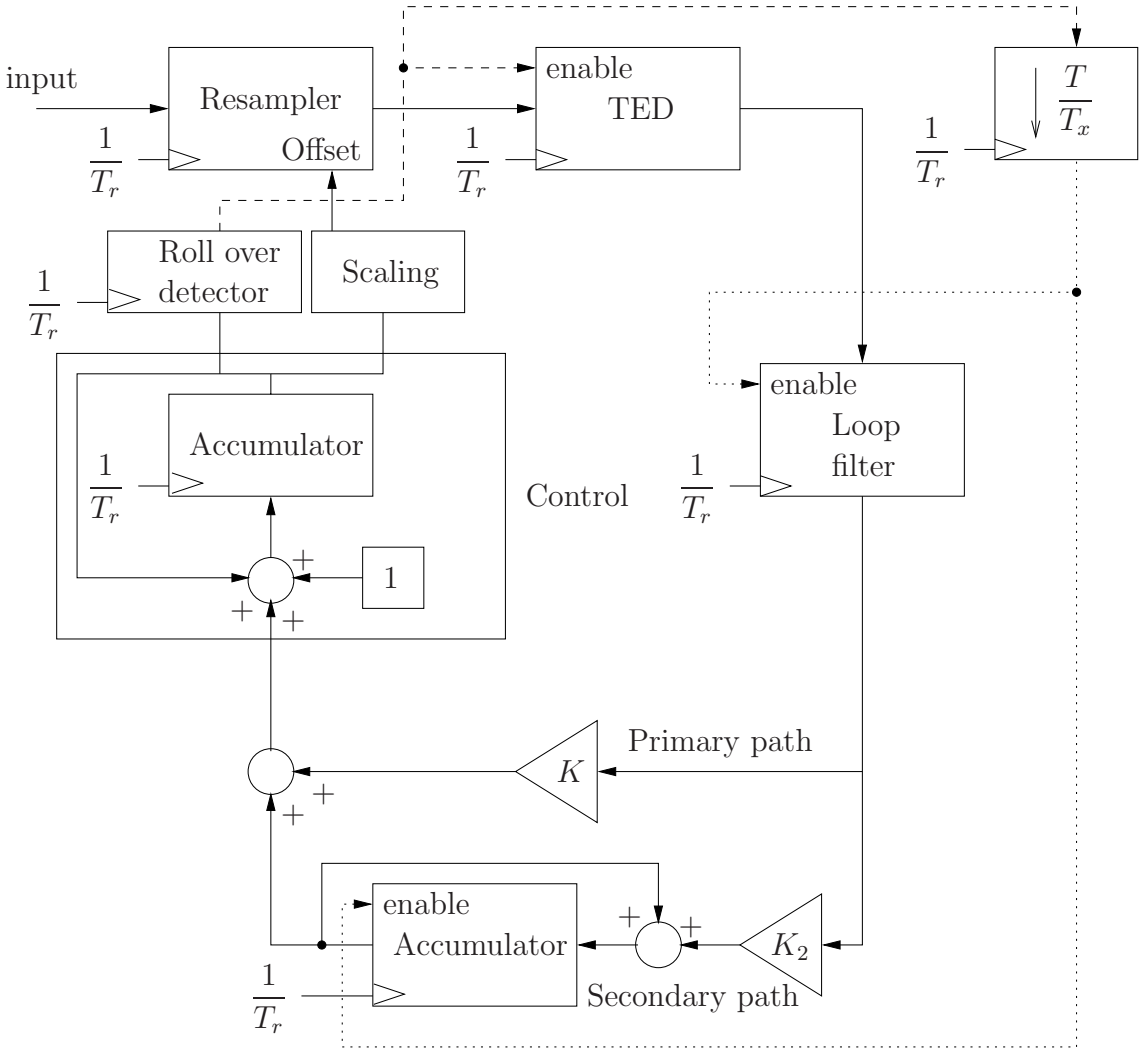

Figure 3.2 Digital timing recovery loop block diagram with synchronous blocks clocked at the receiver sampling rate.

center frequency of the analog phase-locked loop. The accumulator rolls over when its content is greater than or equal to 1. So if the input to the control block is zero, the accumulator exactly rolls over at the receiver sampling rate, and the resampling rate is equal to $1/T_r$.

By using a free-running oscillator to sample the received signal, sampling rates $1/T_r$ in the receiver and $1/T_x$ in the transmitter are close but not equal. Just as a DC error is necessary in the analog phase-lock loop system, a DC error is necessary to have the resampling rate equal to $1/T_x$. The accumulator located in the secondary path acquires this DC value. The DC value is not known at start up. The accumulator content slowly builds up during timing acquisition. Gain K_2 is much smaller than gain K so only a small portion of the timing offset estimate is used to update the accumulator at each sample. After timing has been acquired and the loop operates in steady state, the accumulator contains this DC value, which is equal to $(T_r/T_x - 1)$.

The accumulator in the control block generates the new sampling times, as explained in the following with the help of a graph.

The top graph in Figure 3.3 shows a ramp that is labeled "Transmitter ramp". This ramp is essentially a plot of the phase of the sampling clock in the transmitter, as a function of time. The phase, denoted by $\Phi_T(t)$, has unit of cycles, and increases by one (cycle) every T_x seconds so the slope of the ramp is equal to the sampling rate, $1/T_x$. This ramp could have been digitally generated in the transmitter (see points marked with an "x" on the graph) by using an accumulator that is incremented by one at each positive clock edge of the transmitter sampling clock, so each time a sample is generated in the transmitter.

To resample at a sampling rate of $1/T_x$ in the receiver, the accumulator in the control block, which is clocked at $1/T_r$, has to be incremented such that its output is a ramp that has a slope equal to the slope of the transmitter ramp. For a sampling rate, $\frac{1}{T_r} = \frac{3}{2}\frac{1}{T_x}$, a ramp with the same slope is generated if, at every positive edge

a resampling rate that is smaller than $1/T_r$.

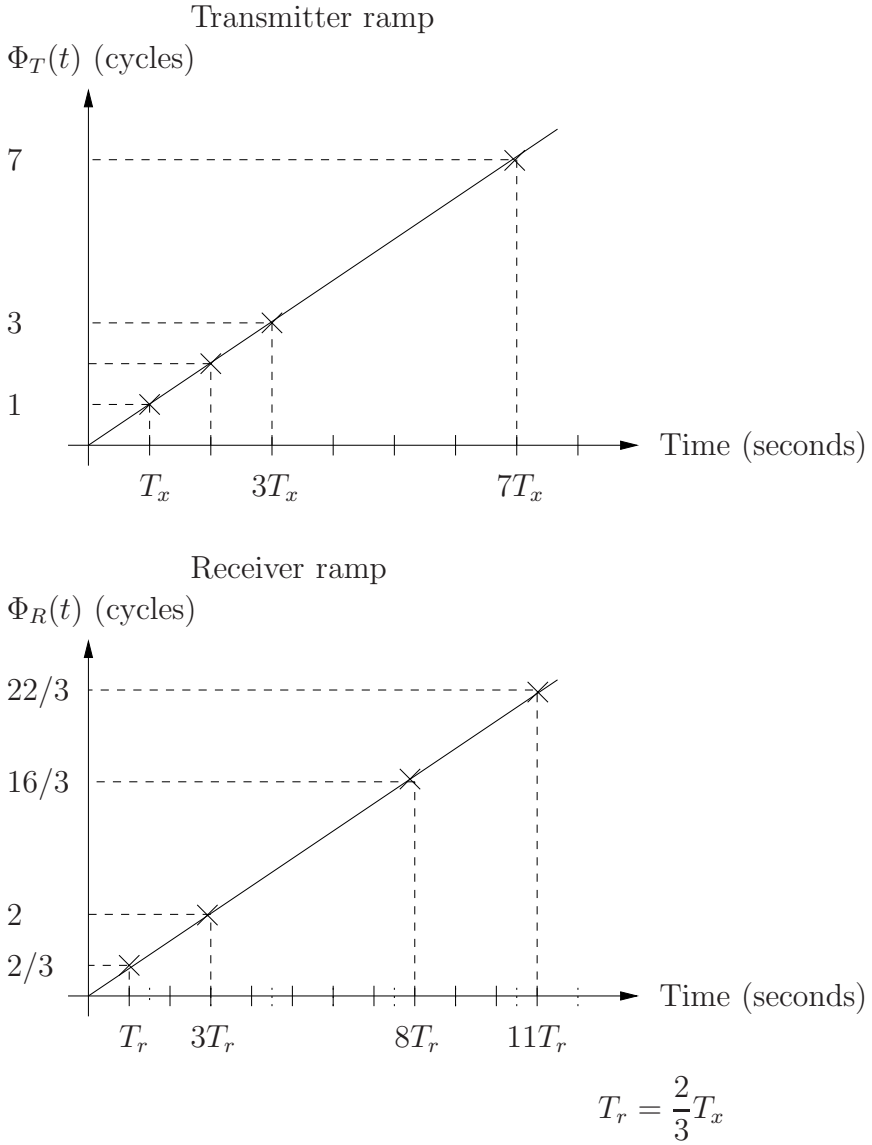

Figure 3.3 Phase ramps digitally produced in transmitter (top graph) and receiver (bottom graph) with samples marked with an "x".

of the receiver sampling clock, the accumulator is incremented by 2/3. The digital ramp obtained, which is shown in the bottom graph of Figure 3.3 (labeled "Receiver ramp") has the same slope as the transmitter ramp (top graph) although the ramp is evaluated at different instants of time, namely $T_r = \frac{2}{3}T_x, 2T_r = \frac{4}{3}T_x, 3T_r = \frac{6}{3}T_x, \ldots$. The phase in the receiver is denoted Φ_R.

The resampling is implemented as follows. The accumulator rolls over every time its content becomes greater than or equal to 1, and only stores the fractional part of Φ_R. The resampler is a time-variant filter whose coefficients are set when the accumulator rolls over. The remainder (content of accumulator after it rolls over) gives the position of the new sample with respect to the received sample, and is used to set the filter's coefficients. For example, with $T_r = (2/3)T_x$, the counter rolls over at $2T_r$, and its content is 1/3 (see bottom graph of Figure 3.3). This indicates the new sample is located $\frac{1}{3}T_x$ seconds in time before the received sample. Unfortunately the time unit in the receiver is T_r and not T_x, so a time conversion is needed to find the position of the new sample relative to the received sample. Since $T_r/T_x = 2/3$ (given by the accumulator in the second path), the new sample is located $(1/3) \times (3/2)T_r = (1/2)T_r$ seconds before the received sample so is half-way between the received and previously received samples. The "Offset" input of the resampler is set to $-1/2$ in that example.

The roll over detector block in Figure 3.2 on page 60 generates a pulse when the accumulator rolls over. This pulse is used to enable the TED so the new sample produced by the resampler gets loaded in the TED's shift registers. The TED produces timing offset estimates at the symbol rate, $1/T$, so its output is only valid every T/T_x new samples. This means that the loop filter as well as the accumulator in the secondary path must be enabled only every T/T_x new samples. As illustrated in Figure 3.2, this is achieved with the use of a down-sampler by T/T_x. The input to the down-sampler is the roll over detector's signal. The down-sampler produces a pulse every $(T/T_x)^{\text{th}}$ input pulse.

This chapter is concerned with steady state operation, which occurs after the loop

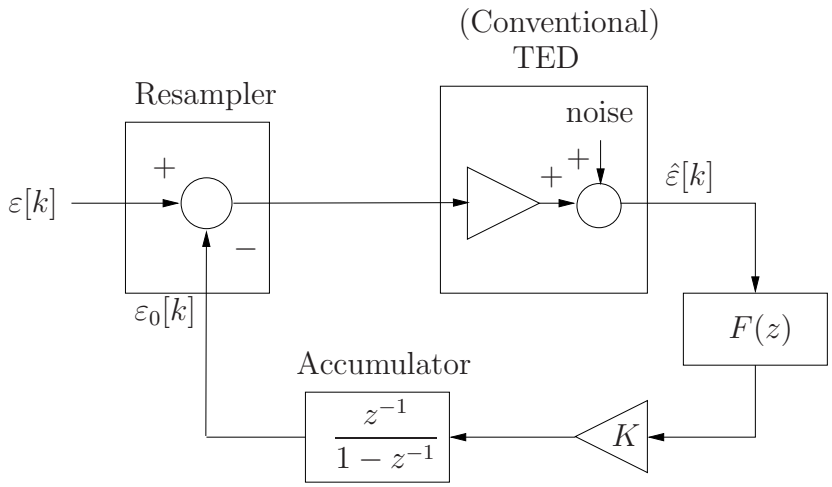

Figure 3.4 Linear model for digital timing recovery loop.

has converged and the accumulator in the secondary branch has settled. In this state, the resampling rate is $1/T_x$. The loop's behavior in steady state is not affected by taking $1/T_r = 1/T_x$ and setting the DC value (accumulator in secondary path) to zero. A noise model for the timing recovery loop when $1/T_r = 1/T_x$ is given in Figure 3.4, where the variable of interest is the timing offset, denoted by $\varepsilon[k]$. This timing offset is constant. A non-constant timing offset would imply that $1/T_r \neq 1/T_x$. In the rest of the chapter $T = 1$, and the timing offset is simply denoted by $\varepsilon[k]$ instead of $\varepsilon[k]T$. The output is denoted by $\varepsilon_0[k]$. The conventional early-late or Gardner TED is modeled as a gain, when in reality it is a non-linear device. The model for the enhanced detector includes a low-pass filter in addition to the gain, as explained in Section 3.3. The output of the detector is $\hat{\varepsilon}[k]$, and the AC component causes the jitter. The models for the resampler and accumulator are identified in Figure 3.4. Note that the secondary path of the timing recovery loop (see Figure 3.2 on page 60) is not modeled, since in steady state, the primary path contributes to the jitter, and the secondary path has very little effects on the jitter as gain $K_2 \ll K$.

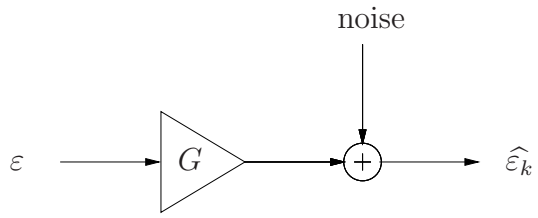

Figure 3.5 Linear model for non-data-aided TED used in a feedback loop.

3.3 Linear models for the detectors

In this section both the early-late and Gardner detectors are linearized. The function of the detector is to produce an output that is proportional to the timing offset. Therefore the input to the detector's model will be timing offset. The detector produces noise that is modeled as additive. The analysis of the early-late detector is done in Section 3.3.1. The analysis of the Gardner detector is carried in Section 3.3.2.

3.3.1 Early-late detector

A general model for a non-data-aided TED that is used in a feedback loop is given in [55]. This model is used in the sequel to derive models for the early-late detectors.

As illustrated in Figure 3.5, the model consists of a gain, G, and a source of noise. The gain, G, is the slope of the detector's S-curve at $\varepsilon = 0$. The input to the model is the timing offset, ε. $G \times \varepsilon$ models the signal component of the detector's output. The linear model for the conventional early-late detector is given in Figure 3.6, where from (2.14), $G = -2\pi r\sigma_d^2$ ($m = 1$ and $M = 4$).

The model for the enhanced detector differs from the model of the conventional detector. The incorporation of high-pass filters inside the detector (see Figure 2.7 on page 46) causes a delay in the response time when a change occurs. Following a change to the input timing offset, it takes some time for the signal component of the detector's output to settle to G times the new timing offset due to the latency introduced by the high-pass filters. This delay is modeled with the addition of an appropriate filter.

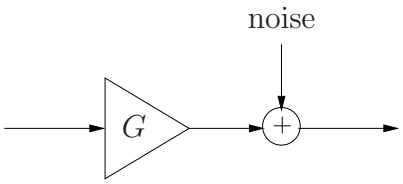

Figure 3.6 Linear model for conventional early-late detector where $G = -2\pi r\sigma_d^2$.

A convenient way to find the appropriate filter is to analyze the output of the detector for an input signal that does not produce self-noise. Recall from Section 2.2 that the detector output is noise-free if the input signal is a sinusoid with a frequency of π radians/symbol-interval, which can be represented by $\cos(\frac{\pi}{4}n+\pi\varepsilon)$ (see Figure 2.1 on page 35). For such an input the downsampled early and late signals are respectively

$$\begin{aligned}\text{early[k]} &= (-1)^k \cos(-\frac{\pi}{4} + \pi\varepsilon)\\ \text{late[k]} &= (-1)^k \cos(\frac{\pi}{4} + \pi\varepsilon).\end{aligned}$$

For small timing offset the output of the early-late detector is

$$\begin{aligned}\widehat{\varepsilon_k} &= \text{late}^2\text{[k]} - \text{early}^2\text{[k]}\\ &= \cos^2\left(\frac{\pi}{4} + \pi\varepsilon\right) - \cos^2\left(\frac{\pi}{4} - \pi\varepsilon\right)\\ &\approx \left(\frac{1}{\sqrt{2}} - \frac{\pi\varepsilon}{\sqrt{2}}\right)^2 - \left(\frac{1}{\sqrt{2}} + \frac{\pi\varepsilon}{\sqrt{2}}\right)^2\\ &\approx -\pi\varepsilon - \pi\varepsilon = -2\pi\varepsilon. \qquad (3.1)\end{aligned}$$

The squaring operation translates the signal component to baseband. In the case of a detector enhanced with high-pass filters placed before the squaring operation, the latency introduced by the high-pass filter can be modeled as latency occurring after the squaring. The latency of a single-pole high-pass filter can be modeled with a single-pole low-pass filter placed after the squarer. As illustrated in Figure 3.7, the pole of the low-pass filter in the model is placed at $z = a$ if the pole of the high-pass filter in the enhanced detector is at $z = -a$.

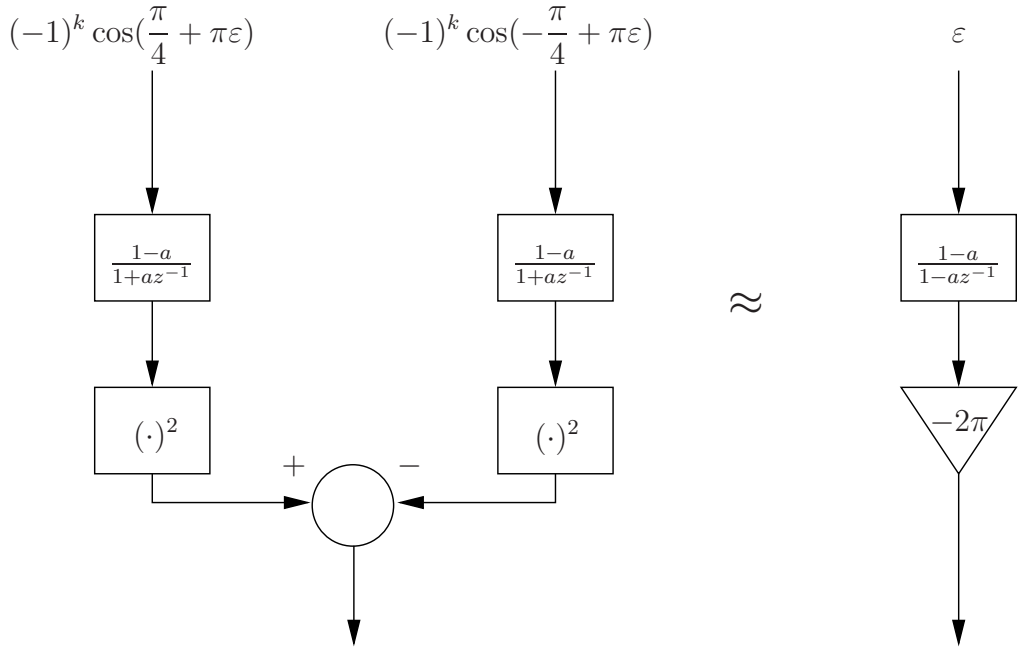

Figure 3.7 Modeling the effect of the high-pass filters in the case of a sinusoidal input signal, $\varepsilon \ll 1$

For the sinusoidal input signal considered here, the insertion of high-pass filters in the detector does not cause any loss of timing information. The reason is that the early and late signals are tones with a frequency of π radians/symbol (see (3.1)), and the high-pass filter gain at $\omega = \pi$ is equal to 1. Therefore the gain following the low-pass filter in the model is simply -2π.

The input signal of interest in this thesis has random symbols. It is shown below that the high-pass filters are modeled as in the case of an input sinusoidal signal, except that the gain following the low-pass filter changes from -2π to G', where G' is the slope of the altered S-curve at $\varepsilon = 0$. Recall from Chapter 2 that the approximation to the ideal high-pass filter with a single-pole high-pass filter has the consequence of removing some of the timing information. This loss in timing information translates into a decrease in the slope of the detector's S-curve at $\varepsilon = 0$.

The input signal can be decomposed into a sinusoid, $\frac{-G'}{2\pi}\cos(\frac{\pi}{4}n + \pi\varepsilon)$, and a signal, referred to as the noisy signal that is equal to the input signal minus that

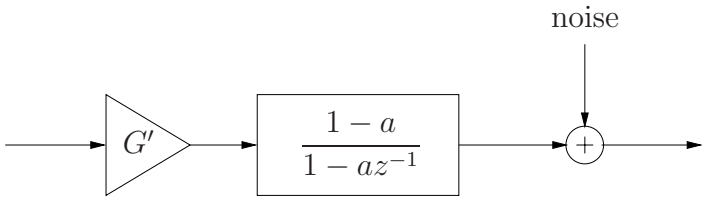

Figure 3.8 Linear model for the enhanced early-late detector.

sinusoid. For small timing offset (i.e., $\varepsilon \ll 1$), the detector is approximately linear, and the principle of superposition applies. The output due to the input sinusoid, $\frac{-G'}{2\pi}\cos(\frac{\pi}{4}n + \pi\varepsilon)$, is modeled as before except that the gain is G' instead of -2π. This is the signal component that is equal to the output of the S-curve evaluated at ε. The signal referred to as the noisy signal only produces a zero-mean noise at the output, and is modeled as additive noise.

The linear model for the enhanced detector is shown in Figure 3.8. The validity of the models for both the conventional and enhanced detectors has been verified in closed-loop operation, the results of which are presented in Section 3.5.

3.3.2 Gardner detectors

The general model for non-data-aided feedback synchronizers [55] is also used to model the Gardner detector. The Gardner detector's S-curve is similar to that of the early-late detector. It has a sinusoidal shape, is odd and nearly linear about $\varepsilon = 0$ [16]. This model is given in Figure 3.9, where the gain, G_g, is the slope of the Gardner detector's S-curve evaluated at $\varepsilon = 0$. This slope, which is a function of the roll off factor and the variance of the symbols, was evaluated with a computer simulation.

The model for the enhanced Gardner detector is similar to the model for the enhanced early-late detector. The gain is denoted by G'_g, where G'_g is the slope of the altered S-curve of the Gardner detector. This slope was evaluated with a computer simulation. The model for the enhanced Gardner detector is given in Figure 3.10.

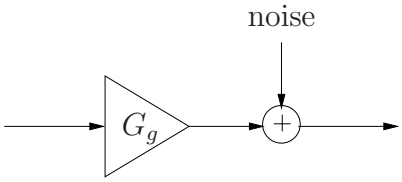

Figure 3.9 Linear model for the Gardner detector.

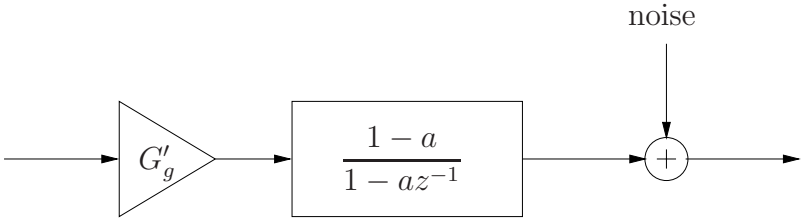

Figure 3.10 Linear model for the enhanced Gardner detector.

Note that the presence of a single-pole filter in the model of the enhanced detector increases the loop order by 1. The order of the loop also increases if a single-pole low-pass filter is placed at the output of the detector.

3.4 Linear analyses of the loops used in these systems

3.4.1 Closed-loop bandwidth of interest

Performance comparisons among the different systems were accurately obtained by simulating the systems with identical closed-loop bandwidths.

There are several ways to define the closed-loop bandwidth. Here the definition chosen is the one that corresponds to the noise bandwidth. The noise bandwidth, B_L, is defined as [59]

$$B_L = \frac{1}{2}\frac{1}{2\pi}\int_{-\pi}^{+\pi} |H(e^{j\omega})|^2 d\omega, \tag{3.2}$$

where $H(z)\big|_{z\,=\,e^{j\omega}}$ is the closed loop frequency response.

The transfer function, $H(z)$, is calculated below for first, second, and third-order loops. Calculation of $H(z)$ requires linearizing the loop by using the models that were

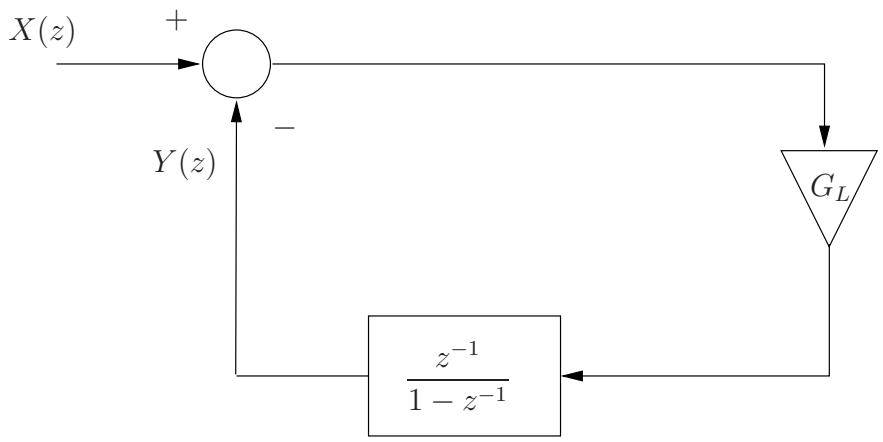

Figure 3.11 Model for first-order loop.

derived in Section 3.3 for the early-late and Gardner detectors, and the loop model given in Section 3.2.

3.4.2 Linear analysis of the first-order loop

A model for the first-order loop is shown in Figure 3.11, where the loop gain, G_L, is equal to $G \times K$ if the TED is the early-late detector and $G_g \times K$ if the TED is the Gardner detector.

The open-loop transfer function is then $\dfrac{G_L z^{-1}}{1 - z^{-1}}$, and the closed-loop transfer function is given by

$$H_1(z) = \frac{G_L z^{-1}}{1 - (1 - G_L) z^{-1}}. \tag{3.3}$$

The root-locus plot [60] for the closed-loop system, $H_1(z)$, is shown in Figure 3.12. The unit circle is shown with a dotted line. There is only one root-locus path, and this path is shown with a thick line. The open-loop system has one pole at $z = 1$ and a zero at $-\infty$. For loop gains less than 2 the system is perfectly stable.

If $h_1[k]$ is the inverse Z-transform of $H_1(z)$, then from (3.2) and Parseval's theo-

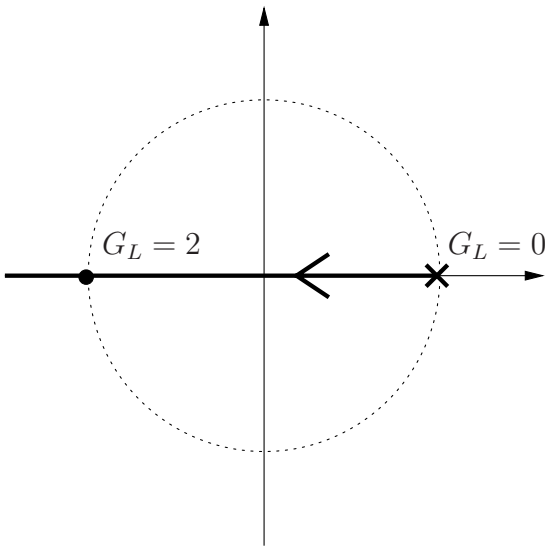

Figure 3.12 Root-locus plot for first-order loop system.

rem [56], the noise bandwidth, B_L, is given by

$$B_L = \frac{1}{2} \sum_{k=-\infty}^{+\infty} h_1^2[k]. \tag{3.4}$$

Equation (3.4) is solved to yield a simple expression that relates B_L to the loop gain, G_L. From (3.3) using the z-transform pair, $A^k u[k] \longleftrightarrow \frac{z}{z-A}$, it can be shown that $h_1^2[k] = (\frac{G_L}{1-G_L})^2(1-G_L)^{2k}u[k-1]$, where $u[k]$ is the unit step function. For $0 < G_L < 2$, the geometric series, $\sum_{k=-\infty}^{+\infty} h_1^2[k]$, converges and

$$B_L = \frac{1}{2}\left(\frac{G_L}{2-G_L}\right) \approx \frac{G_L}{4} \text{ for } |\mathrm{G_L}| \ll 2. \tag{3.5}$$

3.4.3 Linear analysis of the second-order loop

A model for the second-order loop is shown in Figure 3.13, where the loop gain, G_L, can take on values, $G \times K$, $G_g \times K$, $G' \times K$, or $G'_g \times K$, depending on whether the TED is the early-late detector, the Gardner detector, the enhanced early-late detector, or the enhanced Gardner detector. The low-pass filter models either the

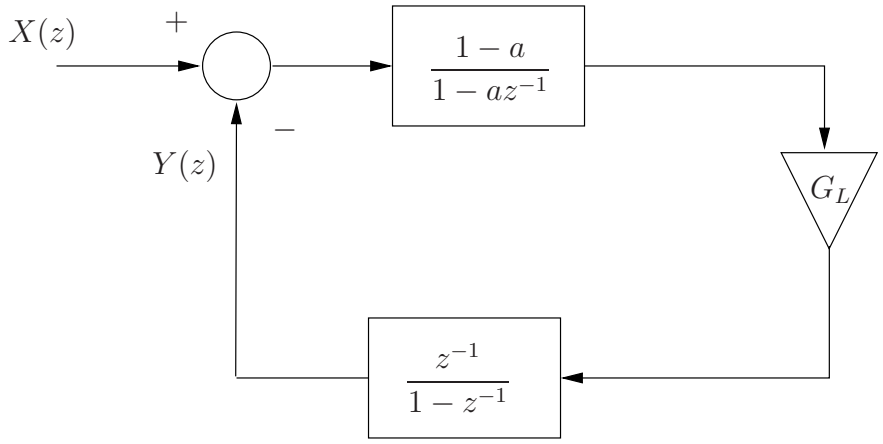

Figure 3.13 Model for second-order loop.

high-pass filters in the enhanced detector (in which case no low-pass filter is placed at its output) or the single-pole low-pass filter placed at the output of the detector (in which case the conventional detector is used).

The open-loop transfer function is $\frac{G_L(1-a)z^{-1}}{(1-z^{-1})(1-az^{-1})}$, and the closed-loop transfer function is

$$H_2(z) = \frac{G_L(1-a)z^{-1}}{1-(a+1-G_L(1-a))z^{-1}+az^{-2}}. \tag{3.6}$$

The root-locus plot for $H_2(z)$ is shown in Figure 3.14. The poles of the open-loop transfer function are shown with a "x" and the zeros are shown with a circle. There is a zero at infinity, which is not shown in the Figure. As the loop gain increases, the poles move toward each other along the real axis. They meet at $z = \sqrt{a}$. As the gain increases further, the poles become complex conjugate pairs with one pole traveling on the upper half-circle and the other pole traveling on the lower half-circle. They meet again on the real axis at $z = -\sqrt{a}$. As the gain continues to increase, the poles move in separate directions with one traveling toward the origin and the other traveling toward minus infinity.

The systems that were simulated were critically damped systems. The system becomes critically damped when the two poles are at the breakaway point, which is

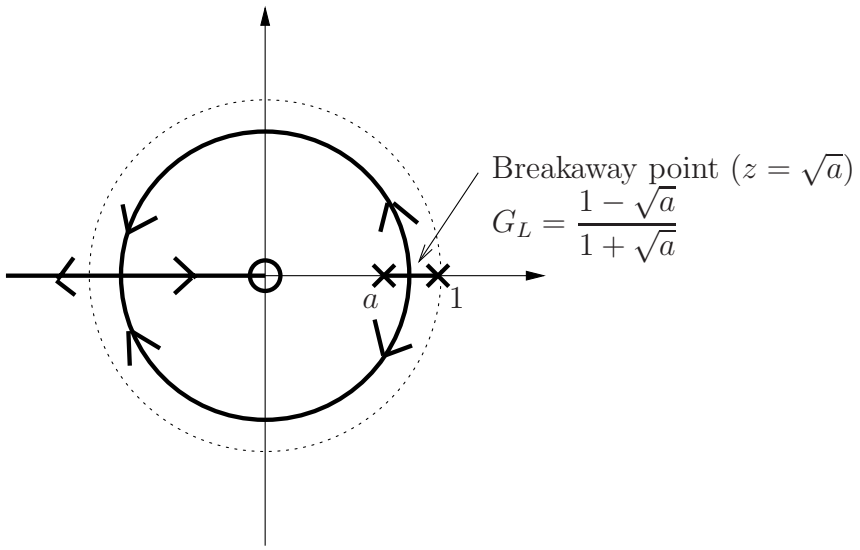

Figure 3.14 Root-locus plot for second-order loop system.

$z = \sqrt{a}$. The value of the loop gain, G_L, is the one that makes the discriminant of the second-order equation equal to zero, i.e., $1 - (a + 1 - G_L(1 - a))z^{-1} + az^{-2} = 0$. This yields

$$G_L = \frac{1 - \sqrt{a}}{1 + \sqrt{a}}. \tag{3.7}$$

For a critically-damped system, using (3.7), $H_2(z)$ reduces to

$$H_2(z) = \frac{(1 - \sqrt{a})^2 z}{(z - \sqrt{a})^2}. \tag{3.8}$$

An expression for the noise bandwidth, B_L, as a function of the loop gain, G_L, is determined as follows. From (3.8), and using the z-transform pair, $kA^k u[k] \longleftrightarrow \frac{Az}{(z-A)^2}$, it is found that

$$h_2[k] = \frac{(1 - \sqrt{a})^2}{\sqrt{a}} k(\sqrt{a})^k u[k], \tag{3.9}$$

and

$$h_2^2[k] = \frac{(1 - \sqrt{a})^4}{a} k^2 a^k u[k]. \tag{3.10}$$

Using the geometric series, $\sum_{k=1}^{\infty} k^2 A^k = \frac{A(A+1)}{(1-A)^3} (|A| < 1)$, and substituting (3.10) into (3.4) after replacing $h_1[k]$ by $h_2[k]$, the noise bandwidth, B_L, is given by

$$\begin{aligned} B_L &= \frac{(1-\sqrt{a})^4(a+1)}{2(1-a)^3} \\ &= \frac{(1-\sqrt{a})(a+1)}{2(1+\sqrt{a})(1+\sqrt{a})^2} \\ &= \frac{G_L}{2}\left(1 - \frac{2\sqrt{a}}{(1+\sqrt{a})^2}\right), \end{aligned} \tag{3.11}$$

where (3.7) was used in the last substitution.

For small loop gains (i.e., $|G_L| \ll 1$), $\sqrt{a} \approx 1$, $\frac{2\sqrt{a}}{(1+\sqrt{a})^2} \approx \frac{1}{2}$, and

$$B_L \approx \frac{G_L}{4}. \tag{3.12}$$

3.4.4 Linear analysis of the third-order loop

A third-order loop has three poles. The simulated systems that contained a third-order loop had an enhanced detector and a single-pole low-pass filter at the output of the detector.

The analysis of the third-order loop is more complex than the analysis of the second-order loop due to the presence of an extra pole. The linear analysis of the loop is performed by considering two distinct cases:

Case A: The pole of the high-pass filters inside the detector is placed at the same distance from the unit circle as the pole of the low-pass filter at the output of the detector.

Case B: The pole of the high-pass filters is placed closer to or further away from the unit circle than the pole of the low-pass filter.

A detailed analysis for case A is presented below. The results obtained are easily

extended to case B.

- Case A analysis:

  The poles are at distance, a, from the origin, with the pole of the low-pass filter placed at $z = a$, and the pole of the high-pass filter placed at $z = -a$. The linear model of the loop is shown in Figure 3.15, where the loop gain, G_L, can take on values, $G' \times K$, or $G'_g \times K$.

  The open-loop transfer function is $\dfrac{G_L(1-a)^2 z^{-1}}{(1-z^{-1})(1-az^{-1})^2}$, and the closed-loop transfer function is

$$H_3(z) = \frac{G_L(1-a)^2 z^2}{(z-1)(z-a)^2 + G_L(1-a)^2 z^2}. \tag{3.13}$$

  The root-locus plot for $H_3(z)$ is shown in Figure 3.16. The double-pole at $z = a$ of the open-loop transfer function is shown with two 'x's and the double-zero at the origin with two circles. There is also a pole at $z = 1$ and a zero at infinity. As the loop gain increases, one of the poles at $z = a$ and the pole at $z = 1$ move toward each other, while the second pole at $z = a$ moves toward the origin, where its locus path ends. As in the case of the second-order loop, after merging at the breakaway point, the two poles become complex conjugate, and travel on upper and lower half-circles. After joining again on the real axis, the poles separate. One locus path ends at the origin whereas the other path ends at infinity.

  For a critically-damped system, all three poles of $H_3(z)$ are on the positive real axis with two poles at the breakaway point. For smaller order loops, simple equations were derived to relate B_L, G_L, and a (see (3.11)). Here, no simple equation could be found, so an iterative algorithm was devised to find numerical solutions for G_L and a, given a desired value, B_L^d, of the noise bandwidth.

  A high-level data-flow diagram of the algorithm is given in Figure 3.17. The algorithm is based on a dichotomic search to find a value for a that yields a bandwidth B_L that is within 1 % of B_L^d.

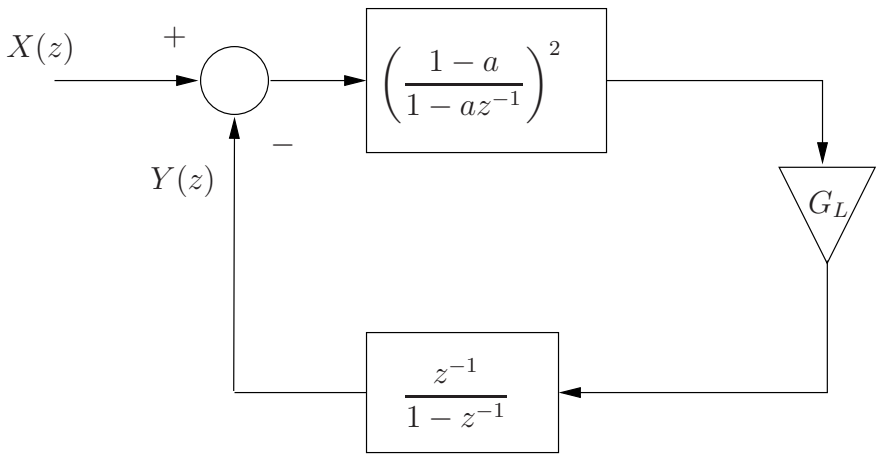

Figure 3.15 Model for third-order loop - case A.

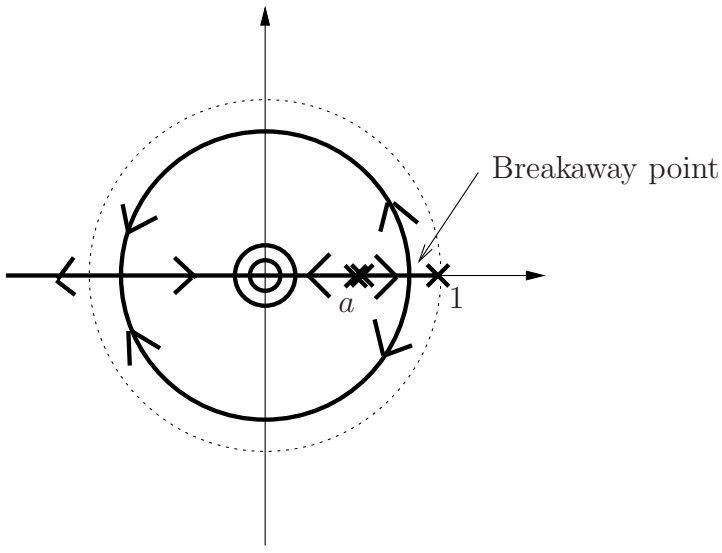

Figure 3.16 Root-locus plot for third-order loop - case A.

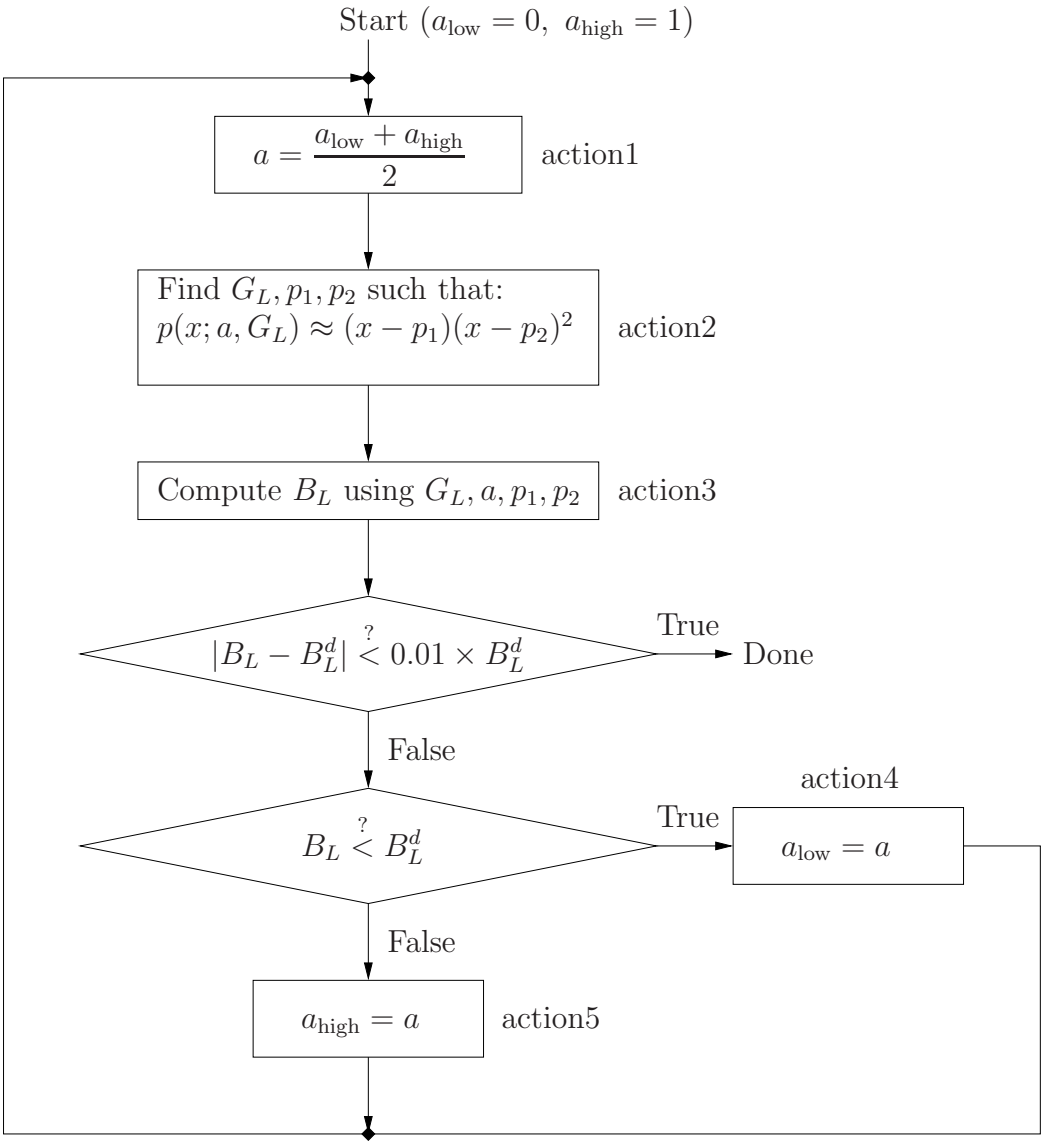

Figure 3.17 High-level data-flow diagram for algorithm.

The algorithm consists of several actions:

Action1: a is set to the mid-point value of $(a_{\text{low}}, a_{\text{high}})$. At the start, $a_{\text{low}} = 0, a_{\text{high}} = 1$, and a is set to 0.5.

Action2: For a critically damped system, the roots of $H_3(z)$ are real. From (3.13), they are the roots of the third order polynomial given by

$$p(x; a, G_L) = x^3 + (-2a - 1 + G_L(1-a)^2)x^2 + (a^2 + 2a)x - a^2. \quad (3.14)$$

Action2 consists of finding numerical solutions for G_L and the polynomial roots, given a and the condition that $p(x; a, G_L)$ can be written in the form $(x - p_2)^2(x - p_1)$ (e.g. $p(x; a, G_L) \approx (x - p_2)^2(x - p_1)$), where p_2 is the double-root at the breakaway point, and p_1 the single root.

Action3: Compute B_L using G_L, a, p_1, and p_2.

Following Action3, two tests occur, the outcomes of which are:

Done: B_L is within 1 % of B_L^d. The algorithm ends.

$\mathbf{|B_L - B_L^d| > 0.01 \times B_L^d}$ **and** $\mathbf{B_L < B_L^d}$**:** An additional iteration is required with a larger value for a. a_{low} is set to a (action4).

$\mathbf{|B_L - B_L^d| > 0.01 \times B_L^d}$ **and** $\mathbf{B_L < B_L^d}$**:** An additional iteration is required with a smaller value for a. a_{high} is set to a (action5).

Action2 and Action3 are now described in more details.

- **Action2 description:**

  Solutions for G_L, p_1, and p_2 are found with an iterative search. To facilitate the search, an upper bound for G_L is analytically derived, as follows.

  Figure 3.18 shows realizations of $p(x; a, G_L)$ for different values of G_L and for $a = 0.3$. The curves displayed correspond to values of G_L equal to 0.15, 0.207, 0.329, and 0.5. Notice that for $G_L > 0.208$, the curves have only one zero-crossing. In terms of the root-locus plot, two out of the three

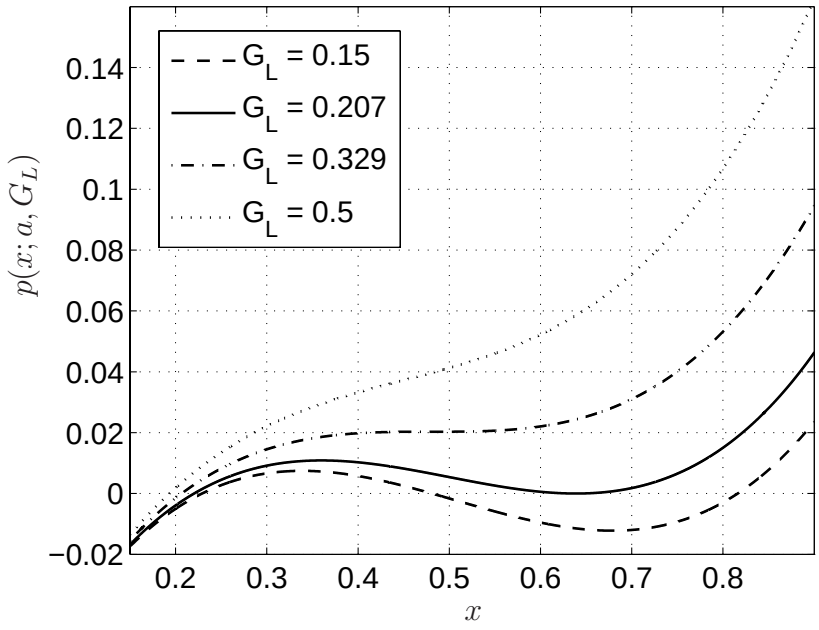

Figure 3.18 Realizations of $p(x; a, G_L)$ for $a = 0.3$ and different values of G_L. Only the portion of the curves between $x = 0.2$ and $x = 0.9$ is shown.

poles are complex conjugate. $G_L \approx 0.207$ is the value of interest since $p(x; a, G_L)$ has a double root ($p_2 \approx 0.64$), and a single root ($p_1 \approx 0.21$). For smaller values of G_L, $p(x; aG_L)$ has three distinct roots.

Observe that for values of G_L that are less than the value of interest, the curves have two distinct points with zero slope. This situation remains true until $G_L \approx 0.329$ (G_L greater than the value of interest), where the curve has only one point with zero-slope, before changing into a strictly increasing function for larger values of G_L. Thus, an upper bound, $G_L^{\max}$, for G_L is obtained when the slope of $p(x; aG_L)$ is zero at only one point. Mathematically, $\dfrac{dp(x)}{dx} = 0$ has a double root. Setting the discriminant to zero, after some algebraic manipulations, it is found that $G_L^{\max}$ is equal to

$$G_L^{\max} = \frac{1 + 2a - \sqrt{3(a(2+a))}}{(a-1)^2}. \tag{3.15}$$

Clearly from Figure 3.18, the value, G_L, of interest verifies two conditions:

$$\begin{cases} p(p_2; a, G_L) & = 0, \\ \dfrac{dp(x; a, G_L)}{dx}|_{x=p_2} & = 0. \end{cases} \tag{3.16}$$

As done previously for a, G_L is sought with a dichotomic search, where the initial interval is $(0, G_L^{\max})$, and the starting value is $0.5G_L^{\max}$.

For a given G_L, an iteration consists of computing the value of p_2 such that $\dfrac{dp(x; a, G_L)}{dx}|_{x=p_2} = 0$. This is easily done since $\dfrac{dp(x; a, G_L)}{dx}$ is a second-order polynomial. A test occurs to determine whether $|p(p_2; a, G_L)| < 10^{-4}$, in which case the search ends. If the test fails, then another iteration is needed. The range of the new interval for G_L is determined by the sign of p_2.

– **Action3 description:**

An expression for B_L in terms of G_L, a, p_1, and p_2 is obtained by writing $H_3(z)$ in the form

$$H_3(z) = \frac{G_L(1-a)^2}{(z-p_2)^2(z-p_1)}. \tag{3.17}$$

After computing the inverse Z-transform of $H_3(z)$, (3.4) is used to yield an equation for B_L. The details of the calculations are given in Appendix E, where it is found that

$$\begin{aligned} B_L = \frac{1}{2}\frac{G_L^2(1-a)^4}{(p_2-p_1)^2}\Bigg[& \frac{p_1^2}{(p_1-p_2)^2}\left(\frac{p_2^2}{1-p_2^2} + \frac{p_1^2}{1-p_1^2} - 2\frac{p_1p_2}{1-p_1p_2}\right) \\ & + \frac{2p_1}{p_1-p_2}\left(\frac{p_2^2}{(1-p_2^2)^2} - \frac{p_1p_2}{(1-p_1p_2)^2}\right) \\ & + \frac{p_2^2(1+p_2^2)}{(1-p_2^2)^3}\Bigg]. \end{aligned} \tag{3.18}$$

This completes the description of the algorithm.

- Case B analysis:

The loop's model and the root-locus plot are shown in Figures 3.19 and 3.20

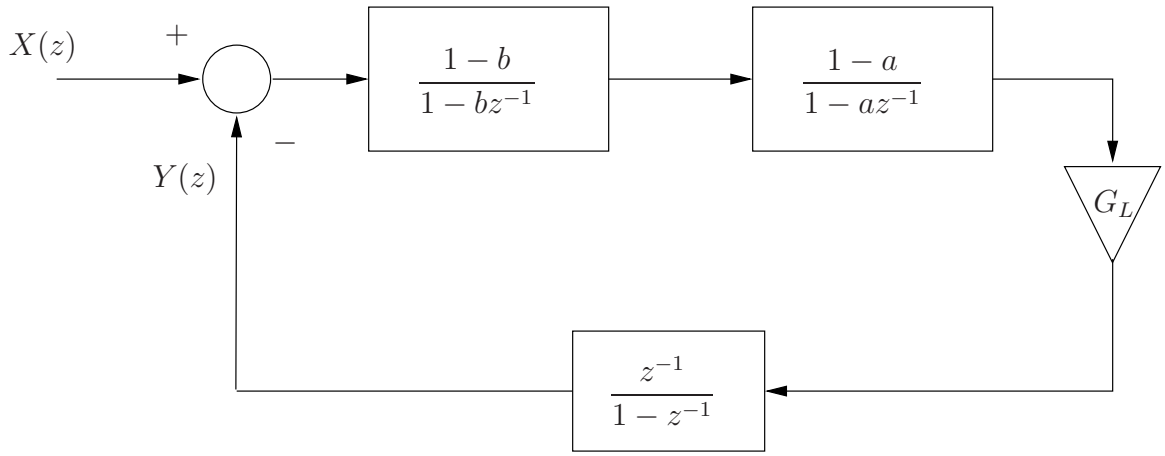

Figure 3.19 Model for third-order loop - case B.

respectively. The main difference from case A is that in case B the poles of the open-loop system are distinct. In Figure 3.20, a first pole is shown at $z = a$, a second pole at $z = b$, and a third pole at $z = 1$. Note that there are two systems with the same model. One system has the pole of the low-pass filter at $z = a$, and the pole of the high-pass filters at $z = -b$. The other system poles of the low-pass and high-pass filters are respectively at $z = b$ and $z = -a$.

The algorithm devised in case A can be used in case B provided that the following modifications are made:

1. b is fixed, and is passed to the algorithm along with B_L^d.
2. No changes to action1.
3. The third-order polynomial becomes

$$p(x; a, b, G_L) = x^3 + (-a - b - 1 + G_L(1-a)(1-b))x^2 + (a + b + ab)x - ab, \tag{3.19}$$

and the upper bound for G_L is given by

$$G_L^{\max} = \frac{1 + a + b - \sqrt{3(a + b + ab)}}{(a-1)(b-1)}. \tag{3.20}$$

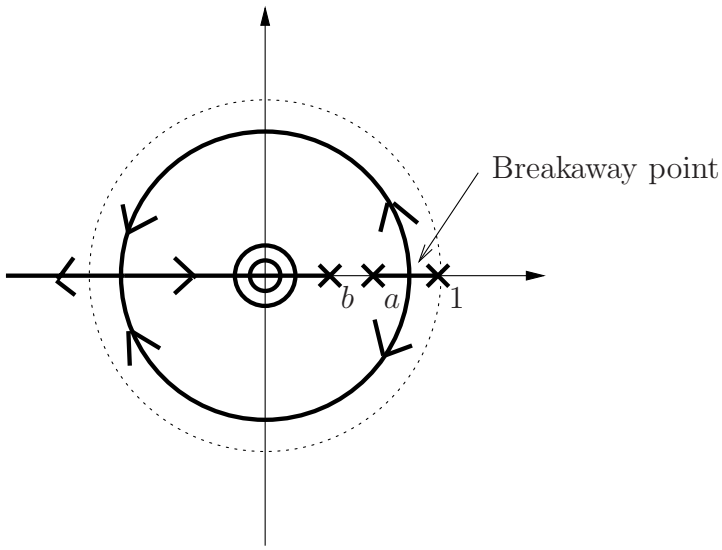

Figure 3.20 Root-locus plot for third-order loop - case B.

4. In (3.18), the term, $(1-a)^4$, is replaced with $(1-a)^2(1-b)^2$ to obtain the new equation for B_L.

The algorithm was used to compute the positions of the poles for different bandwidths, B_L. The results are shown in Figure 3.21, where the bandwidths are expressed in percentage of the symbol rate. Each curve shows a as a function of b for a given B_L. The plot shows that minimizing the response time (e.g. having the breakaway point as close as possible to the origin) and maximizing noise reduction (e.g. having the poles of both the low-pass filter and high-pass filters as close to the unit circle as possible) occurs for $a = b$ (i.e., case A).

3.5 Verification

The validity of the feedback loops models was verified by comparing for each model the theoretical closed-loop amplitude response with measurements of this response obtained through simulations. The feedback loop was implemented in Simulink. The TED was the early-late detector. The resampler used an interpolation filter of length 30 samples, which was a truncated version of the impulse response, $\frac{\sin \pi t/T}{\pi t/T}$ [61].

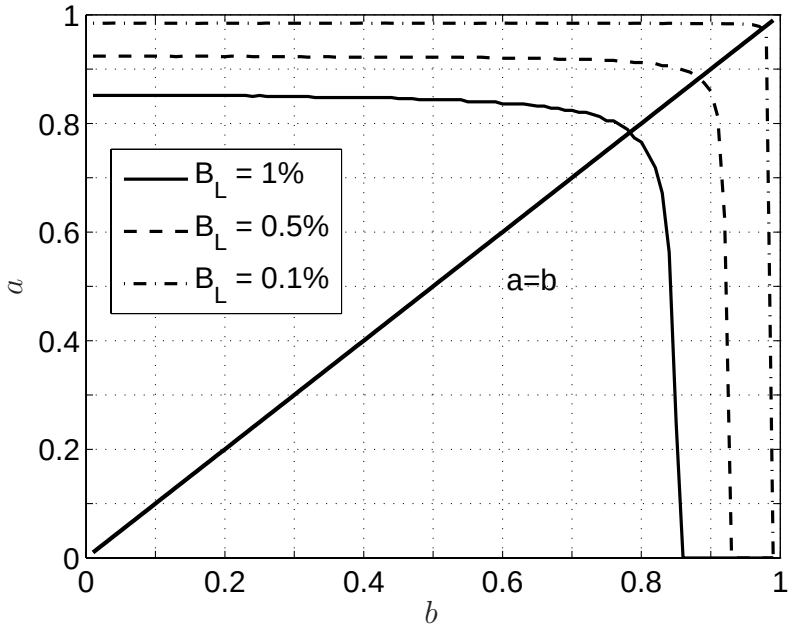

Figure 3.21 Position of the poles for different bandwidths, B_L.

Two types of measurement were made. One set of measurement was obtained with an input signal that does not produce self-noise in the early-late detector. Such signal is a sinusoid at frequency $\pi/4$ radians/sample. This signal was produced by using the alternating symbol pattern, $-7, 7, -7, 7, \ldots$. The signal had 4 samples per symbol interval, and the roll off factor was set to $r = 0.1$. Measurements were also performed by feeding an 8-PAM signal with random symbols (4 samples per symbol interval and $r = 0.1$). This signal produced self-noise in the early-late detector.

The closed-loop amplitude response was measured at several frequencies. The timing offset was varied between $-1/16$ and $1/16$ in a sinusoidal fashion at the frequency of interest. This was realized by using a second interpolator that was identical to the one in the loop, and that was placed in line with the input.

First, second and third-order loops were simulated in the case of no self-noise. The (noise) bandwidth, B_L, was set to 0.5 % of the symbol rate.

A first-order loop was simulated with the conventional early-late detector and

no loop filter. From (3.5) the loop gain was equal to $G_L = 0.02$ radians/symbol-interval. In the case of an alternating symbol pattern, here $7, -7, 7, -7, \ldots$, the S-curve equation of the detector is $-7^2 \sin 2\pi\varepsilon$ (Section 2.2) so the slope of the S-curve at $\varepsilon = 0$ was -98π.

A second-order loop was simulated with the enhanced early-late detector. In the case of an enhanced detector, there is no low-pass filter in the loop for a second-order system. The pole of the high-pass filters was placed at $z = -a$. From (3.7) the loop gain was $G_L = 0.02$ radians/symbol-interval, and a was equal to $\left(\frac{1 - G_L}{1 + G_L}\right)^2 = 0.9321$. Note that the S-curve is not altered in that case, since the early and late signals are sinusoidal signals at frequency π radians / symbol-interval, and the gain of the high-pass filter is unity at that frequency.

A third-order loop was simulated with the enhanced early-late detector and with a single-pole low-pass filter in the loop. The pole of the high-pass filter was at $z = -a$, and the pole of the low-pass filter was at $z = a$. The parameters of the loop were determined as follows. Using the algorithm defined in Figure 3.17 on page 77, with $B_L = 0.005$, numerical solutions for G_L and a were found to be $G_L = 0.0185$ and $a = 0.8848$.

Each measurement consisted of recording 1256 samples of the timing error of the resampled signal after the loop had reached steady state. Such signal was a sinusoid at a frequency equal to the frequency used to vary the timing offset but with a smaller amplitude due to the filtering effect of the loop. The frequencies chosen for the measurements were all multiples of 1/1256 cycles/sample. The amplitude of the sinusoid was estimated by computing the Fourier coefficient of the recorded signal at the measurement frequency to determine the amplitude response of the loop at that frequency. Plots of the closed-loop amplitude responses for the first, second, and third-order loops are shown in Figure 3.22. These plots were obtained by using (3.3), (3.8), and (3.13). The simulation results are marked with a 'x' for the first-order loop, a 'o' for the second-order loop and a square for the third-order loop.

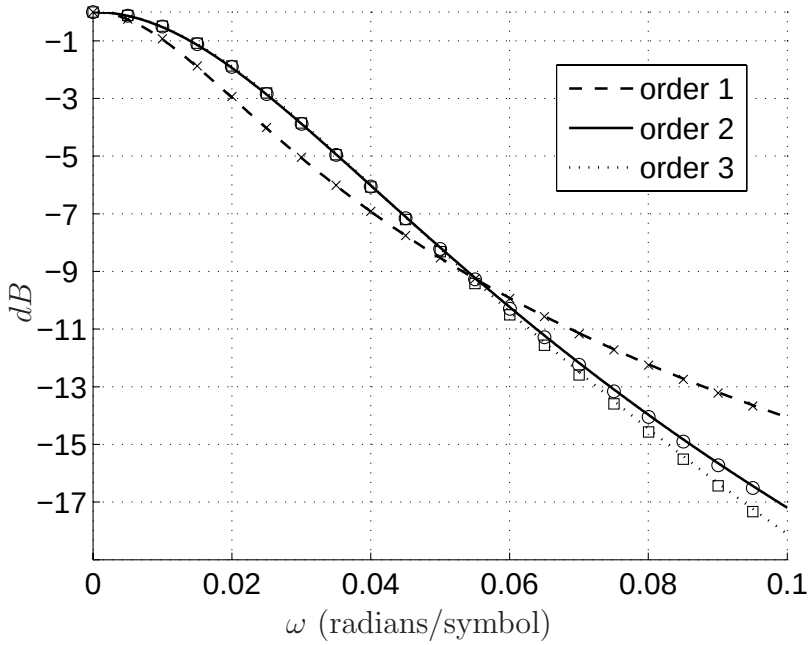

Figure 3.22 First, second, and third-order closed-loop amplitude responses with three sets of simulation results marked with 'x', 'o', and squares in the case of no self-noise, and B_L equal to 0.5 % of the symbol rate.

The close agreement between the simulation results and the theoretical curves confirm the validity of the linear models in the case of no self-noise. Notice that the 3 dB bandwidth of the first-order loop is smaller than the 3 dB bandwidth of the second and third-order loops. This confirms that the 3 dB bandwidth parameter criterion to establish comparison between the systems would not have been a good choice since this parameter does not take into account of the roll off sharpness of the frequency responses.

A third-order loop was simulated in presence of self-noise. The bandwidth, B_L, was set to 0.1 % of the symbol rate. A narrower bandwidth was used to restrict the self-noise to occur within the linear region of the detector, i.e., to remain within 10% of the symbol interval. This bandwidth was chosen after visually inspecting timing error plots, which were obtained by simulating the third-order loop with different bandwidths.

The third-order loop was simulated with the enhanced early-late detector and with a single-pole low-pass filter in the loop. The pole of the high-pass filter was at $z = -a$, and the pole of the low-pass filter was at $z = a$. The parameters of the loop were determined as follows. Using the algorithm defined in Figure 3.17 on page 77, with $B_L = 0.001$, numerical solutions for G_L and a were found to be $G_L = 0.0036$ and $a = 0.9761$.

Each measurement consisted of recording 12×1256 samples of the timing error of the resampled signal after the loop had reached steady state. An averaged periodogram [62] was used to estimate the amplitude of the sinusoid corrupted with self-noise.

A plot of the third-order closed-loop amplitude response along with the simulation results marked with a square are shown in Figure 3.23.

The close agreement between the simulation results and the theoretical curves confirm the validity of the linear models in the case of no self-noise, and that the linear analyses were done without error.

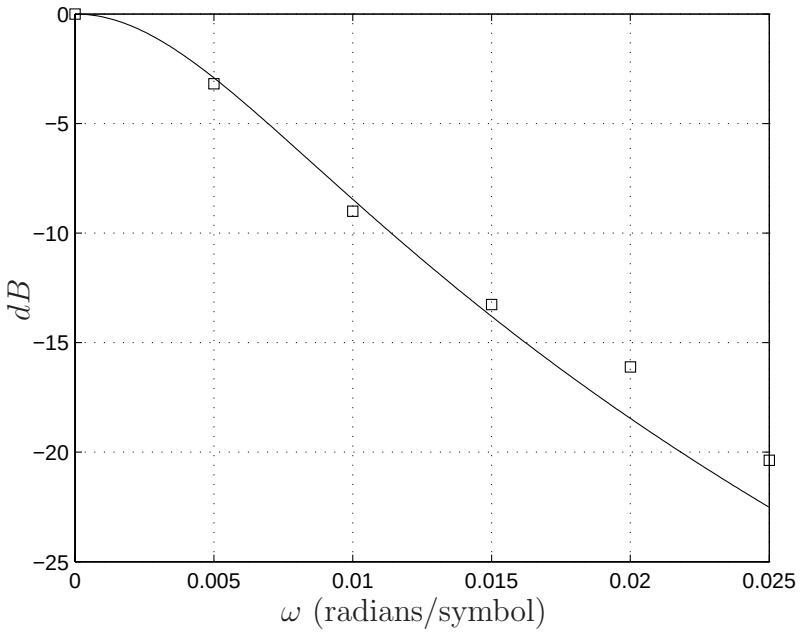

Figure 3.23 Third-order closed-loop amplitude response with one set of simulation results marked with squares in the case of self-noise and $B_L = 0.1$ % of the symbol rate.

3.6 Performance of the systems

3.6.1 Description of the systems under evaluation

Systems containing either the early-late or Gardner detectors in their conventional and enhanced forms were simulated. The Franks/Gardner synchronizer was simulated as well as the Franks/early-late synchronizer. The simulated systems are described below.

Conventional and enhanced early-late detectors

The conventional detector was simulated in both first-order and second-order loops. The second-order system had a single-pole low-pass filter placed after the output of the detector.

The enhanced early-late detector was simulated with and without a low-pass filter placed after the detector's output. Since the enhanced detector has a high-pass filter that appears to be a low-pass filter, the response corresponds to that of a second-order loop if there is no low-pass filter placed at its output, and a third-order loop if there is a low-pass filter placed at its output.

Conventional and enhanced Gardner detectors

The Gardner detector was simulated in first-order and second-order loop systems as in the case of the conventional early-late detector.

The enhanced Gardner detector was simulated in second-order and third-order loop systems as in the case of the enhanced early-late detector.

Franks/Gardner synchronizer

The prefilter used in the simulation was a 161 tap FIR filter, which was obtained with a least mean square fit to the frequency response given in (1.3) on page 27.

The Franks/Gardner synchronizer was simulated in a first-order loop and in a

second-order loop using either none or one single-pole low-pass filter at the output of the detector.

Franks/early-late synchronizer

The Franks/early-late synchronizer is identical to the the Franks/Gardner synchronizer except that the Gardner detector is replaced with the early-late detector.

The Franks/early-late synchronizer was simulated in a first-order loop and in a second-order loop as in the case of the Franks/Gardner synchronizer.

3.6.2 Simulation results

The systems previously described were implemented in Simulink. The resampler used an interpolation filter, as described in Section 3.5. The input signal was a 64-QAM signal of length $16,000$ symbols, which was generated with 4 samples per symbol and a roll off factor of 0.1. The 64-QAM signal was corrupted with additive white Gaussian noise, the level of which was determined by the operating $\frac{E_b}{N_0}$. The ratio, $\frac{E_b}{N_0}$, was varied in 1 dB step from 13 to 23 dB. The QAM signal was generated with no timing offset. A step function timing offset of 0.25T was introduced at the time of the 1000^{th} symbol to strain the detector. The timing error of the resampled signal was recorded at the symbol rate after the loop reached steady state.

Curves of tracking mode timing jitter variances versus E_b/N_0 are shown in Figure 3.24 for a bandwidth, B_L, of 0.1 % of the symbol rate. Six curves are plotted: three are associated with the early-late detector, and three are associated with the Gardner detector. The three curves associated with the early-late detector have data points shown with a square. The three curves associated with the Gardner detector have data points shown with a diamond.

The three curves for the early-late detector illustrate its performance in three different systems. The dotted line marked with squares, which is the top curve in the graph, is the performance of the conventional early-late detector. In this system,

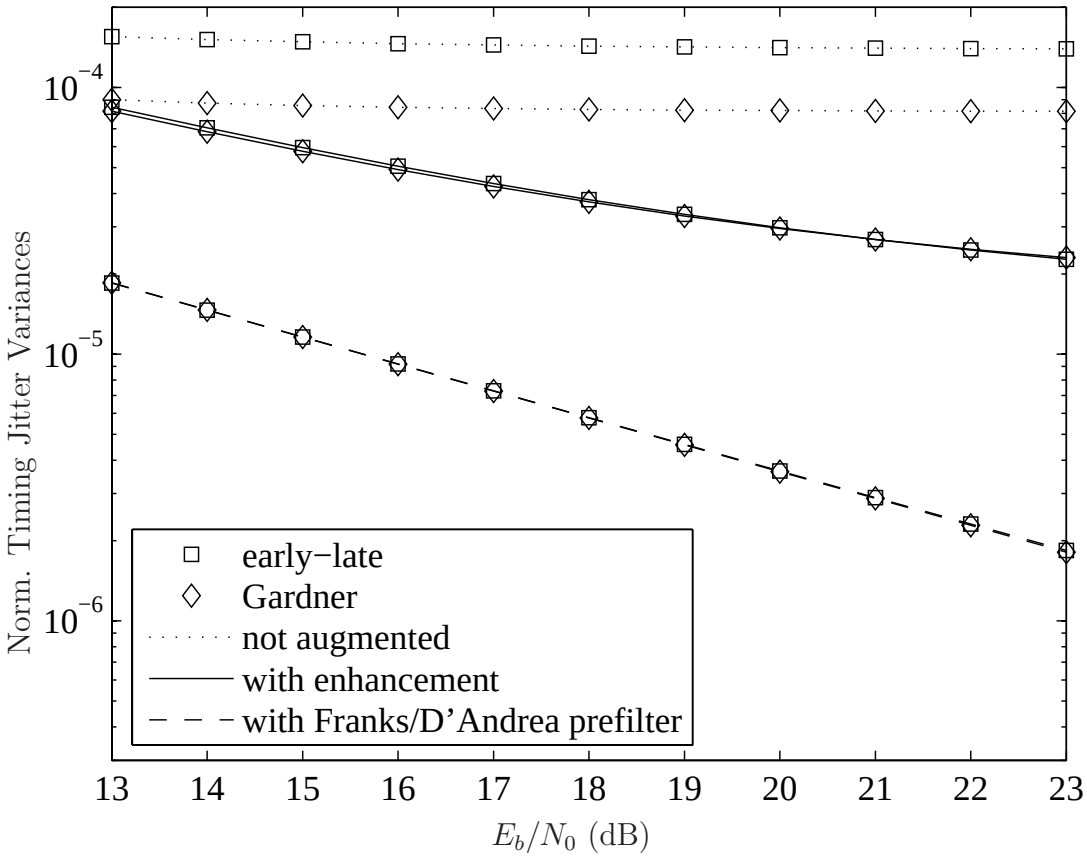

Figure 3.24 Normalized timing jitter ($T = 1$) variances for critically damped systems with a bandwidth equal to $B_L = 0.1$ % of the symbol rate.

the loop was of order 1 with $G_L = 0.004$. The solid line marked with squares shows the performance of the enhanced early-late detector. The loop was of order 2 with same loop gain, $G_L = 0.004$. The pole of the high-pass filter was at $z = -0.9841$. The dashed line marked with squares shows the performance of the Franks/early-late synchronizer. The prefilter was placed in front of the resampler of the loop. The loop was of order 1 with $G_L = 0.004$.

The three curves for the Gardner detector illustrate its performance in the three scenarios. The dotted line marked with diamonds shows the performance of the conventional Gardner detector. The solid line marked with diamonds shows the performance of the enhanced Gardner detector. The high-pass filter was the same as the

one used to enhance the early-late detector. The dashed line marked with diamonds show the performance of the Franks/Gardner synchronizer.

From these curves it can be seen that the Gardner detector outperforms the conventional early-late detector. The self-noise is the dominant noise in both the early-late and the Gardner detector since the variance of the jitter does not decrease as E_b/N_0 is increased in either case. When the two detectors are enhanced, the performance of both improves. The timing jitter variance of the enhanced early-late detector is nearly 8 dB lower than the timing jitter variance of the conventional early-late detector for $E_b/N_0 = 23$ dB. The Gardner detector looses its advantage over the early-late detector since the performance of both detectors is nearly identical after enhancement. The Franks/Gardner and Franks/early-late synchronizers perform very well with nearly identical timing jitter variances. These synchronizers offer the best performance. However, the performance improvement comes at a cost of a long FIR prefilter for each of the in phase and quadrature signal streams, and two additional resamplers.

A small bandwidth (e.g. 0.1 % of the symbol rate) is an effective solution to mitigate self-noise in a conventional detector. From Figure 3.24, the addition of single-pole high-pass filters to the detector also proved to be an effective and economical solution to further reduce the self-noise. However the problem with small bandwidths is long acquisition times.

Bandwidths as large as 1 % of the symbol rate can be used provided that the loop contains a low-pass filter that is placed at the output of the early-late detector to filter the self-noise.

Simulation results with $B_L = 0.01$ are given in Figure 3.25. The loops containing either the conventional early-late or Gardner detectors were of order 2. The pole of the low-pass filter was at $z = 0.852$. The loops for the enhanced detectors were of order 3. The poles of the low-pass and high-pass filters were placed at the same distance from the unit circle (case A in Section 3.4.4). The pole of the high-pass filters

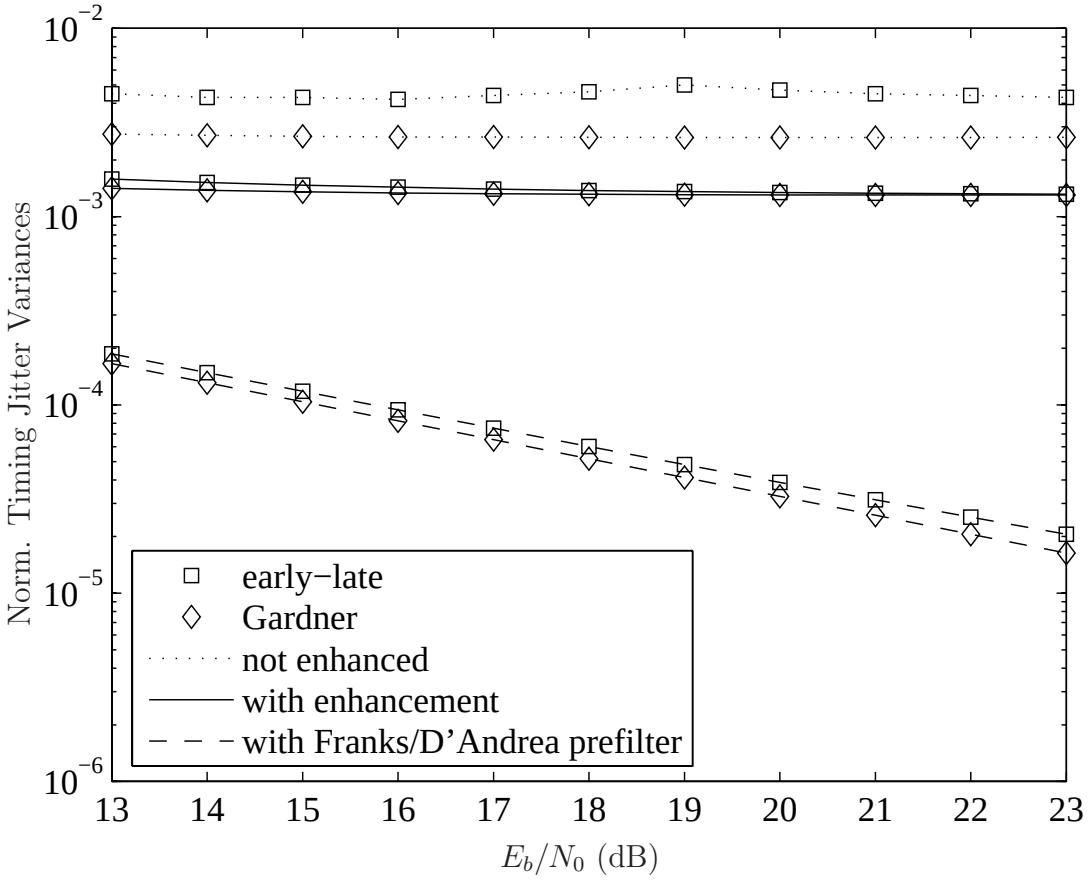

Figure 3.25 Normalized timing jitter ($T = 1$) variances for critically damped systems with a bandwidth equal to $B_L = 1$ % of the symbol rate.

was at $z = -0.7852$ and the pole of the low-pass filter at $z = 0.7852$. The loop gain was equal to $G_L = 0.0373$. The Franks/early-late and Franks/Gardner synchronizers were also equipped with a low-pass filter, which was identical to the one used in the second-order loop (e.g. $z = 0.852$).

An improvement in performance is obtained by enhancing the detectors. The timing jitter variance of the conventional early-late detector is reduced by about 4.5 dB over the 13 to 23 dB range of E_b/N_0.

4. Timing Jitter Analysis of the Franks/Gardner Symbol Synchronizer

4.1 Introduction

In systems where AWGN is very small, the Franks/Gardner synchronizer works very well. However in presence of significant AWGN the mid-samples are corrupted with noise, as Franks' prefilter can not force the noise to zero. The non-zero mid-sample causes error in the output of the Gardner detector. This error is injected in the loop and travels through the resampler. The end effect is timing jitter.

In this chapter the timing jitter in the Franks/Gardner synchronizer is analyzed after the timing recovery loop has acquired timing and operates in steady state mode. In this mode the timing jitter is stationary and is referred to as steady state timing jitter. An analysis of the steady state timing jitter is undertaken by deriving a closed-form expression for the Power Spectral Density (PSD) of the noise at the output of the Gardner detector. From that expression the variance of the steady state timing jitter is found using knowledge of the closed-loop frequency response. A simple equation is derived to relate the steady state timing jitter variance to the system bandwidth for small bandwidth systems. The performance of the Franks/Gardner synchronizer is also compared to the performance of the Oerder/Mehr synchronizer when the latter is equipped with Franks' prefilter. This comparison reveals that the Franks/Gardner synchronizer outperforms the Oerder/Mehr synchronizer.

Chapter 4 is organized as follows. In Section 4.2 models for the Gardner detector and the system containing the detector are given. A full characterization of the

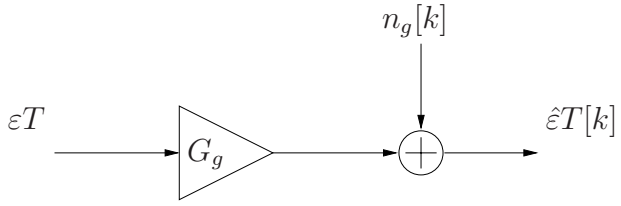

Figure 4.1 Linear model for the Gardner detector.

Gardner detector's model requires knowledge of the PSD of the noise produced by the detector and the S-curve equation. Closed-form expressions for the noise PSD as well as the S-curve equation are analytically derived in Section 4.3. A simple approximation for the timing jitter variance in the case of a system with small bandwidth is derived in Section 4.4. Verification of the Gardner detector's model and the timing jitter equation is the object of Section 4.5. In Section 4.6 the performance of the Franks/Gardner synchronizer and the Oerder/Mehr synchronizer when equipped with Franks' prefilter are compared against the MCRB.

4.2 System's model

The linear model for the Gardner detector, which was given in Figure 3.9 on page 69, is reproduced in Figure 4.1. The Gardner detector produces timing offset estimates, $\hat{\varepsilon}T[k]$, at the symbol rate. The model is valid for a small input timing offset, εT. The detector's output is decomposed into two component: a signal component and a noise component. The signal component is $G_g \times \varepsilon T$, where the gain, G_g, is equal to the derivative of the slope of the S-curve of the detector at $\varepsilon T = 0$, and the noise component, $n_g[k]$, has statistical properties that depend on εT. Noise, $n_g[k]$, originates from the Gaussian noise corrupting the QAM signal and the interaction of the QAM signal with the noise inside the detector.

For a constant timing offset, εT, $n_g[k]$ is a stationary sequence. The model is quite general and does not specify the PSD of $n_g[k]$ conditional to εT, nor the value of G_g. The PSD of the noise and the gain, G_g, depend on the filtering applied to the

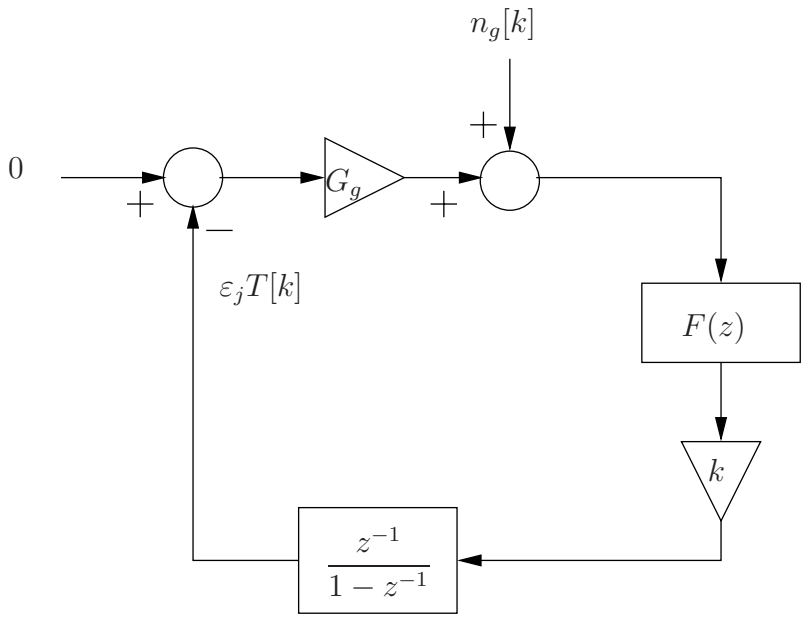

Figure 4.2 Linear model of the digital timing recovery loop in the Franks/Gardner synchronizer.

received signal prior to feeding it to the detector.

A model for the timing recovery loop of the Franks/Gardner synchronizer is given next. This model uses the model of the Gardner detector previously described.

The linear model for a digital timing recovery loop, which was given in Figure 3.4 on page 64, is reproduced in Figure 4.2, where $F(z)$ is the loop filter and $\frac{z^{-1}}{1-z^{-1}}$ models the accumulator. This model applies to steady state operation. Steady state operation is reflected in the model by setting the input, which is the timing offset, to zero. The model clearly shows that the steady state timing jitter, denoted by $\varepsilon_j T[k]$, is caused by the Gardner's detector noise, $n_g[k]$.

From the model given in Figure 4.2, one way to determine the PSD of $n_g[k]$ is to calculate the conditional PSD of $n_g[k]$ for a given timing offset. The PSD is then obtained by integrating the product of the conditional PSD and the Probability Density Function (PDF) of the timing offset with respect to the timing offset. To do this the PDF of the timing offset must be determined. This approach is somewhat impracti-

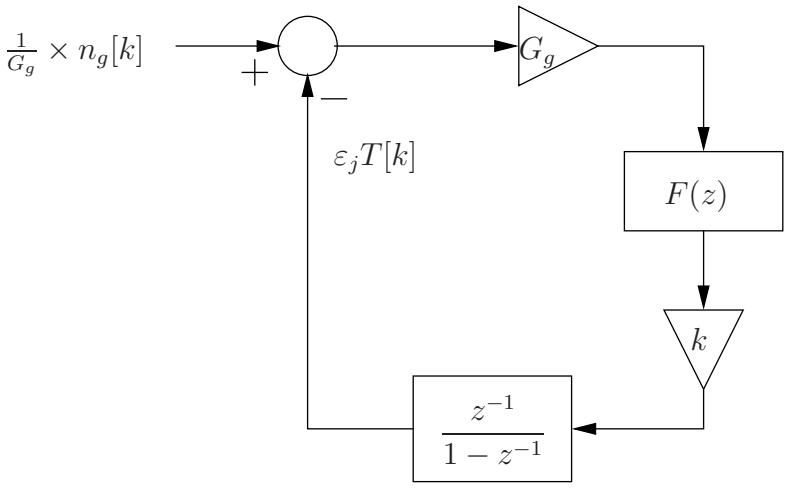

Figure 4.3 Rearranged model of the timing recovery loop with noise reflected to input.

cal since the PDF of the timing offset likely depends on the system bandwidth. An easier method [55], which is pursued here, is to use an approximation. In practical applications the steady state timing jitter is small, in which case the PSD of $n_g[k]$ is approximately equal to the PSD conditional to a timing offset of zero. Let the PSD of $n_g[k]$ be denoted by $S(e^{j\Omega T})$. Under the assumption that the timing jitter is small, $n_g[k]$ is independent of the timing offset and can be moved outside the loop as illustrated in Figure 4.3. The input of this rearranged model is $n_g[k]/G_g$.

From the rearranged model shown in Figure 4.3, the variance of the timing jitter, $\varepsilon_j T[k]$, is simply given by

$$\sigma_j^2 = \frac{1}{2\pi G_g^2} \int_{-\pi}^{\pi} S(e^{j\Omega T}) |H(e^{j\Omega T})|^2 d(\Omega T), \tag{4.1}$$

where

$$|H(e^{j\Omega T})| = H(z)|_{z=e^{j\Omega T}} = \frac{kG_g F(z) z^{-1}}{1-(1-kG_g F(z))z^{-1}}|_{z=e^{j\Omega T}}$$

is the closed-loop frequency response and σ_j^2 has units of T^2.

Closed-form expressions for $S(e^{j\Omega T})$ and G_g are derived in Section 4.3.

4.3 Linear model for the Gardner detector

The linear model shown in Figure 4.1 has parameter G_g and an additive noise signal. A closed-form expression for the power spectrum of the Gardner detector's noise as well as an expression for G_g are analytically derived in this section.

4.3.1 Power spectral density of the model noise

Calculation of the PSD is a tedious task that demands attention to details, many of which are subtle. The approach taken in this thesis is to find the DTFT of the noise for a truncated sequence of length, N, then take the ensemble average of its magnitude squared, and then take the limit as N goes to infinity in order to determine the PSD.

The details of the derivation of the PSD, which is denoted $S(e^{j\Omega T})$, can be found in Appendix F. The result, which has been checked by simulation, is given below.

For $r \leq 0.5$, the PSD of $n_g[k]$ is equal to

$$S(e^{j\Omega T}) = \begin{cases} \frac{2}{\pi}\left(S^{s\times n}(e^{j\Omega T}) + S^{n\times n}(e^{j\Omega T})\right), & 0 \leq \Omega T \leq 2r\pi, \\ 0, & 2r\pi < \Omega T < \pi, \end{cases} \tag{4.2}$$

where

$$\begin{aligned} S^{s\times n}(e^{j\Omega T}) &= \sigma_d^2\sigma_{w_I}^2 \int_{\Omega T-\pi r}^{\pi r} (1+\cos\theta)\cos^4\frac{\theta}{2r}\cos^2\frac{\theta-\Omega T}{2r}d\theta, \\ S^{n\times n}(e^{j\Omega T}) &= \sigma_{w_I}^4 \int_{\Omega T-\pi r}^{\pi r} (1+\cos\theta-2\sin\frac{\theta}{2r}\sin\frac{\theta-\Omega T}{2r}\cos\frac{\theta}{2}\cos\frac{\Omega T-\theta}{2}) \\ &\quad \times \cos^2\frac{\theta}{2r}\cos^2\frac{\theta-\Omega T}{2r}d\theta, \end{aligned} \tag{4.3}$$

where $\sigma_{w_I}^2$ is the variance of the real component of the low-pass equivalent bandpass white Gaussian noise.

4.3.2 Slope of S-curve parameter

A closed-form expression for the S-curve can be derived from Equation (25) in [16], once the frequency response of the end-to-end filter is specified. The end-to-end filter is obtained by cascading the two matched filters as well as the prefilter.

The S-curve equation, which is derived in Appendix G, is

$$g(\varepsilon T) = \frac{96}{\pi(64 - 20r^2 + r^4)}\sigma_d^2 \sin\frac{\pi}{2}r \sin\frac{2\pi\varepsilon T}{T},$$

where $\sigma_d^2 = E\{a^2[k]\} = E\{b^2[k]\}$ and $a[k] + jb[k]$ are the transmitted symbols.

The slope of $g(\varepsilon T)$ at $\varepsilon T = 0$ is the parameter, G_g. It is given by

$$G_g = \frac{dg(\varepsilon T)}{d\varepsilon T}|_{\varepsilon T=0} = \frac{1}{T}\frac{192\sigma_d^2}{64 - 20r^2 + r^4}\sin\frac{\pi}{2}r. \tag{4.4}$$

4.4 Estimation of the timing jitter variance

The variance of the timing jitter can be computed using (4.1), (4.2), and (4.4) along with numerical integration. In this Section an approximation to (4.1) is used so that numerical integration can be avoided.

From (4.2) it can be shown that the noise power spectrum, $S(e^{j\Omega T})$, is maximum at $\Omega T = 0$, and has a slope of 0 at $\Omega T = 0$. This means $S(e^{j\Omega T})$ can be approximated by its value at $\Omega T = 0$ in systems where the bandwidth is sufficiently small. Using this approximation (4.1) simplifies to

$$\sigma_j^2 = \frac{1}{2\pi G_g^2}S(e^{j0})\int_{-2\pi r}^{2\pi r}|H(e^{j\Omega T})|^2 d\Omega T, \tag{4.5}$$

The noise bandwidth, B_n, is by definition equal to (Section 3.4)

$$B_n = \frac{1}{4\pi}\int_{-2\pi r}^{2\pi r}|H(e^{j\Omega T})|^2 d\Omega T,$$

which means (4.5) can be expressed as

$$\sigma_j^2 = \frac{2}{G_g^2} \times B_n \times S(e^{j0}). \tag{4.6}$$

Evaluating (4.2) at $\Omega = 0$ and after a few manipulations, it is found that

$$S(e^{j0}) = \frac{2}{\pi}(\sigma_d^2 \times \sigma_{w_I}^2 + \sigma_{w_I}^4) \int_{-\pi r}^{\pi r} (1 + \cos\theta) \cos^6 \frac{\theta}{2r} d\theta. \tag{4.7}$$

Evaluating the integral in (4.7) produces

$$S(e^{j0}) = \frac{1}{\pi}\sigma_{w_I}^2(\sigma_d^2 + \sigma_{w_I}^2) \left(\frac{5\pi r}{4} + \frac{45 \sin \pi r}{36 - r^2(r^2-7)^2} \right). \tag{4.8}$$

Substituting (4.4) and (4.8) into (4.6) yields

$$\sigma_j^2 = C(r) \times B_n \times \frac{\sigma_{w_I}^2}{\sigma_d^4} \left(\sigma_d^2 + \sigma_{w_I}^2 \right) \times T^2, \tag{4.9}$$

where

$$C(r) = \frac{2}{\pi} \left(\frac{64 - 20r^2 + r^4}{192 \sin \pi r/2} \right)^2 \left(\frac{5\pi r}{4} + \frac{45 \sin \pi r}{36 - r^2(r^2-7)^2} \right). \tag{4.10}$$

From Appendix F $\sigma_d^2 = E_s$ and $\sigma_{w_I}^2 = N_0/T_s$, so $\dfrac{\sigma_d^2}{\sigma_{w_I}^2} = \dfrac{E_s T_s}{N_0}$, and (4.9) becomes

$$(\sigma_j/T)^2 = C(r) \times \frac{B_n}{E_s T_s/N_0} \left(1 + \frac{1}{E_s T_s/N_0} \right), \tag{4.11}$$

where $(\sigma_j/T)^2$ is the timing jitter variance normalized to the symbol period and is unit-less.

For $r < 0.1$, $C(r) \approx \dfrac{20}{9\pi^2 r}$, and

$$(\sigma_j/T)^2 = \frac{20}{9\pi^2 r} \times \frac{B_n}{E_s T_s/N_0} \left(1 + \frac{1}{E_s T_s/N_0} \right). \tag{4.12}$$

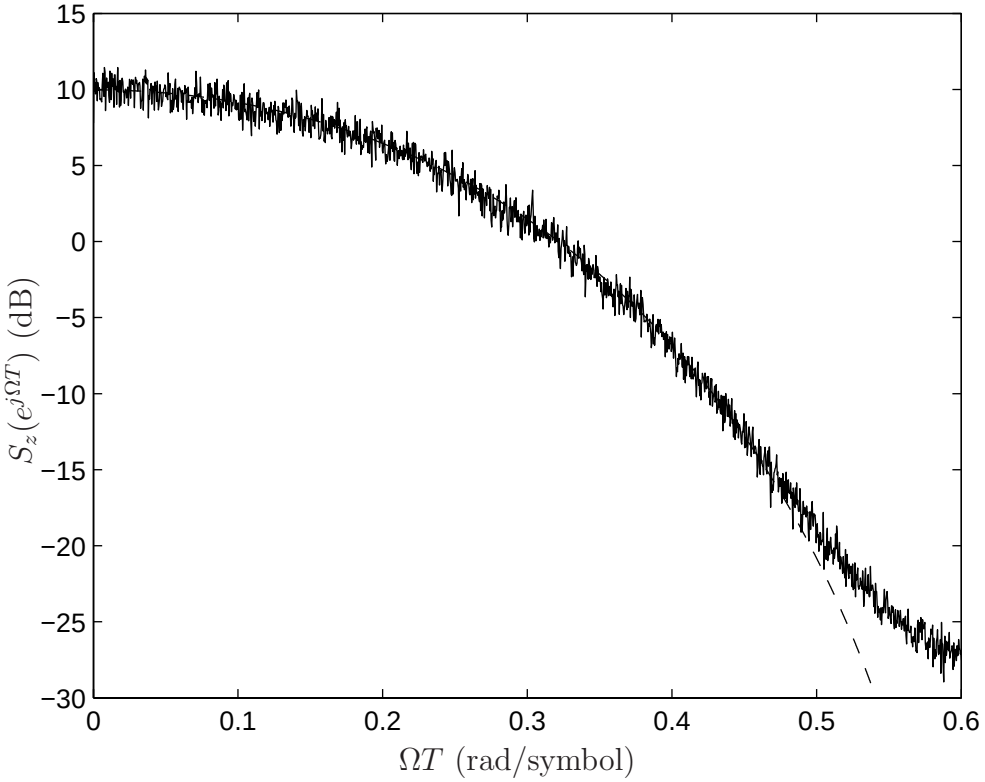

Figure 4.4 Noise power spectrum of the Gardner detector when Franks' prefilter is used to reshape the signal and $r = 0.1$ and $E_b/N_0 = 0$ dB.

4.5 Verification

Eq. (4.2) was verified with a computer simulation in a similar fashion to what was done in Section 2.5. The spectrum was estimated using Welch's 50 % overlapping method with blocks of size 16384 symbols. The PSD is plotted in Figure 4.4 along with the theoretical curve (dashed line) in the case of $r = 0.1$ and $E_b/N_0 = 0$ dB. The agreements between the curves strongly suggest that (4.2) is correct. Furthermore it shows that $S(e^{j\Omega T})$ is maximum at $\Omega T = 0$ and has a slope of zero at $\Omega T = 0$. This validates the approach taken to derive (4.12).

To verify (4.12) the Franks/Gardner synchronizer was simulated in a system very similar to the one described in Section 3.6. The feedback loop was of second-order with a noise bandwidth equal to 0.5 % of the symbol rate. The loop parameters were

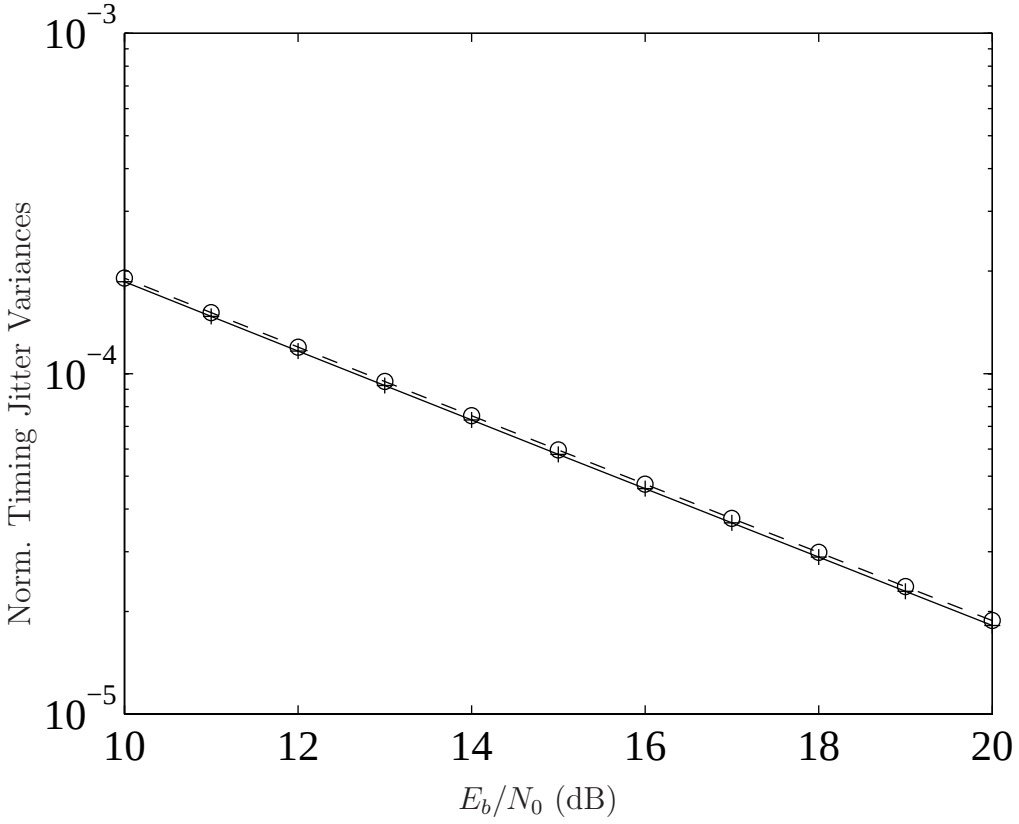

Figure 4.5 Theoretical (dashed curve) and measured (solid curve) normalized timing jitter variances for a critically damped system with a noise bandwidth of 0.5 % of the symbol rate and $r = 0.1$.

chosen to critically damp the system.

Curves of steady state normalized timing jitter variance versus $\frac{E_b}{N_0}$ are shown in Figure 4.5. The curve displaying the simulation results is a solid line with data points shown with a "+". The curves show the normalized jitter variance. The theoretical curve obtained from (4.12) is the dashed line with calculated points shown with a circle. The curves nearly coincide, which confirms the validity of (4.12) for small system bandwidths and small r.

4.6 Performance

In this section the performance of the Franks/Gardner synchronizer is compared to the Modified Cramer-Rao Bound (MCRB) [53] and to the performance of the Oerder/Mehr synchronizer for different system bandwidths and roll off factors. The performance measure is the variance of the steady state timing jitter.

Comparing the performance of both systems is not a simple task. The steady state timing jitter variance, σ_j^2, of the Franks/Gardner synchronizer is given by (4.1), and thus depends on the closed-loop frequency response, $|H(e^{j\Omega T})|$, whereas the steady state timing jitter variance of the feedforward Oerder/Mehr synchronizer depends on the interval of time over which the input signal is observed to produce a timing offset estimate [18]. So the main difference is that a feedfordward synchronizer (i.e., Oerder/Mehr synchronizer) estimates the timing offset over a finite interval, and a feedback synchronizer (i.e., Franks/Gardner) estimates the timing offset over an infinite interval due to the recursive nature of the timing recovery loop.

For comparison the two systems must be put on equal footing. This is effected by choosing an observation interval in the feedforward system to make the noise bandwidth of the feedforward system the same as the noise bandwidth of the closed-loop system. The feedforward system is a moving average filter of length L, so the noise bandwidth is $B_L = \dfrac{1}{2L}$ [53]. The noise bandwidth of the closed-loop system is $B_n = \dfrac{1}{4\pi}\displaystyle\int_{-\pi/T}^{\pi/T} |H(e^{j\Omega T})|^2 d\Omega$, where $H(e^{j\Omega T})$ is the closed-loop frequency response. Both systems have same noise bandwidth if and only if

$$L = \frac{1}{2B_n}. \tag{4.13}$$

The expression for the MCRB for timing offset, for which a derivation is given in Appendix A, is reproduced below

$$\frac{1}{T^2}\mathrm{MCRB}(\varepsilon \mathrm{T}) = \frac{1}{8\pi^2 \times \xi \times \mathrm{L} \times \mathrm{E_s/N_0}}, \tag{4.14}$$

where L, as in the case of the moving average filter, is an integer that represents the number of symbol intervals over which the input signal is observed to estimate εT, and ξ is a constant that depends on the roll off factor.

Timing jitter variance curves for the Franks/Gardner synchronizer along with the corresponding MCRB curves are plotted in Figure 4.6 for a bandwidth of 1 % of the symbol rate and roll off factors 0.1, 0.2, and 0.3. The curves were obtained by simulating the Franks/Gardner synchronizer with a 64-QAM input signal that was similar to the one used in the simulations of Chapter 3. The feedback loop was of second-order with $B_n = 0.01$ cycle/symbol-interval. The value to use for L in the MCRB expression is difficult to determine. The safe thing to do is to include the lengths (in symbol-intervals) of the matched filter and prefilter that precede the Franks/Gardner synchronizer. The lengths of the matched filter and prefilter used in the simulations were 20 and 40 symbols respectively, so a value of $L = 110$ was used in (4.14) to plot the MCRBs in Figure 4.6. This value L will produce a conservative MCRB.

Figure 4.6 shows six curves. The three MCRB curves for the three different values of r nearly coincide. The three curves for the Franks/Gardner synchronizer do not coincide. Figure 4.6 shows the performance increases as r increases. In the presence of a timing offset, there is less ISI corrupting the decision variables for a larger r. For $r = 0.1$ the timing jitter variance is about 11 dB greater than the MCRB and 7.5 dB greater than the MCRB for $r = 0.3$.

Similar plots are given in Figures 4.7 and 4.8 for noise bandwidths of 0.5 % and 0.1 % of the symbol rate. Using the same rule for determining L, a value of $L = 160$ was used to plot the MCRBs in Figure 4.7, and $L = 560$ was used for the MCRBs in Figure 4.8. Comparing the MCRB curves in Figures 4.7 and 4.8 to those in Figure 4.6 shows the MCRB improves with decreasing noise bandwidths. This is clear from (4.14), as the MCRB is inversely proportional to L, and L is inversely proportional to B_n.

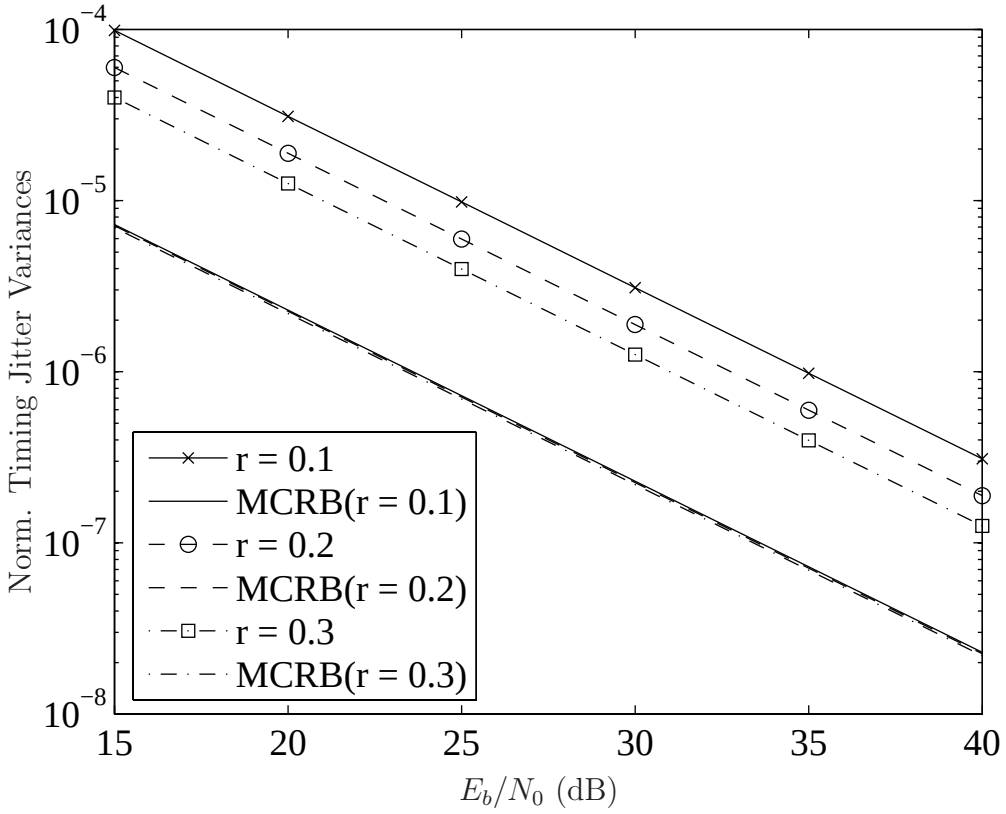

Figure 4.6 Normalized timing jitter variances along with the MCRBs for a critically damped system with a noise bandwidth of 1 % of the symbol rate and three values of r, 0.1, 0.2 and 0.3.

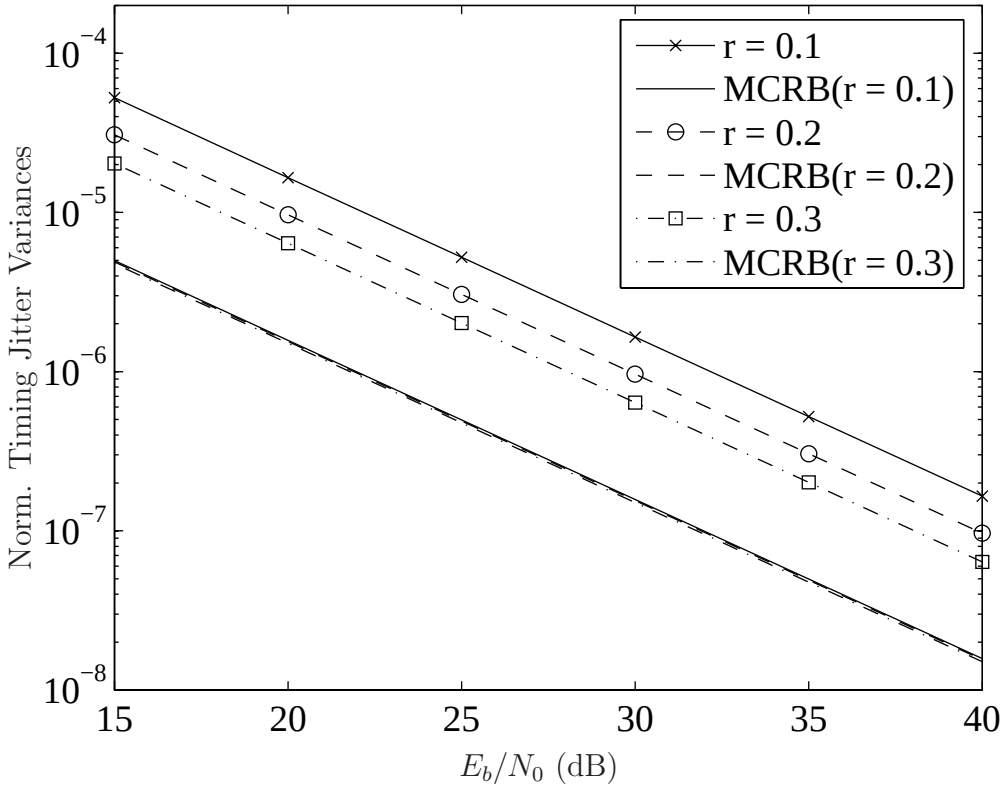

Figure 4.7 Normalized timing jitter variances along with the MCRBs for a critically damped system with a noise bandwidth of 0.5 % of the symbol rate and three values of r, 0.1, 0.2 and 0.3.

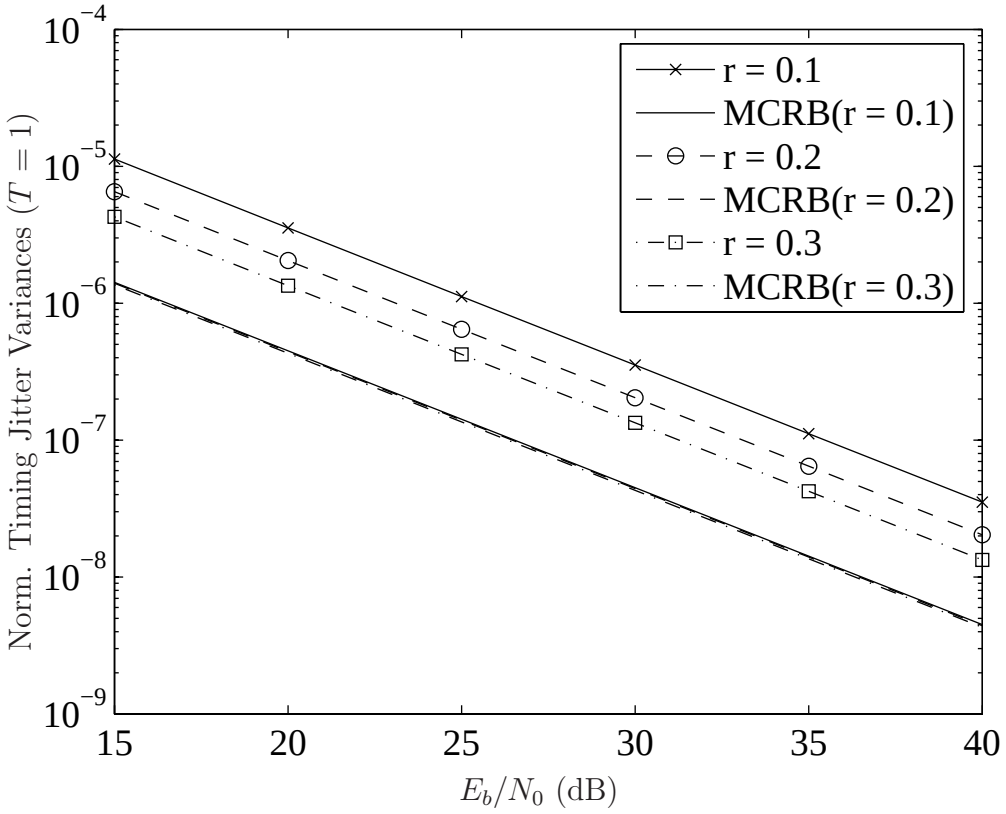

Figure 4.8 Normalized timing jitter variances along with the MCRBs for a critically damped system with a noise bandwidth of 0.1 % of the symbol rate and three values of r, 0.1, 0.2 and 0.3.

Comparing the curves for the Franks/Gardner synchronizer shows that the performance also improves for decreasing noise bandwidths. For a noise bandwidth of 0.5 % of the symbol rate and $r = 0.1$, the timing jitter variance is about 10 dB above the MCRB as opposed to 11 dB above the MCRB for the case of a 1 % noise bandwidth. For $r = 0.3$ it drops from 7.5 dB above the MCRB for a bandwidth of 1 % to 6 dB for a bandwidth of 0.5 %. From Figure 4.8 for a bandwidth of 0.1 % of the symbol rate and $r = 0.1$, the timing jitter variance is about 8.5 dB above the MCRB and 4.5 dB for $r = 0.3$. The results indicate that the performance gets closer to the MCRB as r decreases. These results also suggest that the Franks/Gardner synchronizer approaches the MCRB as the closed-loop bandwidth decreases, however this may be due in part to the value of L used to evaluate the MCRB being less conservative for smaller bandwidths.

The performance of the Oerder/Mehr feedforward synchronizer was evaluated for an input signal that was reshaped with Franks' prefilter. A 64-QAM signal with four samples per symbol interval and zero timing offset was corrupted with white Gaussian noise whose level was controlled by the operating E_b/N_0. This signal, after being filtered by the matched filter and Franks' prefilter, was passed to the Oerder/Mehr timing offset estimator. The Oerder/Mehr estimator produced an output by processing $L \times 4$ samples to compute the Fourier coefficient at digital frequency, $\pi/2$ radians/sample, and used the phase of that coefficient as an estimate of the timing offset. $5,000$ detector's outputs were recorded to estimate the variance of the timing jitter.

Timing jitter variance curves for the Franks/Oerder synchronizer (i.e., Oerder/Mehr synchronizer equipped with Franks prefilter) along with the Franks/Gardner synchronizer's curves previously shown in Figures 4.6-4.8 are plotted in Figures 4.9, 4.10, and 4.11. The curves shown in Figure 4.9 were obtained for a roll off factor of $r = 0.1$ and noise bandwidths of $B_n = 1$ %, 0.5 %, and 0.1 % of the symbol rate for Franks/Gardner and corresponding values of $L = 50$, 100, and 500 for Franks/Oerder. The results displayed in Figures 4.10 and 4.11 were obtained for the same three bandwidths and corresponding values for L, but with roll off factors of $r = 0.2$ and $r = 0.3$

respectively.

The Franks/Gardner synchronizer performs consistently better than the Franks/Oerder synchronizer and significantly better in the cases of high SNRs and small L. From Figure 4.9 the Franks/Gardner synchronizer has a variance that is 8 dB less than the Franks/Oerder synchronizer's variance at $E_s/N_0 = 40$ dB, $r = 0.1$, and $L = 50$. The reason is the Franks/Oerder has an additional self-noise component. This component introduces a noise floor, which causes a decrease in performance compared to the Franks/Gardner synchronizer as the SNR increases. From Figure 4.11 the variance of the Franks/Gardner synchronizer is 10.5 dB less than that of the Franks/Oerder synchronizer at $E_s/N_0 = 40$ dB, $r = 0.3$, $L = 50$ as opposed to 8 dB at $E_s/N_0 = 40$ dB, $r = 0.1$, and $L = 50$.

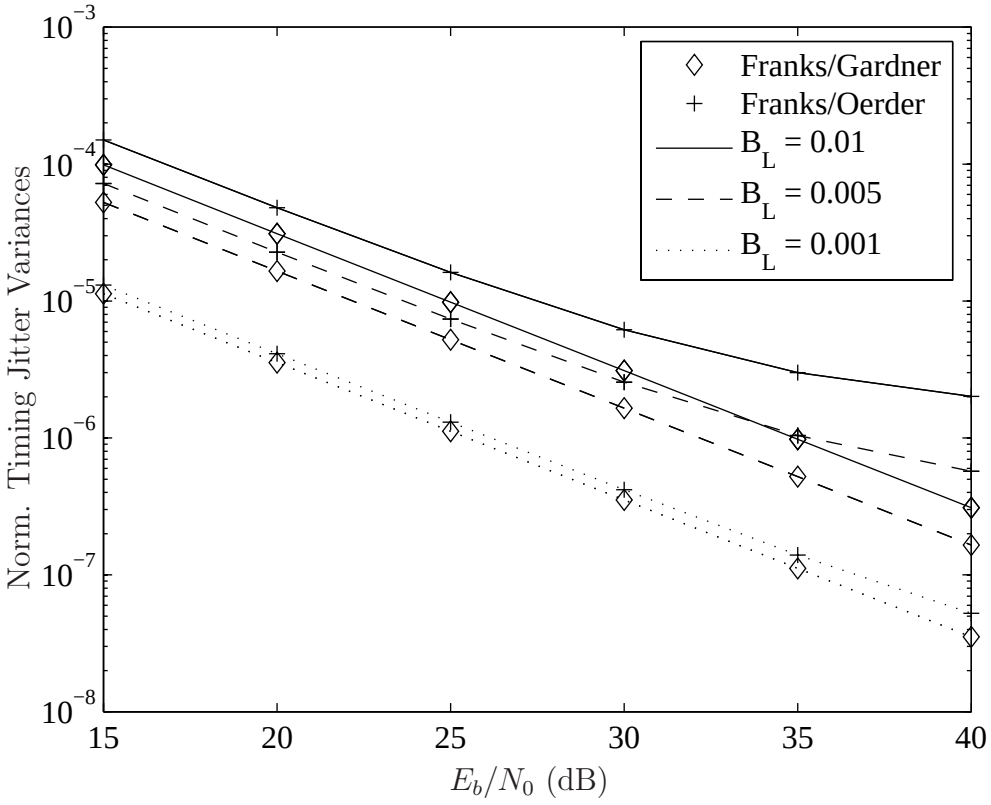

Figure 4.9 Timing jitter variances for the Franks/Oerder synchronizer with $L = 50$, 100, and 500 along with timing jitter variances for the Franks/Gardner synchronizer for a critically damped system with bandwidths of 1 %, 0.5 %, and 0.1 % of the symbol rate, and with roll off factor $r = 0.1$.

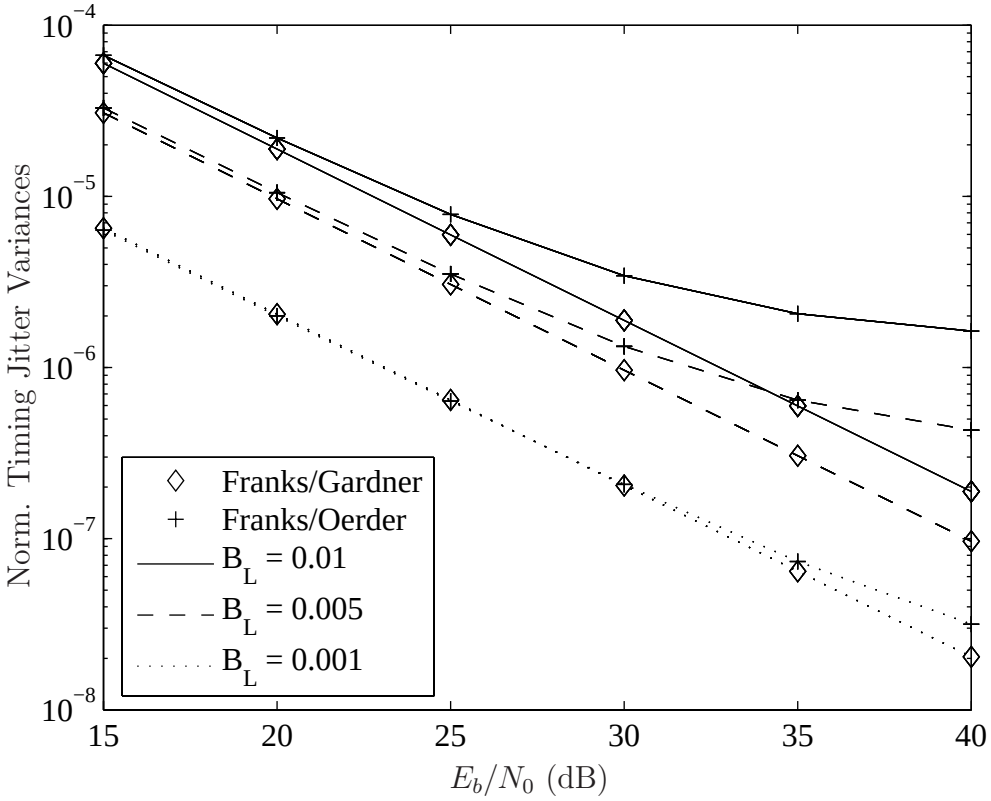

Figure 4.10 Timing jitter variances for the Franks/Oerder synchronizer with $L = 50$, 100, and 500 along with timing jitter variances for the Franks/Gardner synchronizer for a critically damped system with bandwidths of 1 %, 0.5 %, and 0.1 % of the symbol rate, and with roll off factor $r = 0.2$.

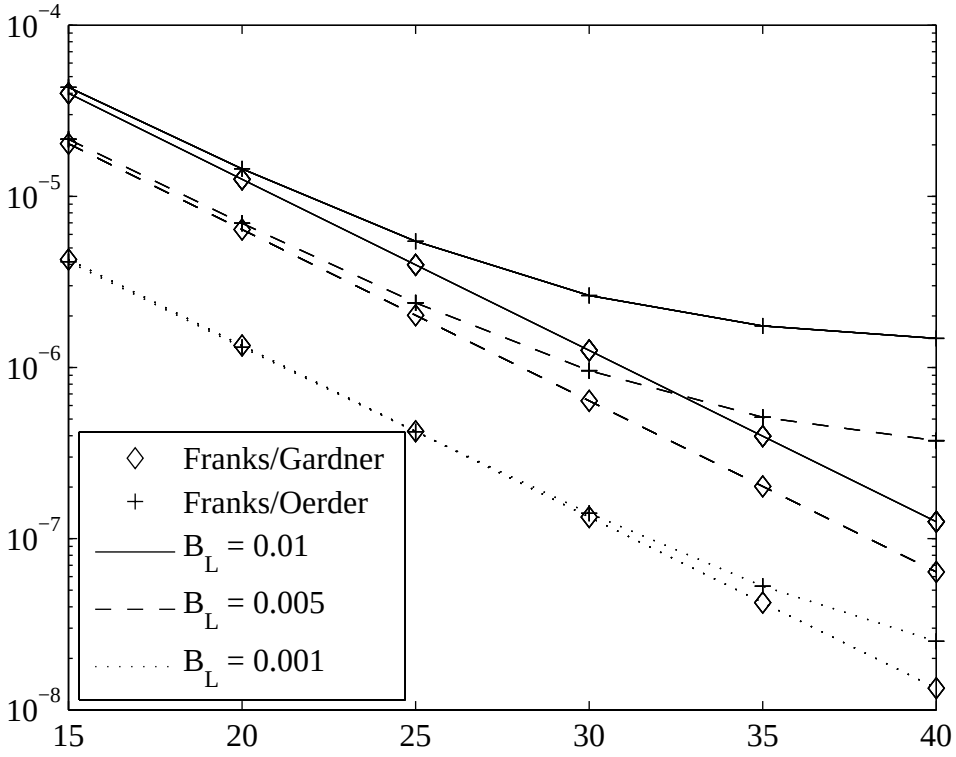

Figure 4.11 Timing jitter variances for the Franks/Oerder synchronizer with $L = 50$, 100, and 500 along with timing jitter variances for the Franks/Gardner synchronizer for a critically damped system with bandwidths of 1 %, 0.5 %, and 0.1 % of the symbol rate, and with roll off factor $r = 0.3$.

5. Frequency Coherent Detection in QPSK

5.1 Introduction

Detection schemes are commonly classified as being either coherent or incoherent. Coherent detection schemes are the ones that recover/estimate the phase of the unmodulated carrier and use that information in the detection of the transmitted symbol. The unmodulated carrier can be estimated in a variety of ways, one of which is a type II phase locked loop[1]. Typically in coherent detection schemes the output of the matched filter is counter-spun by multiplication with the rotating vector $e^{-j(\Delta\omega n+\psi_c+\psi_a)}$, where $\Delta\omega$ is the carrier frequency offset in radians / sample, $\Delta\omega n+\psi_c$ is the carrier phase offset and ψ_a is a phase ambiguity that could be 0 or $\pm\pi/2$ or π radians/sample. After counter spinning, the decision variables are in an orthogonal axis system that is rectified to the axis system in the transmitter, except there may be a rotational ambiguity of $\pm 90^o$ or 180^o. The ambiguity in the receiver's axis system is usually resolved by using differential encoding/decoding in the transmitter/receiver.

A widely used scheme in the class of incoherent detection is differential detection . Unlike coherent detection it does not establish a rigid axis system in the receiver that is rectified to the axis system in the transmitter. The decision variable is obtained by multiplication with the vector $e^{-j\phi_{k-1}}$, where ϕ_{k-1} is the phase of the output of the matched filter one symbol interval earlier. In essence this establishes a new axis system for each output of the matched filter. The axis system for output k is the one that has output $k-1$ on its positive real axis. Differential encoding must be used for the

[1]A type II phase locked loop is one that has zero steady state phase error in the presence of a frequency offset.

decision variable to be properly justified in the axis system. Coherent and differential detectors both have advantages and disadvantages. Differential detectors set up the axes system very quickly, with only two symbols. Coherent detectors take much longer as they must average over a very large number of symbols to get reasonable estimates of $\Delta\omega$ and ψ_c. The price for quick synchronization in differential detection is performance, as its axes system is based on a single received symbol, which has random rotation error. It is well known that the performance penalty for differential detection is 3 dB over coherent detection. However there are applications for example short-burst asynchronous packet transmission systems, where there is insufficient time for coherent detectors to recover phase. In these applications differential detection schemes are used.

In this chapter a novel coherent QPSK detector, referred to in this thesis as a frequency coherent detector, is proposed [54]. It has a performance penalty of about 1 dB over conventional coherent detectors but it has the advantage of setting up an axis system very quickly. It can be used in place of differential detectors and offers a performance advantage of about 2 dB. The carrier phase is recovered by using a novel scheme. However if the recovery scheme were to be modeled by a phase locked loop, it would have to be of type I.[2] Being a coherent detector, it counter spins the output of the matched filter. In this case the counter spinning is done by multiplication with $e^{-j(\Delta\omega n+\hat{\psi}_c+\psi_a)}$, where $\hat{\psi}_c$ is a biased estimate of ψ_c, with the bias depending on the frequency offset $\Delta\omega$.

The remainder of this chapter is organized into 3 sections. Section 5.2 explains the principle of operation of the proposed detector and provides a circuit that implements it. The results of a performance analysis are presented in Sections 5.3 and 5.4.

[2]A type I phase lock loop has a steady state phase error that is proportional to the frequency offset.

5.2 Structure of the frequency coherent detector circuit

The operation of the proposed frequency coherent detector hinges on the construction of the complex sinusoid that counter spins the decision variable. This complex sinusoid is denoted U_k. Its phase is an estimate of the carrier phase offset, except for an ambiguity of 0, $\pm 90^o$, or 180^o. Its amplitude is not important and can vary with time without affecting the performance of the detector.

The practical construction of U_k can be easily described. However it involves decision feedback, which makes it difficult to understand how the phase of U_k is an estimate of the carrier phase offset. To help understand how the phase of U_k is an estimate of the carrier phase offset, the construction of U_k is described from a behavioral point of view with many of the implementation issues swept aside.

The complex sinusoid, U_k, is derived from the output of the matched filter. The output, denoted by r_k, has the form $r_k = \sqrt{2E_s}e^{j(k\theta'+\theta_0+\phi_k)} + \eta_k$, where $k\theta' + \theta_0$ is the carrier phase offset with θ' being the frequency offset in radians / symbol-interval, ϕ_k is the information component which is referred to as the modulating phase, η_k is the complex Gaussian noise at the output of the matched filters, and E_s is the symbol energy of the transmitted QPSK signal. Decision feedback information is used to remove the modulation phase from r_k, to get $\widetilde{r}_k = \sqrt{2E_s}e^{j(k\theta'+\theta_0+\phi_a)} + \widetilde{\eta}_k$, where ϕ_a is a phase ambiguity that is either 0^o, $\pm 90^o$, 180^o. The phase ambiguity can not be avoided since there is insufficient information in the received signal to remove the modulating phase without leaving an unpredictable but constant error that may be 0^o, $\pm 90^o$, or 180^o. As explained in the sequel, this phase ambiguity does not affect the recovery of the transmitted modulating phases and is ignored by setting it to zero.

The unmodulated output of the matched filter, which has been denoted $\widetilde{r}_k$, is passed through a moving average filter to get U_k. If the moving average filter is of

length N, then U_k is given by

$$\begin{aligned} U_k &= \sum_{i=0}^{N-1} \widetilde{r}_{k-i} \\ &= \sqrt{2E_s} \sum_{i=0}^{N-1} e^{j((k-i)\theta' + \theta_0)} + \widetilde{\eta}_{k-i} \\ &= \sqrt{2E_s} e^{j(k\theta' + \theta_0)} \sum_{i=0}^{N-1} e^{j(-i\theta')} + \widetilde{\eta}_{k-i} \end{aligned} \tag{5.1}$$

As shown in Section 5.3, the expectation of U_k is $E\{U_k\} = Ae^{j(k\theta' + \theta_0 - \frac{N-1}{2}\theta')}$, where $A = \frac{\sin(N/2)\theta'}{\sin\theta'/2}\sqrt{2E_s}$. The phase of $E\{U_k\}$ is a biased estimate of the carrier phase offset with the bias being $(\frac{N-1}{2}\theta')$.

An implementable structure of the proposed frequency coherent detector circuit is given in Figure 5.1. The structure does not show the timing recovery circuit, but it assumes that timing has been recovered perfectly and the output of the matched filter is sampled at the correct decision times. These samples, which are denoted by r_k, are fed to the frequency coherent detector.

As illustrated in Figure 5.1 the construction of the reference involves constructing reference vector, U_k, by rotating and summing the N vectors, r_k, r_{k-1}, ..., r_{k-N+1}. The key step is the rotation of vector, r_k, by 0, $\pm 90^o$, or 180^o to align it within $\pm 45^o$ of U_{k-1}. The rotation is a simple operation since the elements of the rotation matrix are either 1 or -1. The rotated vector is denoted $\widetilde{r}_k$. In the circuit shown, $N = 4$.

The construction of vector U_k is illustrated in Figure 5.2 for $N = 2$. Vector r_{k-1} is rotated by 180^o to place it within $\pm 45^o$ of U_{k-2}. The rotated r_{k-1} is shown as $\widetilde{r}_{k-1}$ in the Figure. Then U_{k-1} is constructed from the equality $U_{k-1} = \widetilde{r}_{k-2} + \widetilde{r}_{k-1}$. Next $\widetilde{r}_k$ is found by rotating r_k to within $\pm 45^o$ of U_{k-1}. Finally U_k is calculated with $U_k = \widetilde{r}_{k-1} + \widetilde{r}_k$.

At startup $\widetilde{r}_{-N}$, $\widetilde{r}_{-N+1}$, ... , $\widetilde{r}_{-1}$ must be initialized. A natural approach is to

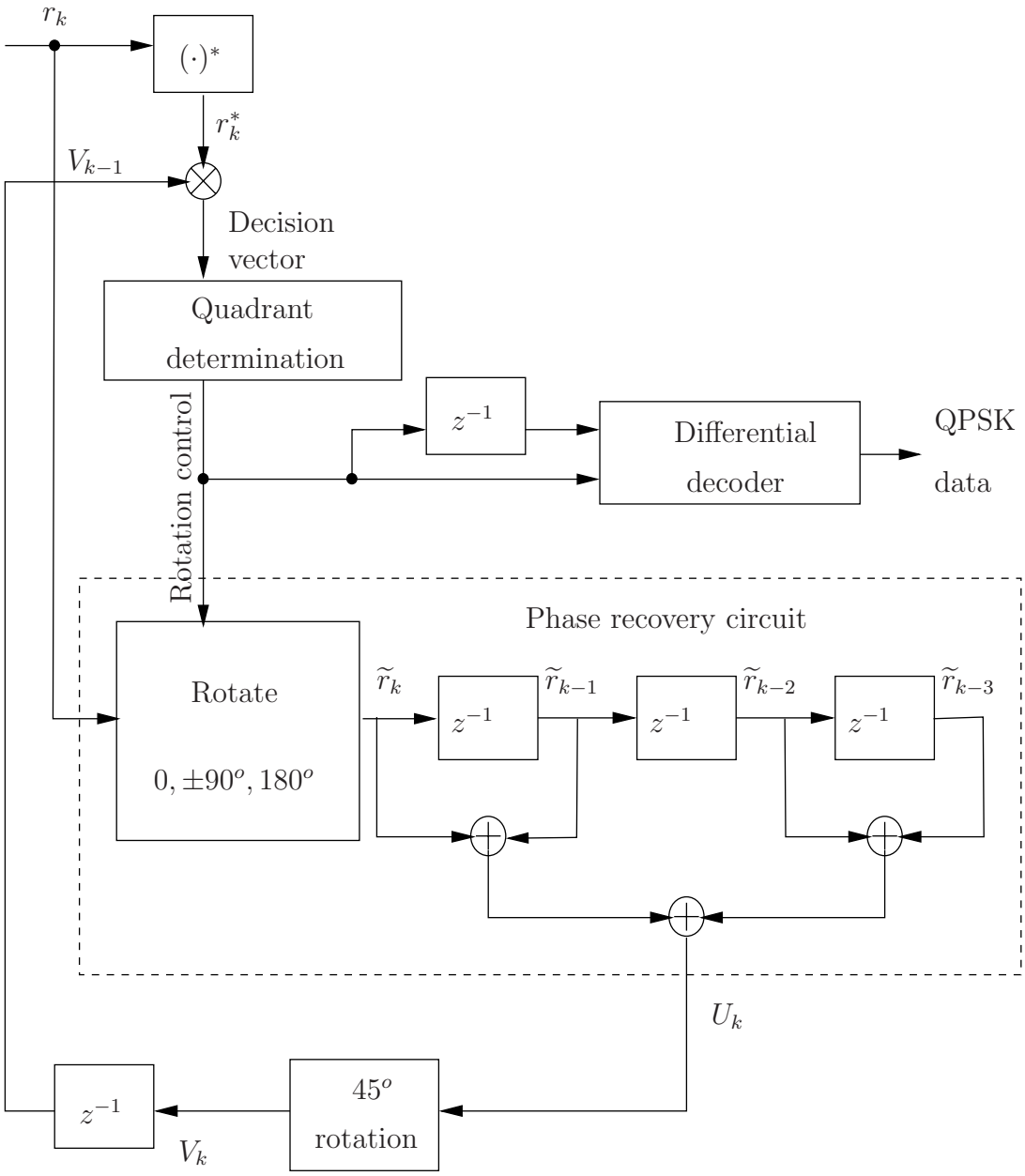

Figure 5.1 Frequency coherent detector for QPSK

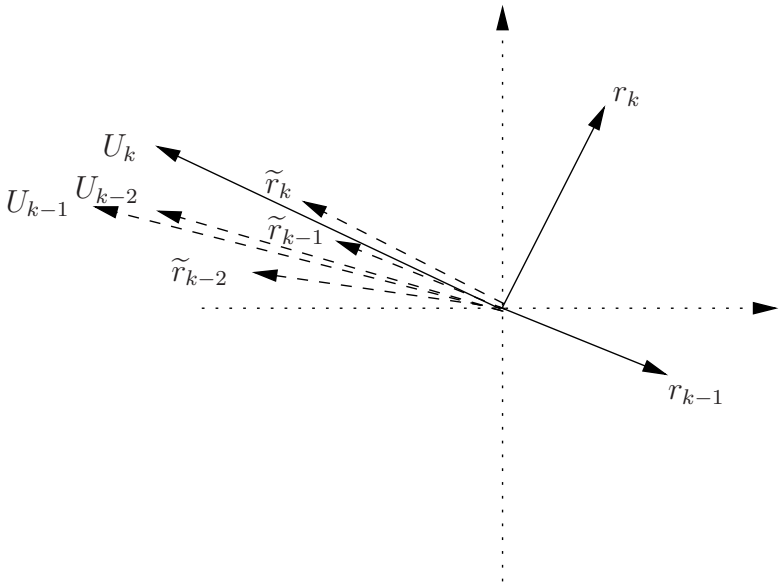

Figure 5.2 Construction of U_k.

initialize $\widetilde{r}_{-N}$, $\widetilde{r}_{-N+1}$, ..., $\widetilde{r}_{-1}$ with r_{-1}. Vector U_0 is simply r_{-1}, and the detector behaves like a conventional differential detector. The noise variance component of the reference vector will decrease over the next $N-1$ symbols, at which point U_{N-1} is the sum of N independent vectors. However if the preamble can be used to initialize $\widetilde{r}_{-N}$, $\widetilde{r}_{-N+1}$, ... , $\widetilde{r}_{-1}$ with N independent vectors, then U_0 has minimum noise variance.

Vector V_k is U_k rotated by 45^o (see Figure 5.1). The phase of r_k is compared to the phase of the rotated reference, V_{k-1}, by complex multiplication, where $*$ indicates complex conjugation. The reference vector U_k is rotated by 45^o so that in noise-free operation the decision vector, $r_k^* \times V_{k-1}$, has an angle of either $\pm 45^o$ or $\pm 135^o$. The decision boundaries are then the axes.

The phase of r_k with respect to U_{k-1} is estimated to be 0, 90^o, 180^o, or -90^o if the decision vector resides in quadrants 1, 2, 3, or 4 respectively. The quadrant determination is easily established using the sign bits of the real and imaginary parts of $r_k^* \times V_{k-1}$. The differential decoder recovers the two bits of information in r_k from the difference between the phase estimates of r_k and r_{k-1}.

5.3 Performance analysis for a small carrier frequency offset

The performance of the proposed circuit is determined analytically for a small carrier frequency offset, which is denoted by θ'. The matched filters have a square-root raised cosine frequency response and the complex sample, r_k, is given by

$$r_k = \sqrt{2E_s}e^{j(\phi_k+\theta_0+k\theta')} + \eta_k, \tag{5.2}$$

where $\phi_k \in [0^o, +90^o, 180^o, -90^o]$ is the modulating phase, $\theta_0 + k\theta'$ is the phase offset, and η_k is the complex Gaussian noise. For small θ' the distortions caused by the matched filter are negligible and are not considered in this analysis.

A close approximation to the probability of a symbol error, P_s, is derived as follows.

For a symmetric signaling set such as QPSK, the probability, P_s, of a symbol error does not depend on the information in the symbol. With no loss of generality let ϕ_k be zero in (5.2), and $r_k = \sqrt{2E_s}e^{j(\theta_0+k\theta')} + \eta_k$. The samples r_k, $k = 0, 1, \ldots$, are independent, as they are spaced one symbol interval apart. The variance of η_k is $2N_0$, therefore r_k has variance $2N_0$, where $2N_0$ is the one-sided spectral density constant of the white Gaussian noise at the input of the matched filter.

The probability that the decision vector, $r_k^* \cdot V_{k-1}$, is in quadrant 1, which is the probability of being correct, is denoted by P_c. P_c is given by

$$P_c = \frac{1}{2\pi(\sigma^2/2)} \int_0^\infty e^{-\frac{(x-\mu_x)^2}{\sigma^2}} dx \int_0^\infty e^{-\frac{(y-\mu_y)^2}{\sigma^2}} dy, \tag{5.3}$$

where μ_x and μ_y are the real and imaginary parts of the mean of the decision vector, denoted by μ, and σ^2 is the variance of the decision vector. With changes of variables $x \to \sqrt{2}(x-\mu_x)/\sigma$ and $y \to \sqrt{2}(y-\mu_y)/\sigma$, (5.3) reduces to

$$P_c = \left(1 - Q\left(\frac{\sqrt{2}\mu_x}{\sigma}\right)\right)\left(1 - Q\left(\frac{\sqrt{2}\mu_y}{\sigma}\right)\right), \tag{5.4}$$

where $Q(y) = \frac{1}{\sqrt{2\pi}} \int_y^{+\infty} e^{-x^2/2} dx$ is the Q-function. The Q function if expressed in terms of the complimentary error function, erfc, is given by $Q(y) = \frac{1}{2}\text{erfc}\left(\frac{\text{y}}{\sqrt{2}}\right)$.

A symbol error occurs if the algorithm decides on a different quadrant than quadrant one. In differential decoding symbol errors usually occur in pairs. Therefore P_s is very nearly twice that of $1 - P_c$, and from (5.4) is approximately given by

$$\begin{aligned} P_s \approx & 2Q\left(\frac{\sqrt{2}\mu_x}{\sigma}\right) + 2Q\left(\frac{\sqrt{2}\mu_y}{\sigma}\right) \\ & - 2Q\left(\frac{\sqrt{2}\mu_x}{\sigma}\right) Q\left(\frac{\sqrt{2}\mu_y}{\sigma}\right) \end{aligned} \tag{5.5}$$

5.3.1 Mean and variance of decision vectors

The mean of the decision vector, μ, is equal to $E\{r_k^* \cdot V_{k-1}\} = E\{r_k^*\}E\{V_{k-1}\}$, where $E\{\cdot\}$ is the expectation operator. The reference vector is

$$\begin{aligned} U_{k-1} &= \left(\sum_{n=0}^{N-1} \widetilde{r}_{k-1-n}\right) \\ &= \sum_{n=0}^{N-1} \left(\sqrt{2E_s} e^{j(\theta_0 + (k-1-n)\theta')} + \widetilde{\eta}_{k-n-1}\right), \end{aligned}$$

where $\widetilde{\eta}_{k-n-1}$ is the noise component of $\widetilde{r}_{k-n-1}$. Since $\widetilde{\eta}_k$ has zero-mean,

$$\begin{aligned} E\{V_{k-1}\} &= E\{e^{j\frac{\pi}{4}} U_{k-1}\} \\ &= \sqrt{2E_s} e^{j(\theta_0 + (k-1)\theta' + \frac{\pi}{4})} \sum_{n=0}^{N-1} e^{-jn\theta'}. \end{aligned} \tag{5.6}$$

Also since $\widetilde{\eta}_k$ has zero-mean,

$$E\{r_k^*\} = \sqrt{2E_s} e^{-j(\theta_0 + k\theta')}.$$

The sum in (5.6) is equal to

$$\sum_{n=0}^{N-1} e^{-jn\theta'} = \begin{cases} N, & \theta' = 0 \\ \dfrac{\sin N\theta'/2}{\sin \theta'/2} e^{-j\theta'(N-1)/2}, & \theta' \neq 0. \end{cases} \tag{5.7}$$

The mean of the decision variable is then

$$\mu = \begin{cases} 2NE_s e^{j\frac{\pi}{4}}, & \theta' = 0 \\ 2\dfrac{\sin N\theta'/2}{\sin \theta'/2} E_s e^{j(\frac{\pi}{4} - \theta'(N+1)/2)}, & \theta' \neq 0. \end{cases} \tag{5.8}$$

The decision vector variance, σ^2, is given by

$$\begin{aligned} \sigma^2 &= E\{|r_k^* \times V_{k-1} - \mu|^2\} \\ &= E\{|r_k|^2\} E\{|V_{k-1}|^2\} - |\mu|^2. \end{aligned} \tag{5.9}$$

From (5.2)

$$E\{|r_k|^2\} = 2E_s + 2N_0, \tag{5.10}$$

and from (5.6)

$$\begin{aligned} E\{|V_{k-1}|^2\} = 2E_s \left| \sum_{n=0}^{N-1} e^{-jn\theta'} \right|^2 + \\ E\left\{ \left(\sum_{n=0}^{N-1} \widetilde{\eta}_{k-1-n} \right) \left(\sum_{n=0}^{N-1} \widetilde{\eta}_{k-1-n} \right)^* \right\} \end{aligned} \tag{5.11}$$

Substituting (5.7) into (5.11) and then (5.8), (5.10), and (5.11) into (5.9) yields

$$\sigma^2 = \begin{cases} 4(N + N^2)E_s N_0 + 4NN_0^2, & \theta' = 0 \\ 4(N + \dfrac{\sin^2 N\theta'/2}{\sin^2 \theta'/2})E_s N_0 + 4NN_0^2 & \theta' \neq 0. \end{cases} \tag{5.12}$$

5.3.2 Probability of a symbol error

From (5.5), (5.8) and (5.12) it is found after some algebraic manipulations that

$$\begin{aligned} P_s \approx\ & 2Q\left(\cos(\frac{\pi}{4}-\frac{\theta'(N+1)}{2})\sqrt{\frac{2NA(\theta')}{NA(\theta')+(1+\frac{N_0}{E_s})}\frac{E_s}{N_0}}\right) \\ & + 2Q\left(\sin(\frac{\pi}{4}-\frac{\theta'(N+1)}{2})\sqrt{\frac{2NA(\theta')}{NA(\theta')+(1+\frac{N_0}{E_s})}\frac{E_s}{N_0}}\right) \\ & - 2Q\left(\cos(\frac{\pi}{4}-\frac{\theta'(N+1)}{2})\sqrt{\frac{2NA(\theta')}{NA(\theta')+(1+\frac{N_0}{E_s})}\frac{E_s}{N_0}}\right) \\ & \times Q\left(\sin(\frac{\pi}{4}-\frac{\theta'(N+1)}{2})\sqrt{\frac{2NA(\theta')}{NA(\theta')+(1+\frac{N_0}{E_s})}\frac{E_s}{N_0}}\right), \end{aligned} \tag{5.13}$$

where

$$A(\theta') = \begin{cases} 1, & \theta' = 0 \\ \left(\dfrac{\sin N\theta'/2}{N\sin\theta'/2}\right)^2, & \theta' \neq 0. \end{cases}$$

Two approximations were made in the calculation of P_s, both of which are pessimistic. The first approximation is that in constructing $\widetilde{r}_k$, the decision to rotate r_k by 0^o, 90^o, 180^o, or -90^o, in order to be within $\pm 45^o$ of U_{k-1}, is based on $r_k - \eta_k$ (i.e., a noise-free r_k) rather than r_k. A difference between the algorithm and the analysis only occurs when η_k is sufficiently large to cause $r_k^* \cdot V_{k-1}$ and $(r_k - n_k)^* \cdot V_{k-1}$ to be in different quadrants, e.g. when r_k is large enough to cause a symbol error. In such a case the algorithm rotates r_k by an extra $\pm 90^o$ or 180^o to place $\widetilde{r}_k$ within $\pm 45^o$ of U_{k-1}. This makes the angle between $\widetilde{r}_k$ and U_{k-1} smaller in the algorithm than in the analysis. The end effect is that the analysis yields a variance for U_{k-1} that is slightly higher than what is produced by the algorithm.

The second approximation concerns the differential decoder. If η_k is large enough to cause an error for r_k, then the analysis assumes that the decoder generates a second error for r_{k+1}. This is slightly pessimistic, since on occasions η_k and η_{k+1} may be large

enough to both create errors. In that case the decoder generates 3 symbol errors, but the analysis assumes 4.

For $N\theta'$ small $A(\theta') \approx 1$. Also for $E_s/N_0 \gg 1$ the third term on the right side of (5.13) is very small and can be neglected. Probability P_s can then be approximated by

$$P_s \approx 2Q\left(\cos(\frac{\pi}{4} - \frac{\theta'(N+1)}{2})\sqrt{\frac{2N}{N+1}\frac{E_s}{N_0}}\right) + 2Q\left(\sin(\frac{\pi}{4} - \frac{\theta'(N+1)}{2})\sqrt{\frac{2N}{N+1}\frac{E_s}{N_0}}\right). \quad (5.14)$$

The increase in performance obtained with the proposed frequency coherent detector detector is illustrated in Figure 5.3 for different values of N and no frequency offset (i.e., $\theta' = 0$). Using (5.14) the probabilities of a symbol error (i.e., symbol error rate) for $N = 2$, $N = 4$ and $N = 8$ are plotted against E_b/N_0, where $E_b = (1/2)E_s$ is the received energy per bit. The symbol error rate for coherent detection with differential decoding, which is approximately equal to $4Q\left(\sqrt{\frac{E_s}{N_0}}\right)$, as well as the error rate for conventional differential detection, which is approximately equal to $2Q\left(\sqrt{\frac{E_s}{2N_0}}\right)$, are also plotted on the same graph.

As shown in Figure 5.3 the increase in performance over differential detection when $N = 4$ is 1.9 dB for E_b/N_0 in the 14 to 20 dB range. Performance degradation over coherent detection (with differential decoding) is 1 dB.

5.4 Performance verification

The performance of the proposed circuit is verified with simulation and compared to the performances of the conventional differential detector and the coherent detector. The verifications and comparisons are made for $N = 4$ and frequency offsets of 0, 1, and 2 degrees/symbol. The proposed circuit was simulated in Matlab/Simulink. The in phase and quadrature components of a QPSK signal were generated with 2 samples

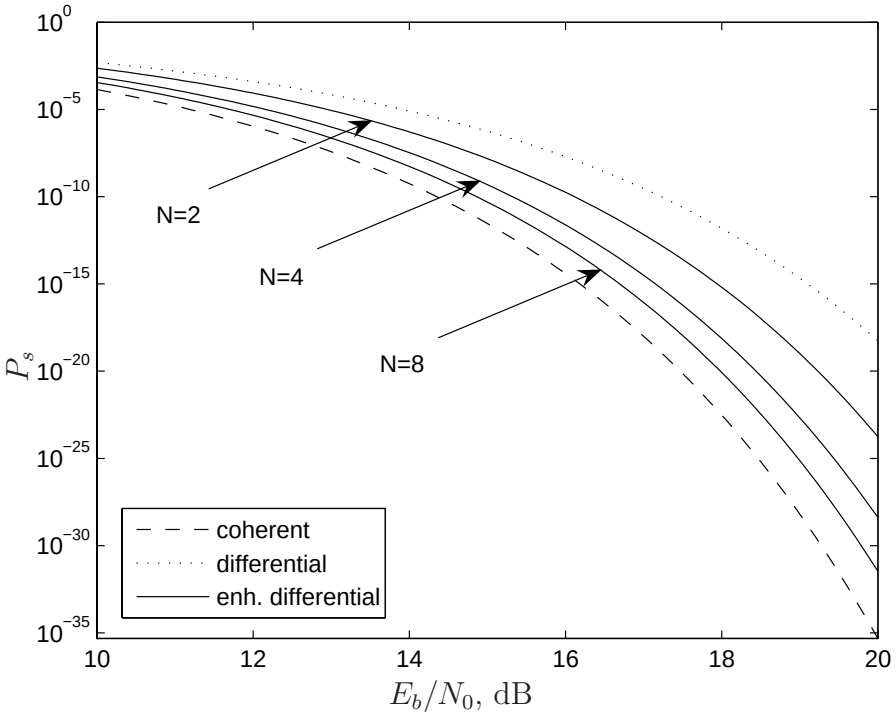

Figure 5.3 Probability of symbol error vs. E_b/N_0 for the frequency coherent detector detector with $N = 2, 4, 8$ along with curves for conventional differential detection and coherent detection with differential decoding.

per symbol. The signal was 500,000 symbols in length. A roll off factor of 0.25 was used in the matched filter. The complex baseband signal was corrupted with AWGN. The frequency offset was introduced by multiplying the complex baseband signal by a complex sinusoid, and the signal obtained was filtered with the matched filter. The output of the matched filter was down-sampled by 2 to produce r_k. The block diagram in Figure 5.1 was then simulated using r_k as input.

The operating E_b/N_0 was varied in 1 dB steps from 10 to 20 dB. The mean and variance of the decision vector, which are denoted $\widehat{\mu}$ and $\widehat{\sigma}^2$, were estimated using the simulation results. P_s was estimated from (5.5) using $\widehat{\mu}_x$, $\widehat{\mu}_y$, and $\widehat{\sigma}^2$ in place of μ_x, μ_y, and σ.

Probability of symbol error curves versus E_b/N_0 are shown in Figure 5.4 for the conventional differential detector and the proposed circuit, as well as for the coherent detector. In all cases differential decoding is used. Parameter N is set to 4. Theoretical curves for frequency offsets of 0, 1 and 2 degrees/symbol are shown for both the conventional and enhanced differential detectors. The symbol error rate for conventional differential detection with a small frequency offset, θ', is approximately equal to $Q\left(\cos\left(\frac{\pi}{4}-\theta'\right)\sqrt{\frac{E_s}{N_0}}\right)+Q\left(\sin\left(\frac{\pi}{4}-\theta'\right)\sqrt{\frac{E_s}{N_0}}\right)$. The simulation results are marked with a "*", a "+", and a "x". The close agreement between the points found by simulations and the theoretical curves confirm the validity of (5.13).

It can be seen in Figure 5.4 that the proposed circuit is more sensitive to frequency offset than the conventional differential detector. However for frequency offsets, θ', that are less than 1 degrees/symbol, the performance gain is at least 1.7 dB for E_b/N_0 in the 14 to 20 dB range of E_b/N_0.

A comparison with Divsalar's algorithm [27] reveals that the frequency coherent detector outperforms Disvalar's detector. For $E_b/N_0 = 13$ dB, Divsalar's detector offers 1.5 dB improvement over differential detection, versus 1.9 dB improvement obtained with the frequency coherent detector. This comparison was made in the case of no frequency offset. The Divsalar's performance measurement was obtained

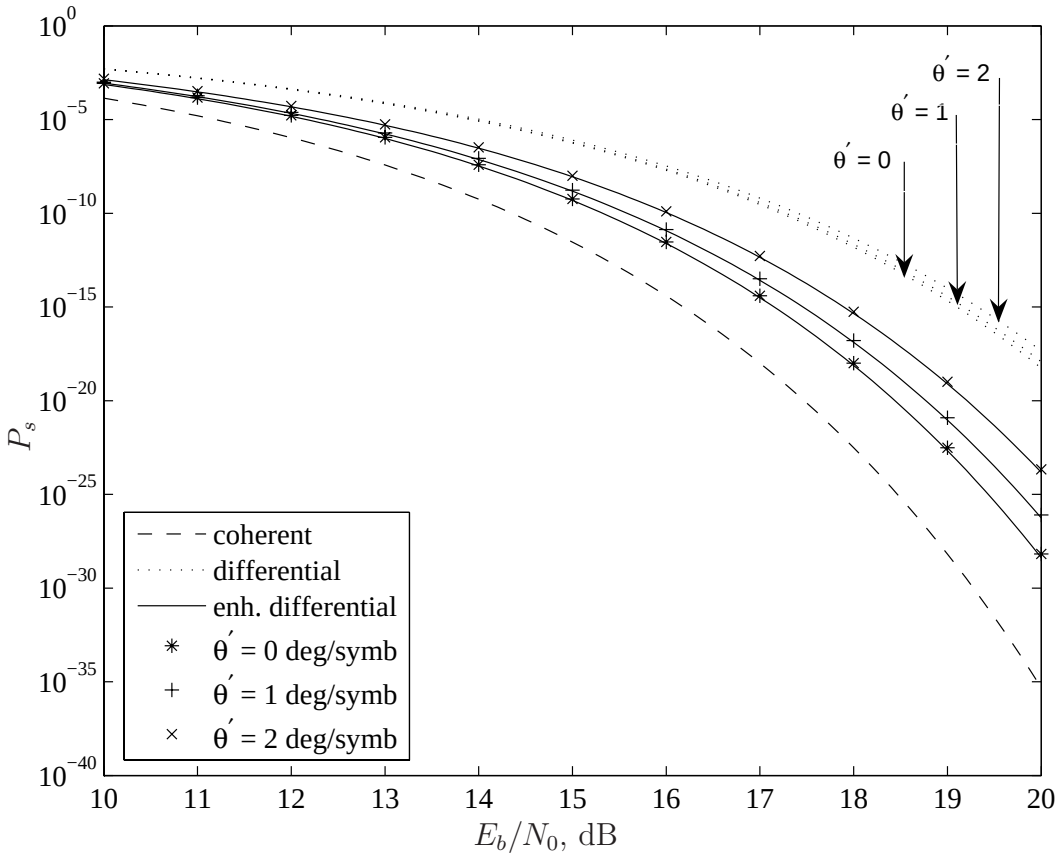

Figure 5.4 Probability of symbol error curves for the proposed circuit with $N = 4$ and frequency offsets $\theta' = 0, 1, 2$ degrees/symbol with 3 sets of simulation results marked with "*", "+" and "x".

from the graph given in [27; Fig. 5].

6. Conclusion

6.1 Summary

Of interest in this research is the non-data-aided timing synchronizers proposed by D'Andrea [17] to recover timing. High performance is achieved by reshaping the received signal prior to estimating the timing. Reshaping is performed by means of a relatively long FIR filter, which consumes a large number of multipliers. In this research a first contribution is made by proposing an alternative to the Franks / Gardner synchronizer. The long FIR filter is replaced with two single poles IIR filters. This novel architecture for filtering self-noise is more suited for FPGA design. However the large reduction in multipliers comes at the expense of a loss in performance.

A second contribution is the analysis of the steady state timing jitter of the Franks/Gardner synchronizer. A closed-form expression for the noise power spectrum is derived along with an equation to estimate the variance of the jitter in systems with narrow closed-loop bandwidths. It is also shown that the Franks/Gardner synchronizer outperforms the Oerder/Mehr square detector when the latter also uses Franks' prefilter prior to estimating the timing offset. The performance measure is the variance of the steady state timing error.

A third contribution is made by proposing a novel frequency coherent detector for QPSK. A detailed description of these three contributions is given next.

6.2 Research contributions

6.2.1 Enhanced non-data-aided feedback synchronizer

Self-noise reduction in the early-late and Gardner detectors was obtained by analytically deriving an equation for the S-curve of the early-late detector. This equation revealed which portion of the spectrum provides timing information and which portion only contributes to self-noise. It was found that the timing information in a QAM signal that is sampled at the symbol rate is contained in the frequency band $[(1-r)\pi, (1+r)\pi]$ radians / sample. The frequency band $[-(1-r)\pi, (1-r)\pi]$ radians / sample only contributes to self-noise and can be filtered with a high-pass filter. In contrast with Franks' prefilter, the high-pass filter does not need linear phase and a single-pole IIR filter can be used to approximate the high-pass filter. A novelty in this research is that the single-pole filter is directly incorporated inside the detector. Two filters are required: one to process the "early" signal, and one to process the "late" signal. Only these signals are affected. The "on-time"signal, which is used to detect the symbol is not affected by the filters, and no second resampler is required.

The addition of single-pole high-pass filters inside the feedback loop do not affect its stability. This has been verified by deriving a linear model for the detector and performing a linear analysis of the loop. The addition of the single-pole high-pass filters increases the order of the loop by 1. The loop is of order 3 if a single-pole low-pass filter is also present at the output of the detector. An algorithm has been devised to determine the position of the poles in a loop of order 3 for a given noise bandwidth.

The presence of single-pole high-pass filters enhances the performance of the detector. Simulations revealed an 8 dB reduction in timing jitter variance for $E_b/N_0 = 23$ dB and a noise bandwidth of 0.1 % of the symbol rate. The enhanced detector does not perform as well as the Franks / Gardner detector. This is not a surprise since the filtering used in the enhanced detector is not as sophisticated as the prefilter of the Franks / Gardner synchronizer. However the reduction in the number of multi-

pliers is significant since for both the in phase and quadrature signal streams, only one resampler is required instead of 2, and the prefilter is replaced with 2 single-pole filters.

The novel self-noise reduction technique proposed here can also be applied to the Gardner detector. The simulation shows that the Gardner detector outperforms the early-late detector when they are used in their conventional form, but loses its advantage when both detectors are enhanced.

Another contribution is a closed-form expression for the self-noise power spectrum of the early-late detector when it is enhanced with an ideal high-pass filter. This expression also serves as an approximation to the power spectrum of the self-noise of the conventional early-late detector for low frequencies. The steady state self-noise power spectrum of the early-late detector is proportional to ω^2 for small ω whether or not the detector is enhanced with a high-pass filter. This spectrum can be suppressed for ω greater than $2r\pi$ radians/sample without affecting the S-curve.

6.2.2 Timing jitter analysis of the Franks / Gardner synchronizer

The peculiar characteristic of the Franks/Gardner synchronizer is that self-noise is nonexistent when timing is perfect. The presence of steady state timing jitter in the timing recovery loop is due to 1) the interaction of the Gaussian noise with the signal inside the Gardner detector and 2) the interaction of the noise with itself. This dual interaction clearly appears in the closed-form expression for the power spectrum output of the detector derived in this analysis. This expression contains two terms: one term is due to the signal times noise interactions and the other terms represent the noise times noise interactions.

The power spectrum is maximum at $\omega = 0$ radians/sample and flat for low-frequencies. In the case of a system with a small closed-loop bandwidth, the power spectrum can be approximated by its value at $\omega = 0$ radians/sample. A simple equation is derived to estimate the timing jitter variance in systems with a small

bandwidth. In systems with medium to large bandwidths, the approximation of the power spectrum by a constant may not hold. In that case the timing jitter variance is estimated by means of a numerical integration involving the power spectrum expression and the closed-loop frequency response.

Timing jitter variance curves were plotted for different noise bandwidths and roll off factors, along with the MCRB. It is found that the performance of the Franks/Gardner synchronizer closely approaches the bound as the noise bandwidth becomes smaller and the roll off factor increases. For a noise bandwidth of 0.1 % of the symbol rate and a roll off factor of $r = 0.3$, the variance of the timing jitter is about 4.5 dB above the MCRB.

Timing jitter variance curves for the Oerder/Mehr synchronizer when equipped with Franks' prefilter were also plotted along with the timing jitter variance curves of the Franks/Gardner synchronizer. It is found that the Franks/Gardner performs consistently better than the Franks/Oerder synchronizer and significantly better in the cases of high SNRs and small noise bandwidths. The reason is the Oerder/Mehr synchronizer suffers from an additional noise component that is not present in the Franks/Gardner synchronizer. This noise component, which is pure self-noise, dominates at high SNRs.

6.2.3 Frequency-coherent detector for QPSK

The proposed circuit essentially builds a less noisy reference than that of conventional differential detection by resorting to the decisions taken on the previous received transmitted symbols, and use that noise-reduced reference to differentially detect the current symbol. The improvement over differential detection is that it outperforms differential detection by about 2 dB without significantly increasing the complexity nor lengthening the acquisition time to synchronize to the carrier.

In presence of a frequency offset the proposed circuit is more sensitive than the conventional differential detector. However performance gains remain greater than 1.7 dB for frequency offsets that are less than 1 degrees / symbol-interval and E_b/N_0

in the 14 to 20 dB range.

REFERENCES

[1] L. Franks, *Signal theory*. Prentice-Hall, 1969. Ch. 8 pp. 166-168.

[2] F. M. Gardner, "Interpolation in digital modems - part I: fundamentals," *IEEE trans. commun.*, vol. 41, pp. 501–507, March 1993.

[3] L. Erup, F. M. Gardner, and R. A. Harris, "Interpolation in digital modems - part II: implementation and performance," *IEEE trans. commun.*, vol. 41, pp. 998–1008, June 1993.

[4] Leon W. Couch II, *Digital and analog communication systems*. New Jersey, USA: Prentice-Hall, 5 ed., 1997. Ch. 6 pp.430-441.

[5] U. Mengali and A. N. D'Andrea, *Synchronization techniques for digital receivers*. Plenum Press, 1997. Ch3, Ch5, Ch8.

[6] M. Santarini, "Is FPGA a simpler puzzle for ASIC designers?," *EDN*, pp. 59–67, July 2007.

[7] S. H. Thomke, *Experimentation matters: unlocking the potential of new technologies for innovation*. Harvard Business School Press, 2003.

[8] "Data-over-cable service interface specifications - DOCSIS 3.0 Physical Layer Specification." CableLabs, Louisville, CO, Tech. Rep. CM-SP-PHYv3.0-I04-070518, May 2007.

[9] S. M. Kay, *Fundamentals of Statistical Signal Processing: Estimation Theory*. Prentice-Hall, 1993. Ch. 3 p. 35.

[10] S. M. Kay, *Fundamentals of Statistical Signal Processing: Estimation Theory*. Prentice-Hall, 1993. Ch. 7.

[11] H. Kobayashi, "Simultaneous adaptive estimation and decision algorithm for carrier modulated data transmission systems," *IEEE trans. commun.*, vol. COM-19, pp. 268–280, June 1971.

[12] H. Meyr, M. Oerder, and A. Polydoros, "On sampling rate, analog prefiltering, and sufficient statistics for digital receivers," *IEEE trans. commun.*, vol. 42, pp. 3208–3213, Dec. 1994.

[13] G. Ascheid, M. Oerder, J. Stahl, and H. Meyr, "An all digital receiver architecture for bandwidth efficient transmission at high data rates," *IEEE trans. commun.*, vol. 37, pp. 804–813, August 1989.

[14] P. Mallory, "A maximum likelihood bit synchronizer," *International Telemetering Conference, IV*, pp. 1–16, 1968.

[15] J. G. Proakis, *Digital Communications.* McGraw-Hill, 4 ed., 2000. Ch. 6 pp. 362-365.

[16] F. M. Gardner, "A BPSK/QPSK timing-error detector for sampled receivers," *IEEE trans. commun.*, vol. COM-34, pp. 423–429, May 1986.

[17] N. A. D'Andrea and M. Luise, "Design and analysis of a jitter-free clock recovery scheme for QAM systems," *IEEE trans. commun.*, vol. 41, pp. 1296–1299, Sept. 1993.

[18] M. Oerder and H. Meyr, "Digital filter and square timing recovery," *IEEE trans. commun.*, vol. 36, pp. 605–612, May 1988.

[19] S. J. Lee, "A new non-data-aided feedforward symbol timing estimator using two samples per symbol," *IEEE Commun. Lett.*, vol. 6, pp. 205–207, May 2002.

[20] U. Mengali and A. N. D'Andrea, *Synchronization techniques for digital receivers.* Plenum Press, 1997. Ch3. pp. 108-115.

[21] C. A. Eldering, N. Himayat, and F. M. Gardner, "CATV return path characterization for reliable communications," *IEEE Commun. Mag.*, vol. 33, pp. 62–69, Aug. 1995.

[22] E. R. Pelet, J. E. Salt, and D. Fast, "Timing and carrier acquisition in upstream CATV channels," *IEEE Ind. Elec. Conf.* Paris, France, Nov. 2006, pp. 3267-3272.

[23] M. Luise and R. Reggiannini, "Carrier frequency recovery in all-digital modems for burst-mode transmissions," *IEEE trans. commun.*, vol. 43, pp. 1169–1178, Feb. 1995.

[24] S. Kay, "A fast and accurate single frequency estimator," *IEEE trans. accoust. speech sig. proc.*, vol. 37, pp. 1987–1990, Dec. 1989.

[25] S. A. Tretter, "Estimating the frequency of a noisy sinusoid by linear regression," *IEEE trans. inform. theory*, vol. IT-31, pp. 832–835, Nov. 1985.

[26] M. P. Fitz and W. C. Lindsey, "Decision-directed burst-mode carrier synchronization techniques," *IEEE Trans. Commun.*, vol. 40, pp. 1644–1653, Oct. 1992.

[27] D. Divsalar and M. K. Simon, "Multiple-symbol differential detection of MPSK," *IEEE Trans. Commun.*, vol. 38, pp. 300–308, March 1990.

[28] B. Sklar, *Digital Communications - Fundamentals and Applications*. Prentice Hall, Oct. 2001. pp. 151.

[29] J. Wang and J. Speidel, "Packet acquisition in upstream transmission of the DOCSIS standard," *IEEE trans. broadcast.*, vol. 49, pp. 26–31, March 2003.

[30] F. M. Gardner, "Hangup in phase-lock loops," *IEEE trans. commun.*, vol. COM-25, pp. 1210–1214, Oct. 1977.

[31] Y.-C. Wu and E. Serpedin, "Unified analysis of a class of blind feedforward symbol timing estimators employing second-order statistics," *IEEE trans. wireless commun.*, vol. 5, pp. 737–742, April 2006.

[32] W.-P. Zhu, Y. Yan, M. O. Ahmad, and M. Swamy, "Feedforward symbol timing recovery technique using two samples per symbol," *IEEE trans. circuits and systems I*, vol. 52, pp. 2490–2500, Nov. 2005.

[33] K. Shi, Y. Wang, and E. Serpedin, "On the design of a digital blind feedforward, nearly jitter-free timing-recovery scheme for linear modulations," *IEEE trans. commun.*, vol. 52, pp. 1464–1469, Sept. 2004.

[34] Y. Wang, E. Serpedin, and P. Ciblat, "Blind feedforward cyclostationarity-based timing estimation for linear modulation," *IEEE trans. wireless commun.*, vol. 3, pp. 709–715, May 2004.

[35] L. Franks, *Signal theory*. New Jersey, USA: Prentice-Hall, 1969. Ch. 8.

[36] L. E. Franks, "Carrier and bit synchronization in data communication - a tutorial review," *IEEE trans. commun.*, vol. COM-28, pp. 1107–1121, August 1980.

[37] M. H. Meyers and L. E. Franks, "Joint carrier phase and symbol timing recovery for PAM systems," *IEEE trans. commun.*, vol. COM-28, pp. 1121–1129, August 1980.

[38] R. D. Gitlin and J. Salz, "Timing recovery in PAM systems," *The Bell System Technical Journal*, vol. 50, pp. 1645–1669, May-June 1971.

[39] Y. Wang, E. Serpedin, and P. Ciblat, "An alternative blind feedforward symbol timing estimator using two samples per symbol," *IEEE trans. commun.*, vol. 51, pp. 1451–1455, Sept. 2003.

[40] F. M. Gardner, "Self-noise in synchronizers," *IEEE trans. commun.*, vol. COM-28, pp. 1159–1163, August 1980.

[41] M. Moeneclaey, "Linear phase-locked loop theory for cyclostationary input disturbances," *IEEE trans. commun.*, vol. COM-30, pp. 2253–2259, Oct. 1982.

[42] T. T. Fang, "I and Q decomposition of self-noise in square-law clock regenerators," *IEEE trans. commun.*, vol. 36, pp. 1044–1052, sept. 1988.

[43] L. E. Franks and J. Bubrouski, "Statistical properties of timing jitter in a PAM timing recovery scheme," *IEEE trans. commun.*, vol. COM-22, pp. 913–920, July 1974.

[44] N. A. D'Andrea and U. Mengali, "Noise performance of two frequency-error detectors derived from maximum likelihood estimation methods," *IEEE trans. commun.*, vol. 42, pp. 793–801, April 1994.

[45] F. M. Gardner, "Properties of frequency difference detectors," *IEEE trans. commun.*, vol. COM-33, pp. 131–138, Feb. 1985.

[46] N. A. D'Andrea and U. Mengali, "Performance of a quadricorrelator driven by modulated signals," *IEEE trans. commun.*, vol. 38, pp. 1952–1957, Nov. 1990.

[47] N. A. D'Andrea and U. Mengali, "Design of quadricorrelators for automatic frequency control systems," *IEEE trans. commun.*, vol. 41, pp. 988–997, June 1993.

[48] M. P. Fitz, "Planar filtered techniques for burst mode carrier synchronization," *Conf. Rec. GLOBECOM'91*, pp. 365–369, 1991. Phoenix, Arizona, Dec 2-5.

[49] M. P. Fitz, "Further results in the flat estimation of a single frequency," *IEEE trans. commun.*, vol. 42, pp. 862–864, Feb. 1994.

[50] N. R. Sollenberger and J. C. I. Chuang, "Low-overhead symbol timing and carrier recovery for TDMA portable radio systems," *IEEE trans. commun.*, vol. 38, pp. 1886–1892, Oct. 1990.

[51] J. C. I. Chuang and N. R. Sollenberger, "Burst coherent demodulation with combined symbol timing, frequency offset estimation, and diversity selection," *IEEE trans. commun.*, vol. 39, pp. 1157–1164, July 1991.

[52] E. R. Pelet and J. E. Salt, "On economical timing-error detectors for QAM receivers," *IET Commun.*, vol. 1, pp. 618–622, August 2007.

[53] A. N. D'Andrea, U. Mengali, and R. Reggiannini, "The modified Cramer-Rao bound and its application to synchronization problems," *IEEE trans. commun.*, vol. 42, pp. 1391–1399, Feb. 1994.

[54] J. E. Salt, E. R. Pelet, and B. Berscheid, "Demodulator for cable TV video-on-demand," *IEEE Trans. Consum. Electron.*, vol. 53, pp. 1642–1646, Nov. 2007.

[55] H. Meyr, M. Moeneclaey, and S. A. Fechtel, *Digital communication receivers*. New York, USA: John Wiley & Sons, 1998. Ch. 2.

[56] Leon W. Couch II, *Digital and analog communication systems*. New Jersey, USA: Prentice-Hall, 5 ed., 1997. Ch. 2.

[57] P. Z. Peebles, *Probability, Random Variables, and Random Signal Principles*. McGraw-Hill, 3 ed., 1993. Ch. 7.

[58] M. H. Hayes, *Statistical Digital Signal Processing and Modeling*. John Wiley & Sons, 1996. Ch. 8.

[59] F. M. Gardner, *Phaselock techniques*. Wiley-Interscience, 2005.

[60] J. Distefano, A. Stubberud, and I. Williams, *Feedback and control systems*. Schaum's outline series - McGraw-Hill, 1990.

[61] A. V. Oppenheim, R. W. Schafer, and J. R. Buck, *Discrete-time signal processing*. Prentice Hall, 2 ed., 1999. Ch. 4.

[62] S. M. Kay, *Modern spectral estimation: theory and application*. Prentice-Hall, 1988. Ch. 4.

[63] J. G. Proakis, *Digital Communications*. McGraw-Hill, 4 ed., 2000. Ch. 9 pp. 560.

A.

The Modified Cramer-Rao Bound for timing offset

Let the signal $r(t)$ be defined as

$$r(t) = s(t; \varepsilon T) + w(t),\ 0 \leq t \leq T_0, \tag{A.1}$$

where $s(t, \varepsilon T)$ is the low-pass equivalent of a bandpass QAM signal, and $w(t)$ is the low-pass equivalent of Additive White Gaussian Noise (AWGN) with power spectral density constant, equal to $2N_0$ Watts / Hz.

The low-pass equivalent QAM signal is given by

$$s(t; \varepsilon T) = e^{j2\pi\mu t} \sum_{l=-\infty}^{+\infty} (d_I(l) + j d_Q(l)) g(t - lT - \varepsilon T), \tag{A.2}$$

where $g(t)$ is the square-root raised cosine pulse, T is the symbol interval, $d_I(l)+jd_Q(l)$ are the random transmitted QAM symbols whose components are independent and uniformly distributed over the alphabet, μ is an unknown frequency offset, and εT is an unknown timing offset. The timing offset is assumed to be uniformly distributed over $(-0.5T,\ 0.5T)$. The unknown parameter, μ, is ignored in the sequel since the frequency offset does not affect the estimation of εT as shown below. Only the timing offset and data are treated as unknown parameters.

The objective here is to derive a lower bound to the variance of any unbiased estimator of εT. The bound we use was originally derived by D'Andrea in [53] and named the Modified Cramer Rao Bound (MCRB). It is rederived here for the discrete-

time observed signal $r(t)$ after it has been bandlimited and sampled. The sampling frequency, $\frac{1}{T_s}$, is taken to be equal to $\frac{M}{T}$, where M is a positive integer with $M \geq 2$ so the sampling rate is at least equal to the Nyquist rate.

The white noise is bandlimited before sampling by filtering $r(t)$ with an ideal low-pass filter of bandwidth $1/(2T_s)$. The sampled signal is given by

$$x(nT_s) = s(nT_s; \varepsilon T) + w_f(nT_s), \tag{A.3}$$

where $w_f(t)$ is the complex bandlimited analog noise, and $w_f(nT_s)$ is a complex digital white noise with variance $2N_0/T_s$. Real and imaginary components of $w_f(nT_s)$ are independent with same variance, equal to N_0/T_s.

The MCRB for the timing offset is derived for the case where$M \times L$ samples of $x(nT_s)$ are observed to estimate εT, and L is a positive integer. LT represents the corresponding length of time the underlying continuous time signal, $x(t)$, is observed. The observed sequence is denoted by $x^T(nT_s)$, where

$$x^T(nT_s) = \begin{cases} s(nT_s; \varepsilon T) + w_f(nT_s), & 0 \leq n \leq ML-1 \\ 0, & \text{otherwise} \end{cases} \tag{A.4}$$

First an expression for the Cramer-Rao bound [9] of εT is derived assuming the transmitted symbols, $d_I(l) + jd_Q(l)$, are known. To differentiate this case from the case of interest (i.e. unknown transmitted symbols) the observed sequence is denoted by $x_d^T(nT_s)$, where the subscript, d, is used to indicate that the symbols are known.

As the complex Gaussian noise is white, then the complex Gaussian PDF of $\mathbf{x_d^T} = [x_d(0), x_d(T_s), \ldots, x_d((ML-1)T_s)]$ is

$$p(\mathbf{x_d^T}, \varepsilon T) = \frac{1}{(2\pi N_0/T_s)^{ML/2}} \exp\left\{ -\frac{1}{2N_0/T_s} \sum_{n=0}^{ML-1} |x_d(nT_s) - s_d(nT_s; \varepsilon T)|^2 \right\} \tag{A.5}$$

After evaluating the second derivative of $\ln p(\mathbf{x_d^T}, \varepsilon T)$ with respect to εT and taking the expectation of the derivative, $\dfrac{\partial^2 \ln p(\mathbf{x_d^T}, \varepsilon T)}{\partial^2 \varepsilon T}$, with respect to $p(\mathbf{x_d^T}, \varepsilon T)$, the Cramer-Rao bound is found to be

$$\mathrm{CRB}(\varepsilon \mathrm{T}) = \frac{\mathrm{N_0/T_s}}{\sum_{\mathrm{n=0}}^{\mathrm{ML-1}} \left| \dfrac{\partial \mathrm{s_d(nT_s;\varepsilon T)}}{\partial \varepsilon \mathrm{T}} \right|^2}, \quad \text{known symbols.} \tag{A.6}$$

When the symbols are unknown, the variance of the unbiased estimator, $\hat{\varepsilon T}$, becomes

$$\begin{aligned} \mathrm{Var}(\hat{\varepsilon \mathrm{T}}) &= E_{d,\varepsilon T} \left\{ \left(\hat{\varepsilon T} - \varepsilon T \right)^2 \right\} \\ &= E_d \left\{ E_{\varepsilon T|d} \left\{ \left(\hat{\varepsilon T} - \varepsilon T \right)^2 \right\} \right\}, \end{aligned} \tag{A.7}$$

where $E_{d,\varepsilon T}\{\cdot\}$ is the expectation taken over the symbols and the timing offset, $E_{\varepsilon T|d}\{\cdot\}$ is the expectation taken over the timing offset conditioned of knowing the symbols, and $E_d\{\cdot\}$ is the expectation taken over the symbols.

Since $E_{\varepsilon T|d} \left\{ \left(\hat{\varepsilon T} - \varepsilon T \right)^2 \right\} \geq \mathrm{CRB}(\varepsilon \mathrm{T})$ defined in (A.6) then from (A.7)

$$\mathrm{Var}(\hat{\varepsilon \mathrm{T}}) \geq \mathrm{E_d} \left\{ \frac{\mathrm{N_0/T_s}}{\sum_{\mathrm{n=0}}^{\mathrm{ML-1}} \left| \dfrac{\partial \mathrm{s(nT_s;\varepsilon T)}}{\partial \varepsilon \mathrm{T}} \right|^2} \right\} \tag{A.8}$$

and [53; Eq. (5)]

$$\mathrm{Var}(\hat{\varepsilon \mathrm{T}}) \geq \frac{\mathrm{N_0/T_s}}{\mathrm{E_d} \left\{ \sum_{\mathrm{n=0}}^{\mathrm{ML-1}} \left| \dfrac{\partial \mathrm{s(nT_s;\varepsilon T)}}{\partial \varepsilon \mathrm{T}} \right|^2 \right\}} \triangleq \mathrm{MCRB}(\varepsilon \mathrm{T}), \tag{A.9}$$

which is the Modified Cramer Rao Bound for the timing offset defined in [53].

Using (A.2)

$$\frac{\partial s(nT_s;\varepsilon T)}{\partial \varepsilon T} = e^{j2\pi\mu n T_s} \sum_{l=-\infty}^{+\infty} c(l) \frac{\partial g(nT_s - lT - \varepsilon T)}{\partial \varepsilon T}, \tag{A.10}$$

where $c(l) = (d_I(l) + jd_Q(l))$ and

$$E\{c(l)c^*(m)\} = \begin{cases} C_2, & l = m \\ 0, & \text{otherwise.} \end{cases} \tag{A.11}$$

Further,

$$g(t - lT - \varepsilon T) = \int_{-\infty}^{+\infty} G(f) e^{-j2\pi f(lT+\varepsilon T)} e^{j2\pi f t} df, \tag{A.12}$$

where $G(f)$ is the Fourier transform of $g(t)$, and

$$\frac{\partial g(nT_s - lT - \varepsilon T)}{\partial \varepsilon T} = \int_{-\infty}^{+\infty} -j2\pi f G(f) e^{-j2\pi f(lT+\varepsilon T)} e^{j2\pi f n T_s} df. \tag{A.13}$$

From (A.10) and (A.13),

$$\begin{aligned} E_d\left\{\left|\frac{\partial s(nT_s;\varepsilon T)}{\partial \varepsilon T}\right|^2\right\} = & \sum_{l_1=-\infty}^{+\infty}\sum_{l_2=-\infty}^{+\infty} E_d\{c(l_1)c^*(l_2)\} \\ & \times e^{j2\pi\mu n T_s}\left(\int_{-\infty}^{+\infty} -j2\pi f G(f) e^{-j2\pi f(l_1 T+\varepsilon T)} e^{j2\pi f n T_s} df\right) \\ & \times e^{-j2\pi\mu n T_s}\left(\int_{-\infty}^{+\infty} j2\pi\theta G^*(\theta) e^{j2\pi\theta(l_2 T+\varepsilon T)} e^{-j2\pi\theta n T_s} d\theta\right). \end{aligned} \tag{A.14}$$

Note that (A.14) does not depend on the frequency offset, μ, so the MCRB for timing offset is independent on the frequency offset. Now evaluating the expectation

using (A.11) yields

$$E_d\left\{\left|\frac{\partial s(nT_s;\varepsilon T)}{\partial \varepsilon T}\right|^2\right\} = 4\pi^2 C_2 \sum_{l=-\infty}^{+\infty}\int_{-\infty}^{+\infty}\int_{-\infty}^{+\infty} fG(f)\theta G^*(\theta) \times e^{j2\pi(lT+\varepsilon T)(\theta-f)} e^{j2\pi nT_s(f-\theta)} d\theta df. \tag{A.15}$$

Using $\sum_{l=-\infty}^{+\infty} e^{j2\pi lT(\theta-f)} = \frac{1}{T}\sum_{k=-\infty}^{+\infty}\delta(\theta - f - \frac{k}{T})$ by substituting $\sum_{l=-\infty}^{+\infty} e^{j2\pi lT(\theta-f)}$ by $(1/T)\sum_{k=-\infty}^{+\infty}\delta(\theta - f - \frac{k}{T})$ into (A.15) produces after simplification

$$E_d\left\{\left|\frac{\partial s(nT_s;\varepsilon T)}{\partial \varepsilon T}\right|^2\right\} = \frac{4\pi^2 C_2}{T}\sum_{k=-\infty}^{+\infty}\int_{-\infty}^{+\infty}(\theta-\frac{k}{T})G(\theta-\frac{k}{T})\theta G^*(\theta) \times e^{j2\pi\varepsilon T(k/T)} e^{j2\pi nT_s(k/T)} d\theta \tag{A.16}$$

Summing (A.16) over n gives

$$\sum_{n=0}^{ML-1} E_d\left\{\left|\frac{\partial s(nT_s;\varepsilon T)}{\partial \varepsilon T}\right|^2\right\} = \frac{4\pi^2 C_2}{T}\sum_{k=-\infty}^{+\infty}\int_{-\infty}^{+\infty}(\theta-\frac{k}{T})G(\theta-\frac{k}{T})\theta G^*(\theta) \times e^{j2\pi\varepsilon T(k/T)}\sum_{n=0}^{ML-1} e^{j2\pi nT_s(k/T)} d\theta \tag{A.17}$$

where since $\frac{1}{T_s} = \frac{M}{T}$,

$$\sum_{n=0}^{ML-1} e^{j2\pi nT_s(k/T)} = \begin{cases} ML, & k=0 \\ 0, & \text{otherwise,} \end{cases} \tag{A.18}$$

and (A.17) simplifies to

$$\sum_{n=0}^{ML-1} E_d\left\{\left|\frac{\partial s(nT_s;\varepsilon T)}{\partial \varepsilon T}\right|^2\right\} = \frac{4\pi^2 C_2}{T} ML\int_{-\infty}^{+\infty}\theta^2|G(\theta)|^2 d\theta. \tag{A.19}$$

Using $\frac{1}{T_s} = \frac{M}{T}$ yields

$$\mathrm{MCRB}(\varepsilon \mathrm{T}) = \frac{N_0/T_s}{\frac{4\pi^2 C_2}{T} ML \int_{-\infty}^{+\infty} \theta^2 |G(\theta)|^2 d\theta} \tag{A.20}$$

$$= \frac{N_0}{4\pi^2 C_2 L \int_{-\infty}^{+\infty} \theta^2 |G(\theta)|^2 d\theta}. \tag{A.21}$$

Note that the MCRB for timing offset does not depend on εT.

The Fourier transform, $G(f)$, of $g(t)$ has a square-root raised cosine shape so $|G(f)|^2$ has a raised cosine shape. From (B.1),

$$|G(f)|^2 = \begin{cases} T, & |f| < \frac{1-r}{2T} \\ \frac{T}{2}\left[1 + \cos\frac{\pi}{2r}\left(2|f|T + r - 1\right)\right], & \frac{1-r}{2T} < |f| < \frac{1+r}{2T} \\ 0, & |f| > \frac{1+r}{2T}, \end{cases} \tag{A.22}$$

so

$$\int_{-\infty}^{+\infty} \theta^2 |G(\theta)|^2 d\theta = \frac{1 + 3r^2 - 24(r/\pi)^2}{12T^2}. \tag{A.23}$$

Letting $\xi = \frac{1 + 3r^2 - 24(r/\pi)^2}{12}$ in (A.23) gives $\int_{-\infty}^{+\infty} \theta^2 |G(\theta)|^2 d\theta = \frac{\xi}{T^2}$ and (A.21) becomes

$$\mathrm{MCRB}(\varepsilon \mathrm{T}) = \frac{\mathrm{N_0} \times \mathrm{T}^2}{4\pi^2 \times \mathrm{C_2} \times \mathrm{L} \times \xi}. \tag{A.24}$$

Because $\int_{-\infty}^{+\infty} |G(f)|^2 df = 1$, the symbol energy in $s(t)$ is C_2. The symbol energy, E_s, in the bandpass QAM signal is then $C_2/2$ and (A.24) reduces to

$$\frac{1}{T^2}\mathrm{MCRB}(\varepsilon \mathrm{T}) = \frac{1}{8\pi^2 \times \mathrm{L} \times \xi \times \mathrm{E_s/N_0}}. \tag{A.25}$$

This derivation produces D'Andrea's equation. This is no surprise since the sampling meets the Nyquist rate and thus no information is lost during the sampling operation.

B.

Discrete time Fourier transform of a raised cosine impulse response sampled at the symbol rate

For a raised cosine pulse, $h(t)$, with Fourier transform denoted by $H_A(j\Omega)$, The Fourier transform of $h(t+\varepsilon T)$ is given by [63]

$$H_A(j\Omega;\varepsilon T) = H_A(j\Omega)e^{j\Omega\varepsilon T} \tag{B.1}$$
$$= \begin{cases} Te^{j\Omega\varepsilon T}, & |\Omega T| \le (1-r)\pi, \\ \dfrac{T}{2}\left[1+\cos\left(\dfrac{\pi}{2r}\left(\dfrac{|\Omega T|}{\pi}+r-1\right)\right)\right]e^{j\Omega\varepsilon T}, & (1-r)\pi \le |\Omega T| \le (1+r)\pi, \\ 0, & (1+r)\pi \le |\Omega T| < \infty. \end{cases}$$

where r is the roll off factor ($0 < r < 1$). The Nyquist frequency of $H_A(j\Omega;\varepsilon T)$ is $(r+1)/2T$. Since r is greater than zero, the symbol rate, $1/T$, is less than twice the Nyquist rate, so sampling $h(t+\varepsilon T)$ at the symbol rate causes aliasing in the frequency domain. The DTFT of $h((k+\varepsilon)T)$ can be defined for any 2π interval of ω, where $\omega = \Omega T$. For $-(1-r)\pi < \omega \le (1+r)\pi$

$$H(e^{j\omega};\varepsilon T) = \frac{1}{T}\sum_{k=-\infty}^{+\infty} H_A(j(\frac{\omega-2\pi k}{T});\varepsilon T), \quad -(1-r)\pi < \omega \le (1+r)\pi.$$

Since $H_A(j\Omega;\varepsilon T)$ is band-limited to $|\Omega| < 2\pi/T$, then

$$H(e^{j\omega};\varepsilon T) = \frac{1}{T}\Big(H_A(e^{j\frac{\omega}{T}};\varepsilon T) + H_A(e^{j(\frac{\omega-2\pi}{T})};\varepsilon T)\Big), \quad -(1-r)\pi < \omega \le (1+r)\pi. \tag{B.2}$$

From (B.1) $(1/T)H_A(e^{j\frac{\omega}{T}};\varepsilon T)$ and $(1/T)H_A(e^{j(\frac{\omega-2\pi}{T})};\varepsilon T)$ are

$$\begin{aligned}
\frac{1}{T}H_A(e^{j\frac{\omega}{T}};\varepsilon T) &= \begin{cases} e^{j\omega\frac{\varepsilon T}{T}}, & |\omega| \le (1-r)\pi, \\ \frac{1}{2}\left[1+\cos\left(\frac{\pi}{2r}\left(\frac{\omega}{\pi}+r-1\right)\right)\right]e^{j\omega\frac{\varepsilon T}{T}}, & (1-r)\pi \le \omega \le (1+r)\pi, \end{cases} \\
\frac{1}{T}H_A(e^{j(\frac{\omega-2\pi}{T})};\varepsilon T) &= \left\{\frac{1}{2}\left[1+\cos\left(\frac{\pi}{2r}\left(\frac{\omega}{\pi}-r-1\right)\right)\right]e^{j(\omega-2\pi)\frac{\varepsilon T}{T}}, \quad (1-r)\pi \le \omega \le (1+r)\pi, \right.
\end{aligned} \tag{B.3}$$

over the interval $[-(1-r)\pi, (1+r)\pi]$.

The functions $H_A(e^{j\frac{\omega}{T}};\varepsilon T)$ and $H_A(e^{j(\frac{\omega-2\pi}{T})};\varepsilon T)$ overlap in the region $((1-r)\pi, (1+r)\pi)$. Using (B.2), (B.3) and the trigonometric identity $\cos(a \pm b) = \cos(a)\cos(b) \mp \sin(a)\sin(b)$ with $a = \frac{\pi}{2r}(\frac{\omega}{\pi} - 1)$ and $b = \frac{\pi}{2r}r = \frac{\pi}{2}$ yields

$$H(e^{j\omega};\varepsilon T) = \begin{cases} e^{j\omega\frac{\varepsilon T}{T}}, & |\omega| \le (1-r)\pi, \\ \dfrac{e^{j\omega\frac{\varepsilon T}{T}}}{2}\left(1-\sin\dfrac{\omega-\pi}{2r}+e^{-j2\pi\frac{\varepsilon T}{T}}\right. & \\ \left.+\, e^{-j2\pi\frac{\varepsilon T}{T}}\sin\dfrac{\omega-\pi}{2r}\right), & (1-r)\pi < \omega \le (1+r)\pi. \end{cases}$$

Using trigonometric identities, $e^{j\pi\frac{\varepsilon T}{T}} + e^{-j\pi\frac{\varepsilon T}{T}} = 2\cos(\pi\frac{\varepsilon T}{T})$ and $e^{j\pi\frac{\varepsilon T}{T}} - e^{-j\pi\frac{\varepsilon T}{T}} = 2j\sin(\pi\frac{\varepsilon T}{T})$, the discrete-time Fourier Transform of $h((k+\varepsilon)T)$ can be written

$$H(e^{j\omega};\varepsilon T) = \begin{cases} e^{j\omega\frac{\varepsilon T}{T}}, & -(1-r)\pi < \omega \le (1-r)\pi, \\ e^{j(\omega-\pi)\frac{\varepsilon T}{T}}\left[\cos(\pi\dfrac{\varepsilon T}{T})\right. & \\ \left.-j\sin(\pi\dfrac{\varepsilon T}{T})\sin(\dfrac{\pi}{2r}(\dfrac{\omega}{\pi}-1))\right], & (1-r)\pi \le \omega \le (1+r)\pi. \end{cases} \tag{B.4}$$

C.

Self-noise power spectrum expression for early-late detector

From (2.16) the discrete-time Fourier transform (DTFT) of $y_{sn}(kT)$ is the sum of the discrete-time Fourier Transform of four terms, each of which is the square of a sequence. Squaring in the discrete-time domain corresponds to circular convolution in the frequency domain. The DTFT of $x_I^2((k+\frac{m}{M})T)$ is

$$\frac{1}{2\pi}\int_{-\pi}^{\pi} X_I(e^{j\theta};\frac{m}{M}T)X_I(e^{j(\omega-\theta)};\frac{m}{M}T)d\theta, \tag{C.1}$$

where $X_I(e^{j\omega};\frac{m}{M}T)$ is the DTFT of $x_I((k+\frac{m}{M})T)$. The DTFT of $x_I((k+\frac{m}{M})T)$ is given by

$$\sum_{i=-N}^{+N} d_I(i)e^{-j\omega i}H(e^{j\omega};\frac{m}{M}T) \tag{C.2}$$

and the DTFT of $x_I^2((k+\frac{m}{M})T)$ by (after using the circular convolution)

$$\frac{1}{2\pi}\int_{-\pi}^{\pi}\sum_{i=-N}^{+N}\sum_{k=-N}^{+N} d_I(i)d_I(k)e^{-j\theta i}e^{-j(\omega-\theta)k}H(e^{j\theta};\frac{m}{M}T)H(e^{j(\omega-\theta)};\frac{m}{M}T)d\theta. \tag{C.3}$$

The DTFT, $Y_{sn}(e^{j\omega})$, is the sum of four terms like in (C.3). The square of the magnitude is given by $|Y_{sn}(e^{j\omega})|^2 = Y_{sn}(e^{j\omega}) \times Y_{sn}^*(e^{j\omega})$ and the power spectrum by

$S_{sn}(e^{j\omega})$

$$= \lim_{N\to\infty} \frac{1}{2N+1}\frac{1}{4\pi^2} E\left\{ \left(\int_{-\pi}^{\pi} \sum_{i=-N}^{+N} \sum_{k=-N}^{+N} [d_I(i)d_I(k) + d_Q(i)d_Q(k)] e^{-j\theta i} e^{-j(\omega-\theta)k} \right.\right.$$
$$\times \left[H(e^{j\theta}; \frac{m}{M}T) H(e^{j(\omega-\theta)}; \frac{m}{M}T) - H(e^{j\theta}; -\frac{m}{M}T) H(e^{j(\omega-\theta)}; -\frac{m}{M}T) \right] d\theta \Big)$$
$$\times \left(\int_{-\pi}^{\pi} \sum_{i=-N}^{+N} \sum_{k=-N}^{+N} [d_I(i)d_I(k) + d_Q(i)d_Q(k)] e^{-j\theta i} e^{-j(\omega-\theta)k} \right.$$
$$\left.\left. \times \left[H(e^{j\theta}; \frac{m}{M}T) H(e^{j(\omega-\theta)}; \frac{m}{M}T) - H(e^{j\theta}; -\frac{m}{M}T) H(e^{j(\omega-\theta)}; -\frac{m}{M}T) \right] d\theta \right)^* \right\}$$

$$= \lim_{N\to\infty} \frac{1}{2N+1}\frac{1}{4\pi^2} \times \int_{\theta_1=-\pi}^{\pi} \int_{\theta_2=-\pi}^{\pi} \sum_{m=-N}^{+N} \sum_{l=-N}^{+N} \sum_{i=-N}^{+N} \sum_{k=-N}^{+N} E\left\{ [d_I(i)d_I(k) + d_Q(i)d_Q(k)] \right.$$
$$\left. \times [d_I(m)d_I(l) + d_Q(m)d_Q(l)] \right\} e^{-j\theta_1 i} e^{-j(\omega-\theta_1)k} e^{j\theta_2 m} e^{j(\omega-\theta_2)l}$$
$$\times [U_+(\theta_1,\omega) - U_-(\theta_1,\omega)] [U_+(\theta_2,\omega) - U_-(\theta_2,\omega)]^* d\theta_1 d\theta_2 \qquad (C.4)$$

where $U_+(\theta,\omega) = H(e^{j\theta}; +\frac{m}{M}T) H(e^{j(\omega-\theta)}; +\frac{m}{M}T)$ and $U_-(\theta,\omega) = H(e^{j\theta}; -\frac{m}{M}T)$ $H(e^{j(\omega-\theta)}; -\frac{m}{M}T)$. Since the symbols, $d_I(i)$ and $d_Q(i)$, have same statistical properties and are independent, the expectation term in (B.4) can be reduced to

$$2E\{d_I(i)d_I(k)d_I(m)d_I(l)\} + 2E\{d_I(i)d_I(k)\}E\{d_Q(m)d_Q(l)\}. \qquad (C.5)$$

The quadruple sum of the first term in (C.5) evaluates to

$$
\begin{aligned}
&2\sum_{m=-N}^{+N}\sum_{l=-N}^{+N}\sum_{i=-N}^{+N}\sum_{k=-N}^{+N} E\{d_I(i)d_I(k)d_I(m)d_I(l)\} \\
&= 2\sum_{i=-N}^{+N} E\{d_I^4(i)\} + 2\sum_{l=-N}^{+N}\sum_{\substack{i=-N \\ (i\neq l)}}^{+N} \sigma_d^4 \\
&+ 2\sum_{k=-N}^{+N}\sum_{\substack{i=-N \\ (i\neq k)}}^{+N} \sigma_d^4 + 2\sum_{m=-N}^{+N}\sum_{\substack{i=-N \\ (i\neq m)}}^{+N} \sigma_d^4 \\
&= 2\sum_{i=-N}^{+N} (E\{d_I^4(i)\} - 3\sigma_d^4) + 2\sum_{l=-N}^{+N}\sum_{i=-N}^{+N} \sigma_d^4 \\
&+ 2\sum_{k=-N}^{+N}\sum_{i=-N}^{+N} \sigma_d^4 + 2\sum_{m=-N}^{+N}\sum_{i=-N}^{+N} \sigma_d^4
\end{aligned} \tag{C.6}
$$

and the quadruple sum of the second term in (C.5) becomes

$$
\sum_{m=-N}^{+N}\sum_{l=-N}^{+N}\sum_{i=-N}^{+N}\sum_{k=-N}^{+N} E\{d_I(i)d_I(k)\}E\{d_Q(m)d_Q(l)\} = 2\sum_{m=l=-N}^{+N} \sigma_d^4 \sum_{i=k=-N}^{+N} \sigma_d^4. \tag{C.7}
$$

Equation (2.18) is obtained after inserting (C.6) and (C.7) into (B.4) and solving each of the terms obtained separately.

The terms are solved by noticing that the double sum, $\sum_{l=m=-N}^{+N}\sum_{i=k=-N}^{+N} e^{-j\omega i}e^{j\omega l}$, is equal to $(\sum_{i=-N}^{N} e^{-j\omega i})^2$, where $\sum_{i=-N}^{N} e^{-j\omega i} = \frac{e^{j\omega N}-e^{-j\omega(N+1)}}{1-e^{-j\omega}} = \frac{\sin(\omega(N+\frac{1}{2}))}{\sin(\frac{\omega}{2})}$ and the limit, $\lim_{N\to\infty} \frac{1}{2N+1}\,(\frac{\sin(\omega(N+\frac{1}{2}))}{\sin(\frac{\omega}{2})})^2 = 2\pi\delta(\omega)$.

Using powers of natural numbers, one can show that $2(E\{d_I^4(i)\}-3\sigma_d^4) = -\frac{12(A+1)}{5(A-1)}\times \sigma_d^4$, where A is the modulation order.

D.

Closed-form power spectrum expression for early-late detector enhanced with ideal high-pass filters

In this appendix a closed-form expression for Equation (2.18) in Section 2.5 is analytically derived. This equation, which is re-labeled Equation (D.1) in this appendix, is given by

$$S_{sn}(e^{j\omega}) = \sigma_d^4 \left\{ \frac{2}{\pi} \int_{-\pi}^{\pi} \left[U_+(\theta,\omega) - U_-(\theta,\omega)\right] \left[U_+(\theta,\omega) - U_-(\theta,\omega)\right]^* d\theta \right. \\ \left. - \frac{12(A+1)}{5(A-1)} \left| H_+(e^{j\omega}) \otimes H_+(e^{j\omega}) - H_-(e^{j\omega}) \otimes H_-(e^{j\omega}) \right|^2 \right\}, \qquad \text{(D.1)}$$

where $\otimes$ denotes the convolution operation, the star, *, denotes the conjugate and $U_+(\theta,\omega) = H(e^{j\theta}; +\frac{m}{M}T)H(e^{j(\omega-\theta)}; +\frac{m}{M}T)$, $U_-(\theta,\omega) = H(e^{j\theta}; -\frac{m}{M}T)H(e^{j(\omega-\theta)}; -\frac{m}{M}T)$, $H_+(e^{j\omega}) = H(e^{j\omega}; +\frac{m}{M}T)$ and $H_-(e^{j\omega}) = H(e^{j\omega}; -\frac{m}{M}T)$, and A is the modulation order (i.e. $A = 64$ for 64-QAM).

Equation (B.4) of Appendix B is used here. This equation, which is re-labeled Equation (D.2) in this appendix, is given by

$$H(e^{j\omega}; \varepsilon T) = \begin{cases} e^{j\omega\varepsilon}, & -(1-r)\pi < \omega \le (1-r)\pi, \\ e^{j(\omega-\pi)\varepsilon} \left[\cos(\pi\varepsilon) - j\sin(\pi\varepsilon)\sin(\frac{\pi}{2r}(\frac{\omega}{\pi} - 1))\right], & (1-r)\pi \le \omega \le (1+r)\pi. \end{cases} \qquad \text{(D.2)}$$

A closed-form expression for (D.1) is obtained as follows: a closed-form expression

for the integral on the right hand side of (D.1) is developed in Section D.1 and a closed-form expression for the magnitude squared in the second term on the right hand side of (D.1) is developed in Section D.2.

D.1

The $\frac{2}{\pi}$ times the integral on the right hand side of (D.1), when expressed in terms of $H(e^{j\omega}; \pm\frac{m}{M}T)$, is equal to

$$\frac{2}{\pi}\int_{-\pi}^{\pi}\Big[H(e^{j\theta};\frac{m}{M}T)H(e^{j(\omega-\theta)};\frac{m}{M}T)-H(e^{j\theta};-\frac{m}{M}T)H(e^{j(\omega-\theta)};-\frac{m}{M}T)\Big]$$
$$\times\Big[H^*(e^{j\theta};\frac{m}{M}T)H^*(e^{j(\omega-\theta)};\frac{m}{M}T)-H^*(e^{j\theta};-\frac{m}{M}T)H^*(e^{j(\omega-\theta)};-\frac{m}{M}T)\Big]\,d\theta. \quad \text{(D.3)}$$

Equation (D.3) is equal to 0 for $|\omega| > 2r\pi$, since when an ideal high-pass filter is used this equation can be viewed as a sum of convolutions of $H(e^{j\omega};\varepsilon T)$ and $H(e^{j\omega};\varepsilon T)$ with $\varepsilon = \pm\frac{m}{M}$ for $(1-r)\pi < |\omega| < \pi$. It is sufficient to solve (D.3) for $0 \le \omega \le 2r\pi$ because (D.3) is an even function of ω.

For $0 \le \omega \le 2r\pi$ and $r \le 0.5$ the interval of integration reduces to $((1-r)\pi + \omega, (1+r)\pi)$ and (D.3) is equal to

$$\frac{2}{\pi}\int_{(1-r)\pi+\omega}^{(1+r)\pi}\Big[H(e^{j\theta};\frac{m}{M}T)H(e^{j(\omega-\theta)};\frac{m}{M}T)-H(e^{j\theta};-\frac{m}{M}T)H(e^{j(\omega-\theta)};-\frac{m}{M}T)\Big]$$
$$\times\Big[H^*(e^{j\theta};\frac{m}{M}T)H^*(e^{j(\omega-\theta)};\frac{m}{M}T)-H^*(e^{j\theta};-\frac{m}{M}T)H^*(e^{j(\omega-\theta)};-\frac{m}{M}T)\Big]$$
$$=\frac{4}{\pi}\int_{(1-r)\pi+\omega}^{(1+r)\pi}|H(e^{j\theta};\frac{m}{M}T)|^2|H(e^{j(\omega-\theta)};\frac{m}{M}T)|^2d\theta$$
$$-\frac{2}{\pi}\int_{(1-r)\pi+\omega}^{(1+r)\pi}\Big[(H(e^{j\theta};\frac{m}{M}T))^2(H(e^{j(\omega-\theta)};\frac{m}{M}T))^2+(H(e^{j\theta};-\frac{m}{M}T))^2(H(e^{j(\omega-\theta)};-\frac{m}{M}T))^2\Big]\,d\theta \quad \text{(D.4)}$$

since from (D.2), $|H(e^{j\omega};-\frac{m}{M}T)|^2 = |H(e^{j\omega};\frac{m}{M}T)|^2$ and $H^*(e^{j\omega};\mp\frac{m}{M}T) = H(e^{j\omega};\pm\frac{m}{M}T)$.

A closed-form expression for (D.4) is obtained as follows. Noticing that $(1-r)\pi < \theta < (1+r)\pi$ over the interval of integration and $-(1+r)\pi < \omega-\theta < -(1-r)\pi$ over

the interval of integration, then $|H(e^{j\theta};\frac{m}{M}T)|^2|H(e^{j(\omega-\theta)};\frac{m}{M}T)|^2$ is equal to

$$\begin{aligned}
&\left[\cos^2(\pi\frac{m}{M})+\sin^2(\pi\frac{m}{M})\sin^2(\frac{\pi}{2r}(\frac{\theta}{\pi}-1))\right]\left[\cos^2(\pi\frac{m}{M})+\sin^2(\pi\frac{m}{M})\sin^2(\frac{\pi}{2r}(\frac{\omega-\theta}{\pi}+1))\right]\\
&=\cos^4(\pi\frac{m}{M})+\cos^2(\pi\frac{m}{M})\sin^2(\pi\frac{m}{M})\sin^2(\frac{\pi}{2r}(\frac{\theta}{\pi}-1))\\
&+\cos^2(\pi\frac{m}{M})\sin^2(\pi\frac{m}{M})\sin^2(\frac{\pi}{2r}(\frac{\omega-\theta}{\pi}+1))\\
&+\sin^4(\pi\frac{m}{M})\sin^2(\frac{\pi}{2r}(\frac{\theta}{\pi}-1))\sin^2(\frac{\pi}{2r}(\frac{\omega-\theta}{\pi}+1))
\end{aligned}\tag{D.5}$$

To obtain (D.5) it can be shown that for $-(1+r)\pi<\omega<-(1-r)\pi$,
$H(e^{j\omega};\varepsilon T)=e^{j(\omega+\pi)\varepsilon}\left[\cos(\pi\varepsilon)-j\sin(\pi\varepsilon)\sin(\frac{\pi}{2r}(\frac{\omega}{\pi}+1))\right]$.

Using the trigonometric identities, $\sin^2(a)=\frac{1}{2}-\frac{1}{2}\cos(2a)$ and $\cos(a)\cos(b)=\frac{1}{2}(\cos(a+b)+\cos(a-b))$, (D.5) can be reduced to

$$\begin{aligned}
&\cos^4(\pi\frac{m}{M})+\frac{1}{2}\cos^2(\pi\frac{m}{M})\sin^2(\pi\frac{m}{M})\left[1-\cos(\frac{\pi}{r}(\frac{\theta}{\pi}-1))\right]\\
&+\frac{1}{2}\cos^2(\pi\frac{m}{M})\sin^2(\pi\frac{m}{M})\left[1-\cos(\frac{\pi}{r}(\frac{\omega-\theta}{\pi}+1))\right]\\
&+\frac{1}{4}\sin^4(\pi\frac{m}{M})\left[1-\cos(\frac{\pi}{r}(\frac{\theta}{\pi}-1))-\cos(\frac{\pi}{r}(\frac{\omega-\theta}{\pi}+1))+\frac{1}{2}\cos(\frac{\omega}{r})+\frac{1}{2}\cos(\frac{\pi}{r}(\frac{\omega-2\theta}{\pi}+2))\right]
\end{aligned}\tag{D.6}$$

Equation (D.6) is an expression for $|H(e^{j\theta};\frac{m}{M}T)|^2|H(e^{j(\omega-\theta)};\frac{m}{M}T)|^2$. A closed form expression for $\frac{4}{\pi}\int_{(1-r)\pi+\omega}^{(1+r)\pi}|H(e^{j\theta};\frac{m}{M}T)|^2|H(e^{j(\omega-\theta)};\frac{m}{M}T)|^2d\theta$ is then equal to

$$\begin{aligned}
&\frac{4}{\pi}\Big\{\cos^4(\pi\frac{m}{M})\left[2r\pi-\omega\right]+\cos^2(\pi\frac{m}{M})\sin^2(\pi\frac{m}{M})\left[2r\pi-\omega\right]-r\cos^2(\pi\frac{m}{M})\sin^2(\pi\frac{m}{M})\sin(\frac{\omega}{r})\\
&+\frac{1}{4}\sin^4(\pi\frac{m}{M})\left[2r\pi-\omega-2r\sin(\frac{\omega}{r})+\frac{1}{2}\cos(\frac{\omega}{r})(2r\pi-\omega)-\frac{r}{2}\sin(\frac{\omega}{r})\right]\Big\}.
\end{aligned}\tag{D.7}$$

Intermediate calculations to derive (D.7) from (D.6) can be found in Section D.3, equations (D.24). Applying $\cos^2(\pi\frac{m}{M})\sin^2(\pi\frac{m}{M})=\cos^2(\pi\frac{m}{M})(1-\cos^2(\pi\frac{m}{M}))$ to replace the first and second term in (D.7) with $\cos^4(\pi\frac{m}{M})\left[2r\pi-\omega\right]$ and after rearranging the

terms, (D.7) can be written as

$$\frac{r}{\pi}\left\{\left[p_1(\frac{m}{M})+p_2(\frac{m}{M})\cos(\frac{\omega}{r})\right]\left[2\pi-\frac{\omega}{r}\right]-p_5(\frac{m}{M})\sin(\frac{\omega}{r})\right\}, \tag{D.8}$$

where

$$\begin{aligned}
p_1(\frac{m}{M}) &= 4\cos^2(\pi\frac{m}{M})+\sin^4(\pi\frac{m}{M})=\cos^4(\pi\frac{m}{M})+2\cos^2(\pi\frac{m}{M})+1\\
p_2(\frac{m}{M}) &= \frac{1}{2}\sin^4(\pi\frac{m}{M})=\frac{1}{2}\cos^4(\pi\frac{m}{M})-\cos^2(\pi\frac{m}{M})+\frac{1}{2}\\
p_5(\frac{m}{M}) &= \frac{5}{2}\sin^4(\pi\frac{m}{M})+4\cos^2(\pi\frac{m}{M})\sin^2(\pi\frac{m}{M})=-\frac{3}{2}\cos^4(\pi\frac{m}{M})-\cos^2(\pi\frac{m}{M})+\frac{5}{2}.
\end{aligned}$$

It remains to solve the second term in (D.4). From (D.2) one can show that

$$(H(e^{j\theta};-\frac{m}{M}T))^2(H(e^{j(\omega-\theta)};-\frac{m}{M}T))^2=(H^*(e^{j\theta};\frac{m}{M}T))^2(H^*(e^{j(\omega-\theta)};\frac{m}{M}T))^2$$

and therefore

$$\begin{aligned}
&(H(e^{j\theta};\frac{m}{M}T))^2(H(e^{j(\omega-\theta)};\frac{m}{M}T))^2+(H(e^{j\theta};-\frac{m}{M}T))^2(H(e^{j(\omega-\theta)};-\frac{m}{M}T))^2\\
&=2\text{Real}\left\{(H(e^{j\theta};\frac{m}{M}T))^2(H(e^{j(\omega-\theta)};\frac{m}{M}T))^2\right\},
\end{aligned} \tag{D.9}$$

where Real denotes the real part of a complex. From (D.2) with $(1-r)\pi<\theta<(1+r)\pi$ and $-(1+r)\pi<\omega-\theta<-(1-r)\pi$, $(H(e^{j\theta};\frac{m}{M}T))^2(H(e^{j(\omega-\theta)};\frac{m}{M}T))^2$ is equal to

$$\begin{aligned}
&e^{2j\omega\frac{m}{M}}\left[\cos(\pi\frac{m}{M})-j\sin(\pi\frac{m}{M})\sin(\frac{\pi}{2r}(\frac{\theta}{\pi}-1))\right]^2\\
&\times\left[\cos(\pi\frac{m}{M})-j\sin(\pi\frac{m}{M})\sin(\frac{\pi}{2r}(\frac{(\omega-\theta)}{\pi}+1))\right]^2\\
&=e^{2j\omega\frac{m}{M}}\left[\cos^2(\pi\frac{m}{M})-2j\cos(\pi\frac{m}{M})\sin(\pi\frac{m}{M})f_1(\theta;r)-\sin^2(\pi\frac{m}{M})f_1^2(\theta;r)\right]\\
&\times\left[\cos^2(\pi\frac{m}{M})-2j\cos(\pi\frac{m}{M})\sin(\pi\frac{m}{M})f_2(\omega-\theta;r)-\sin^2(\pi\frac{m}{M})f_2^2(\omega-\theta;r)\right],
\end{aligned} \tag{D.10}$$

where $f_1(\theta;r)$ denotes $\sin(\frac{\pi}{2r}(\frac{\theta}{\pi}-1))$ and $f_2(\omega-\theta;r)$ denotes $\sin(\frac{\pi}{2r}(\frac{\omega-\theta}{\pi}+1))$. Equa-

tion (D.10) can be written as $e^{2j\omega\frac{m}{M}}[C_1(\frac{m}{M};\theta,\omega,r)+jC_2(\frac{m}{M};\theta,\omega,r)]$, where

$$\begin{aligned}
C_1(\frac{m}{M};\theta,\omega,r) &= \cos^4(\pi\frac{m}{M}) - \cos^2(\pi\frac{m}{M})\sin^2(\pi\frac{m}{M})f_2^2(\omega-\theta;r) \\
&\quad - 4\cos^2(\pi\frac{m}{M})\sin^2(\pi\frac{m}{M})f_1(\theta;r)f_2(\omega-\theta;r) - \cos^2(\pi\frac{m}{M})\sin^2(\pi\frac{m}{M})f_1^2(\theta;r) \\
&\quad + \sin^4(\pi\frac{m}{M})f_1^2(\theta;r)f_2^2(\omega-\theta;r) \\
&= \cos^4(\pi\frac{m}{M}) + \sin^4(\pi\frac{m}{M})f_1^2(\theta;r)f_2^2(\omega-\theta;r) \\
&\quad - \cos^2(\pi\frac{m}{M})\sin^2(\pi\frac{m}{M})\left[f_1^2(\theta;r)+4f_1(\theta;r)f_2(\omega-\theta;r)+f_2^2(\omega-\theta;r)\right]
\end{aligned} \tag{D.11}$$

and

$$\begin{aligned}
C_2(\frac{m}{M};\theta,\omega,r) &= -2\cos^3(\pi\frac{m}{M})\sin(\pi\frac{m}{M})f_1(\theta;r) + 2\cos(\pi\frac{m}{M})\sin^3(\pi\frac{m}{M})f_1(\theta;r)f_2^2(\omega-\theta;r) \\
&\quad - 2\cos^3(\pi\frac{m}{M})\sin(\pi\frac{m}{M})f_2(\omega-\theta;r) + 2\cos(\pi\frac{m}{M})\sin^3(\pi\frac{m}{M})f_1^2(\theta;r)f_2(\omega-\theta;r) \\
&= -2\cos^3(\pi\frac{m}{M})\sin(\pi\frac{m}{M})\left[f_1(\theta;r)+f_2(\omega-\theta;r)\right] \\
&\quad + 2\cos(\pi\frac{m}{M})\sin^3(\pi\frac{m}{M})\left[f_1(\theta;r)f_2^2(\omega-\theta;r)+f_1^2(\theta;r)f_2(\omega-\theta;r)\right].
\end{aligned} \tag{D.12}$$

Using this decomposition (D.9) can be rewritten as

$$\begin{aligned}
&(H(e^{j\theta};\frac{m}{M}T))^2(H(e^{j(\omega-\theta)};\frac{m}{M}T))^2 + (H(e^{j\theta};-\frac{m}{M}T))^2(H(e^{j(\omega-\theta)};-\frac{m}{M}T))^2 \\
&= 2\cos(2\omega\frac{m}{M})C_1(\frac{m}{M};\theta,\omega,r) - 2\sin(2\omega\frac{m}{M})C_2(\frac{m}{M};\theta,\omega,r).
\end{aligned} \tag{D.13}$$

This implies that

$$\begin{aligned}
&-\frac{2}{\pi}\int_{(1-r)\pi+\omega}^{(1+r)\pi}\left[(H(e^{j\theta};\frac{m}{M}T))^2(H(e^{j(\omega-\theta)};\frac{m}{M}T))^2 + (H(e^{j\theta};-\frac{m}{M}T))^2(H(e^{j(\omega-\theta)};-\frac{m}{M}T))^2\right]d\theta \\
&= -\frac{4}{\pi}\cos(2\omega\frac{m}{M})\int_{(1-r)\pi+\omega}^{(1+r)\pi}C_1(\frac{m}{M};\theta,\omega,r)d\theta + \frac{4}{\pi}\sin(2\omega\frac{m}{M})\int_{(1-r)\pi+\omega}^{(1+r)\pi}C_2(\frac{m}{M};\theta,\omega,r)d\theta.
\end{aligned} \tag{D.14}$$

It remains to solve (D.14) to obtain a closed-form expression for (D.4).

From (D.11) a closed-form expression for the first term in (D.14) is equal to

$$
\begin{aligned}
&-\frac{4}{\pi}\cos(2\omega\frac{m}{M})\left\{\cos^4(\pi\frac{m}{M})\left[2r\pi-\omega\right]+\frac{1}{4}\sin^4(\pi\frac{m}{M})\left[2r\pi-\omega\right]\left[1+\frac{1}{2}\cos(\frac{\omega}{r})\right]\right.\\
&-\sin^4(\pi\frac{m}{M})\frac{5r}{8}\sin(\frac{\omega}{r})\\
&\left.-\cos^2(\pi\frac{m}{M})\sin^2(\pi\frac{m}{M})\left[2r\pi-\omega-r\sin(\frac{\omega}{r})+4r\sin(\frac{\omega}{2r})-2\cos(\frac{\omega}{2r})(2r\pi-\omega)\right]\right\}.
\end{aligned}
\tag{D.15}
$$

Intermediate calculations can be found in Section D.3, equations (D.25). Applying $\cos^2(\pi\frac{m}{M})\sin^2(\pi\frac{m}{M})=\cos^2(\pi\frac{m}{M})(1-\cos^2(\pi\frac{m}{M}))$ to replace $[\cos^4(\pi\frac{m}{M})-\cos^2(\pi\frac{m}{M})\sin^2(\pi\frac{m}{M})[2r\pi-\omega]$ with $[2\cos^4(\pi\frac{m}{M})-\cos^2(\pi\frac{m}{M})][2r\pi-\omega]$ and after rearranging the terms, (D.15) can be written as

$$
\begin{aligned}
&-\frac{r}{\pi}\cos(2\omega\frac{m}{M})\left\{\left[p_3(\frac{m}{M})+p_2(\frac{m}{M})\cos(\frac{\omega}{r})+p_4(\frac{m}{M})\cos(\frac{\omega}{2r})\right]\left[2\pi-\frac{\omega}{r}\right]\right.\\
&\left.+\,p_6(\frac{m}{M})\sin(\frac{\omega}{r})-2p_4(\frac{m}{M})\sin(\frac{\omega}{2r})\right\},
\end{aligned}
\tag{D.16}
$$

where

$$
\begin{aligned}
p_3(\frac{m}{M}) &= 8\cos^4(\pi\frac{m}{M})-4\cos^2(\pi\frac{m}{M})+\sin^4(\pi\frac{m}{M})=9\cos^4(\pi\frac{m}{M})-6\cos^2(\pi\frac{m}{M})+1\\
p_4(\frac{m}{M}) &= 8\cos^2(\pi\frac{m}{M})\sin^2(\pi\frac{m}{M})=-8\cos^4(\pi\frac{m}{M})+8\cos^2(\pi\frac{m}{M})\\
p_6(\frac{m}{M}) &= -\frac{5}{2}\sin^4(\pi\frac{m}{M})+4\cos^2(\pi\frac{m}{M})\sin^2(\pi\frac{m}{M})=-\frac{13}{2}\cos^4(\pi\frac{m}{M})+9\cos^2(\pi\frac{m}{M})-\frac{5}{2}
\end{aligned}
$$

From (D.12) a closed-form expression for the second term in (D.14) is equal to

$$
\begin{aligned}
&\frac{4}{\pi}\sin(2\omega\frac{m}{M})\left\{-2\cos^3(\pi\frac{m}{M})\sin(\pi\frac{m}{M})\left[4r\sin(\frac{\omega}{2r})\right]\right.\\
&\left.+\,2\cos(\pi\frac{m}{M})\sin^3(\pi\frac{m}{M})\left[-\frac{4r}{3}\sin(\frac{\omega}{r})+\frac{4r}{3}\sin(\frac{\omega}{2r})\right]\right\}.
\end{aligned}
\tag{D.17}
$$

Intermediate calculations can be found in Section D.3, equations (D.26). After rear-

ranging the terms, (D.17) can be written as

$$-\frac{r}{\pi}\sin(2\omega\frac{m}{M})\left\{p_7(\frac{m}{M})\sin(\frac{\omega}{r})+p_8(\frac{m}{M})\sin(\frac{\omega}{2r})\right\}, \tag{D.18}$$

where

$$\begin{aligned}
p_7(\frac{m}{M}) &= \frac{32}{3}\cos(\pi\frac{m}{M})\sin^3(\pi\frac{m}{M}) = \frac{32}{3}\sin(\pi\frac{m}{M})(-\cos^3(\pi\frac{m}{M})+\cos(\pi\frac{m}{M})) \\
p_8(\frac{m}{M}) &= 32\cos^3(\pi\frac{m}{M})\sin(\pi\frac{m}{M}) - \frac{32}{3}\cos(\pi\frac{m}{M})\sin^3(\pi\frac{m}{M}) \\
&= \frac{32}{3}\sin(\pi\frac{m}{M})(4\cos^3(\pi\frac{m}{M})-\cos(\pi\frac{m}{M}))
\end{aligned}$$

A closed-form expression for the $\frac{2}{\pi}$ times the integral on the right hand side of (D.1) is then obtained after summing (D.8), (D.16) and (D.18). This expression is valid for $0 \leq \omega \leq 2r\pi$. The absolute value of ω is taken so the expression is valid for $|\omega| < 2r\pi$.

D.2

In this Section a closed-form expression for the magnitude squared in the term on the right hand side of (D.1) is derived. As in Section D.1 it is assumed that $r \leq 0.5$, $0 \leq \omega \leq 2r\pi$ and an ideal high-pass filter is used. First, consider $H(e^{j\omega}; \frac{m}{M}T) \otimes H(e^{j\omega}; \frac{m}{M}T)$, which is equal to

$$\begin{aligned}
&\frac{1}{2\pi}\int_{-\pi}^{\pi} H(e^{j\theta};\frac{m}{M}T)H(e^{j(\omega-\theta)};\frac{m}{M}T)d\theta \\
&= \frac{1}{2\pi}\int_{(1-r)\pi+\omega}^{(1+r)\pi} e^{j\omega\frac{m}{M}}\left[\cos(\pi\frac{m}{M})-j\sin(\pi\frac{m}{M})f_1(\theta;r)\right]\left[\cos(\pi\frac{m}{M})-j\sin(\pi\frac{m}{M})f_2(\omega-\theta;r)\right]d\theta
\end{aligned} \tag{D.19}$$

where $f_1(\theta;r) = \sin(\frac{\pi}{2r}(\frac{\theta}{\pi} - 1))$ and $f_2(\omega - \theta; r) = \sin(\frac{\pi}{2r}(\frac{\omega-\theta}{\pi} + 1))$. It can be shown that a closed-form expression for $H(e^{j\omega}; \frac{m}{M}T) \otimes H(e^{j\omega}; \frac{m}{M}T)$ is equal to

$$\frac{e^{j\omega\frac{m}{M}}}{2\pi}\left\{\cos^2(\pi\frac{m}{M})[2r\pi - \omega] - j4r\cos(\pi\frac{m}{M})\sin(\pi\frac{m}{M})\sin(\frac{\omega}{2r})\right.$$
$$\left. - \sin^2(\pi\frac{m}{M})\left[r\sin(\frac{\omega}{2r}) - \frac{1}{2}\cos(\frac{\omega}{2r})(2r\pi - \omega)\right]\right\}. \quad \text{(D.20)}$$

Intermediate calculations to derive (D.20) from (D.19) can be found in Section D.3, Equations (D.25) and (D.26). $H(e^{j\omega}; \frac{m}{M}T) \otimes H(e^{j\omega}; \frac{m}{M}T)$ can be denoted $\frac{e^{j\omega\frac{m}{M}}}{2\pi}\{D_1(\frac{m}{M};\theta,\omega,r) - jD_2(\frac{m}{M};\theta,\omega,r)\}$, where from (D.20)

$$D_1(\frac{m}{M};\theta,\omega,r) = \left[\cos^2(\pi\frac{m}{M}) + \frac{1}{2}\sin^2(\pi\frac{m}{M})\cos(\frac{\omega}{2r})\right][2r\pi - \omega] - \sin^2(\pi\frac{m}{M})r\sin(\frac{\omega}{2r})$$
$$D_2(\frac{m}{M};\theta,\omega,r) = 4r\cos(\pi\frac{m}{M})\sin(\pi\frac{m}{M})\sin(\frac{\omega}{2r}). \quad \text{(D.21)}$$

It can be shown using (D.20) that $H(e^{j\omega}; -\frac{m}{M}T) \otimes H(e^{j\omega}; -\frac{m}{M}T) = \frac{e^{-j\omega\frac{m}{M}}}{2\pi}\{D_1(\frac{m}{M};\theta,\omega,r) + jD_2(\frac{m}{M};\theta,\omega,r)\}$, yielding

$$|H(e^{j\omega}; \frac{m}{M}T) \otimes H(e^{j\omega}; \frac{m}{M}T) - H(e^{j\omega}; -\frac{m}{M}T) \otimes H(e^{j\omega}; -\frac{m}{M}T)|^2$$
$$= |\frac{1}{2\pi}(e^{j\omega\frac{m}{M}} - e^{-j\omega\frac{m}{M}})D_1(\frac{m}{M};\theta,\omega,r) - \frac{j}{2\pi}(e^{j\omega\frac{m}{M}} + e^{-j\omega\frac{m}{M}})D_2(\frac{m}{M};\theta,\omega,r)|^2$$
$$= |\frac{2j}{2\pi}\sin(\omega\frac{m}{M})D_1(\frac{m}{M};\theta,\omega,r) - \frac{2j}{2\pi}\cos(\omega\frac{m}{M})D_2(\frac{m}{M};\theta,\omega,r)|^2$$
$$= \frac{1}{\pi^2}\{\sin(\omega\frac{m}{M})D_1(\frac{m}{M};\theta,\omega,r) - \cos(\omega\frac{m}{M})D_2(\frac{m}{M};\theta,\omega,r)\}^2$$
$$= \frac{1}{\pi^2}\left\{\sin(\omega\frac{m}{M})\left[\left[\cos^2(\pi\frac{m}{M}) + \frac{1}{2}\sin^2(\pi\frac{m}{M})\cos(\frac{\omega}{2r})\right][2r\pi - \omega] - \sin^2(\pi\frac{m}{M})r\sin(\frac{\omega}{2r})\right]\right.$$
$$\left. - \cos(\omega\frac{m}{M})4r\cos(\pi\frac{m}{M})\sin(\pi\frac{m}{M})\sin(\frac{\omega}{2r})\right\}^2 \quad \text{(D.22)}$$

The trigonometric identities $e^{j\omega\frac{m}{M}} - e^{-j\omega\frac{m}{M}} = 2j\sin(\omega\frac{m}{M})$ and $e^{j\omega\frac{m}{M}} + e^{-j\omega\frac{m}{M}} = 2\cos(\omega\frac{m}{M})$ were used to obtain (D.22). After rearranging the terms in (D.22) a closed-form expression for the magnitude squared in the term on the right hand side of (D.1)

is given by

$$\frac{1}{\pi^2}\left\{\left[p_9(\frac{m}{M})+p_{10}(\frac{m}{M})\cos(\frac{\omega}{2r})\right][2r\pi-\omega]\sin(\omega\frac{m}{M})\right.$$
$$\left.-\left[2p_{10}(\frac{m}{M})\sin(\omega\frac{m}{M})+p_{11}(\frac{m}{M})\cos(\omega\frac{m}{M})\right]r\sin(\frac{\omega}{2r})\right\}^2, \tag{D.23}$$

where

$$p_9(\frac{m}{M})=\cos^2(\pi\frac{m}{M})$$
$$p_{10}(\frac{m}{M})=\frac{1}{2}\sin^2(\pi\frac{m}{M})=-\frac{1}{2}\cos^2(\pi\frac{m}{M})+\frac{1}{2}$$
$$p_{11}(\frac{m}{M})=4\cos(\pi\frac{m}{M})\sin(\pi\frac{m}{M}).$$

This expression is valid for $0\leq\omega\leq 2r\pi$. The absolute value of ω has to be taken to make this expression valid for $|\omega|<2r\pi$.

D.3

This Section contains intermediate calculations for Sections D.1 and D.2.

$$\int_{(1-r)\pi+\omega}^{(1+r)\pi}\cos(\frac{\pi}{r}(\frac{\theta}{\pi}-1))d\theta=r\left[\sin(\frac{\pi}{r}(\frac{\theta}{\pi}-1))\right]_{(1-r)\pi+\omega}^{(1+r)\pi}$$
$$=r\sin(\frac{\omega}{r}).$$
$$\int_{(1-r)\pi+\omega}^{(1+r)\pi}\cos(\frac{\pi}{r}(\frac{(\omega-\theta)}{\pi}+1))d\theta\overset{(\alpha=\omega-\theta+2\pi)}{=}-\int_{(1+r)\pi}^{(1-r)\pi+\omega}\cos(\frac{\pi}{r}(\frac{\alpha-2\pi}{\pi}+1))d\alpha$$
$$=\int_{(1-r)\pi+\omega}^{(1+r)\pi}\cos(\frac{\pi}{r}(\frac{\theta}{\pi}-1))d\theta.$$
$$\int_{(1-r)\pi+\omega}^{(1+r)\pi}\cos(\frac{\pi}{r}(\frac{(\omega-2\theta)}{\pi}+2))d\theta=\left[-\frac{r}{2}\sin(\frac{\pi}{r}(\frac{(\omega-2\theta)}{\pi}+2))\right]_{(1-r)\pi+\omega}^{(1+r)\pi}$$
$$=-r\sin(\frac{\omega}{r}) \tag{D.24}$$

The integrals in (D.24) are used to obtain (D.7).

Using the trigonometric identities $\sin^2(a)=\frac{1}{2}-\frac{1}{2}\cos(2a)$ and $\cos(a)\cos(b)=$

$\frac{1}{2}(\cos(a+b)+\cos(a-b))$ and the integrals in (D.24), it is found that

$$\int_{(1-r)\pi+\omega}^{(1+r)\pi} f_1^2(\theta;r)d\theta = \int_{(1-r)\pi+\omega}^{(1+r)\pi} f_2^2(\omega-\theta;r)d\theta = \frac{1}{2}\left[2r\pi-\omega-r\sin(\frac{\omega}{r})\right]$$

$$\int_{(1-r)\pi+\omega}^{(1+r)\pi} f_1^2(\theta;r)f_2^2(\omega-\theta;r)d\theta = \frac{1}{4}[2r\pi-\omega][1+\frac{1}{2}\cos(\frac{\omega}{r})] - \frac{5r}{8}\sin(\frac{\omega}{r})$$

$$\begin{aligned}
\int_{(1-r)\pi+\omega}^{(1+r)\pi} f_1(\theta;r)f_2(\omega-\theta;r)d\theta &= \int_{(1-r)\pi+\omega}^{(1+r)\pi} \sin(\frac{\pi}{2r}(\frac{\theta}{\pi}-1))\sin(\frac{\pi}{2r}(\frac{(\omega-\theta)}{\pi}+1))d\theta \\
&= \frac{1}{2}\int_{(1-r)\pi+\omega}^{(1+r)\pi} \cos(\frac{\pi}{2r}(\frac{\omega-2\theta}{\pi}+2))d\theta - \frac{1}{2}\int_{(1-r)\pi+\omega}^{(1+r)\pi}\cos(\frac{\omega}{2r})d\theta \\
&= \frac{1}{2}\left[-r\sin(\frac{\pi}{2r}(\frac{\omega-2\theta}{\pi}+2))\right]_{(1-r)\pi+\omega}^{(1+r)\pi} \\
&= r\sin(\frac{\omega}{2r}) - \frac{1}{2}\cos(\frac{\omega}{2r})(2r\pi-\omega), \qquad \text{(D.25)}
\end{aligned}$$

where $f_1(\theta;r)=\sin(\frac{\pi}{2r}(\frac{\theta}{\pi}-1))$ and $f_2(\omega-\theta;r)=\sin(\frac{\pi}{2r}(\frac{\omega-\theta}{\pi}+1))$. The integrals in (D.25) are used to obtain (D.15) and (D.20).

Using the trigonometric identities $\sin^2(a)=\frac{1}{2}-\frac{1}{2}\cos(2a)$, $\sin(a)\cos(b)=\frac{1}{2}(\sin(a+b)+\sin(a-b))$ and $\cos(a)\sin(b)=\frac{1}{2}(\sin(a+b)-\sin(a-b))$, it is found that

$$\begin{aligned}
\int_{(1-r)\pi+\omega}^{(1+r)\pi} f_1(\theta;r)d\theta &= -2r\left[\cos(\frac{\pi}{2r}(\frac{\theta}{\pi}-1))\right]_{(1-r)\pi+\omega}^{(1+r)\pi} \\
&= 2r\sin(\frac{\omega}{2r}) \\
\int_{(1-r)\pi+\omega}^{(1+r)\pi} f_2(\omega-\theta;r)d\theta &\overset{(\alpha=\omega-\theta+2\pi)}{=} -\int_{(1+r)\pi}^{(1-r)\pi+\omega} f_2(\alpha-2\pi;r)d\alpha \\
&= \int_{(1-r)\pi+\omega}^{(1+r)\pi} f_1(\theta;r)d\theta
\end{aligned}$$

$$
\begin{aligned}
f_1(\theta;r)f_2^2(\omega-\theta;r) &= \frac{1}{2}\sin(\frac{\pi}{2r}(\frac{\theta}{\pi}-1))\left[1-\cos(\frac{\pi}{r}(\frac{\omega-\theta}{\pi}+1))\right] \\
&= \frac{1}{2}f_1(\theta;r) - \frac{1}{4}\sin(\frac{\pi}{2r}(\frac{2\omega-\theta}{\pi}+1)) + \frac{1}{4}\sin(\frac{\pi}{2r}(\frac{2\omega-3\theta}{\pi}+3)) \\
\int_{(1-r)\pi+\omega}^{(1+r)\pi} f_1(\theta;r)f_2^2(\omega-\theta;r)d\theta &= r\sin(\frac{\omega}{2r}) - \frac{r}{2}\left[\cos(\frac{\pi}{2r}(\frac{2\omega-\theta}{\pi}+1))\right]_{(1-r)\pi+\omega}^{(1+r)\pi} \\
&\quad + \frac{r}{6}\left[\cos(\frac{\pi}{2r}(\frac{2\omega-3\theta}{\pi}+3))\right]_{(1-r)\pi+\omega}^{(1+r)\pi} \\
&= r\sin(\frac{\omega}{2r}) - \frac{r}{2}\left[\sin(\frac{\omega}{r})+\sin(\frac{\omega}{2r})\right] + \frac{r}{6}\left[-\sin(\frac{\omega}{r})+\sin(\frac{\omega}{2r})\right] \\
&= -\frac{2r}{3}\sin(\frac{\omega}{r}) + \frac{2r}{3}\sin(\frac{\omega}{2r}) \\
f_1^2(\theta;r)f_2(\omega-\theta;r) &= \frac{1}{2}\sin(\frac{\pi}{2r}(\frac{\omega-\theta}{\pi}+1))\left[1-\cos(\frac{\pi}{r}(\frac{\theta}{\pi}-1))\right] \\
&= \frac{1}{2}f_2(\omega-\theta;r) - \frac{1}{4}\sin(\frac{\pi}{2r}(\frac{\omega+\theta}{\pi}-1)) \\
&\quad - \frac{1}{4}\sin(\frac{\pi}{2r}(\frac{\omega-3\theta}{\pi}+3))
\end{aligned}
$$

$$
\begin{aligned}
\int_{(1-r)\pi+\omega}^{(1+r)\pi} f_1^2(\theta;r)f_2(\omega-\theta;r)d\theta &= r\sin(\frac{\omega}{2r}) + \frac{r}{2}\left[\cos(\frac{\pi}{2r}(\frac{\omega+\theta}{\pi}-1))\right]_{(1-r)\pi+\omega}^{(1+r)\pi} \\
&\quad - \frac{r}{6}\left[\cos(\frac{\pi}{2r}(\frac{\omega-3\theta}{\pi}+3))\right]_{(1-r)\pi+\omega}^{(1+r)\pi} \\
&= r\sin(\frac{\omega}{2r}) - \frac{r}{2}\left[\sin(\frac{\omega}{r})+\sin(\frac{\omega}{2r})\right] + \frac{r}{6}\left[-\sin(\frac{\omega}{r})+\sin(\frac{\omega}{2r})\right] \\
&= \int_{(1-r)\pi+\omega}^{(1+r)\pi} f_1(\theta;r)f_2^2(\omega-\theta;r)d\theta, \qquad \text{(D.26)}
\end{aligned}
$$

where $f_1(\theta;r) = \sin(\frac{\pi}{2r}(\frac{\theta}{\pi}-1))$ and $f_2(\omega-\theta;r) = \sin(\frac{\pi}{2r}(\frac{\omega-\theta}{\pi}+1))$. The integrals in (D.26) are used to obtain (D.17) and (D.20).

E.

Noise bandwidth expression for third order loop

A partial fraction expansion of $H_3(z)$ yields

$$H_3(z) = \frac{c_{11}}{z - p_2} + \frac{c_{12}}{(z - p_2)^2} + \frac{c_{21}}{z - p_1}, \tag{E.1}$$

where $c_{11} = \dfrac{G_L(1-a)^2(p_2 - 2p_1)}{(p_2 - p_1)^2}$, $c_{12} = \dfrac{G_L(1-a)^2 p_2^2}{(p_2 - p_1)}$, and $c_{21} = \dfrac{G_L(1-a)^2 p_1^2}{(p_2 - p_1)^2}$.

From (E.1) and using the z-transform pairs $A^{k-1}u[k-1] \longleftrightarrow \dfrac{1}{(z-A)}$ and $(k-1)A^k u[k-1] \longleftrightarrow \dfrac{A^2}{(z-A)}$, it is found that

$$h_3[k] = \frac{G_L(1-a)^2}{p_2 - p_1}\left[\left(\frac{p_1}{p_1 - p_2} + k\right)p_2^k + \frac{p_1}{p_2 - p_1}p_1^k\right]u[k-1]. \tag{E.2}$$

The noise bandwidth, B_L, is given by

$$B_L = \frac{1}{2}\sum_{k=-\infty}^{+\infty} h_3^2[k]. \tag{E.3}$$

Using the geometric series $\displaystyle\sum_{k=1}^{+\infty} A^k = \frac{A}{1-A}$, $\displaystyle\sum_{k=1}^{+\infty} kA^k = \frac{a}{(1-a)^2}$ and $\displaystyle\sum_{k=1}^{+\infty} k^2 A^k =$

$\frac{a(a+1)}{(1-a)^3}$ and substituting (E.2) into (E.3) gives

$$B_L = \frac{1}{2}\frac{G_L^2(1-a)^4}{(p_2-p_1)^2}\left[\frac{p_1^2}{(p_1-p_2)^2}\left(\frac{p_2^2}{1-p_2^2}+\frac{p_1^2}{1-p_1^2}-2\frac{p_1p_2}{1-p_1p_2}\right)\right.$$
$$+\frac{2p_1}{p_1-p_2}\left(\frac{p_2^2}{(1-p_2^2)^2}-\frac{p_1p_2}{(1-p_1p_2)^2}\right)$$
$$\left.+\frac{p_2^2(1+p_2^2)}{(1-p_2^2)^3}\right]. \tag{E.4}$$

F.

PSD Derivation of the Gardner detector's noise

The low-pass equivalent of the bandpass QAM signal is given by

$$x(t) = \sum_{l=-\infty}^{+\infty} (a[l] + jb[l])h(t - lT - \varepsilon T), \tag{F.1}$$

where $a[l] + j \times b[l]$ are the transmitted symbols that are uniformly distributed across the alphabet with variance $2\sigma_d^2$ where $\sigma_d^2 = E\{a^2[l]\} = E\{b^2[l]\}$, $h(t)$ is the square-root raised cosine signaling pulse, T is the symbol interval, and εT is the timing offset.

The symbol energy of $x(t)$ is $2\sigma_d^2$, since $\int h^2(t)dt = 1$. The symbol energy, E_s, of the bandpass QAM signal is then $E_s = \sigma_d^2$.

The transmit signal is corrupted with bandpass white Gaussian noise, whose low-pass equivalent is denoted by $w(t) = w_I(t) + j \times w_Q(t)$, where $w_I(t)$ and $w_Q(t)$ are the real and imaginary components, each with variance $\sigma_{w_I}^2 = \sigma_{w_Q}^2 = \sigma_w^2/2$. The constant power spectral density of the low-pass equivalent noise is $2N_0$. It is assumed that $x(t)$ is bandlimited to $\pm 1/(2T_s)$ before being sampled at $1/T_s$, so $\sigma_{w_I}^2 = \sigma_{w_Q}^2 = N_0/T_s$.

The PSD is derived in the case of zero timing offset (i.e. $\varepsilon T = 0$). The Gardner detector operates on a signal that is sampled at twice the symbol rate, $1/T$, so the digital signal that is fed to the Gardner detector (assuming perfect timing) is given

by

$$y[n](\equiv y(nT_s)) = x[n] \otimes h[n] \otimes g[n] + w[n] \otimes h[n] \otimes g[n]$$
$$= \sum_{l=-\infty}^{+\infty} (a[l] + jb[l])p[n-2l] + w[n] \otimes q[n], \tag{F.2}$$

where $h[n]$ is the square-root raised cosine impulse response, h(t), sampled at $2/T$, $g[n]$ is the impulse response of the prefilter given by

$$g[n] = (h[n] \otimes h[n]) \times \cos(\pi n), \tag{F.3}$$

$\otimes$ is the convolution operator, $p[n] = h[n] \otimes h[n] \otimes g[n]$, and $q[n] = h[n] \otimes g[n]$. The prefilter is a high-pass version of the raised cosine prefilter (i.e. cascade of two square-root raised cosine filters), and is obtained by modulating the raised cosine impulse response, $h[n] \otimes h[n]$, by $\cos(\pi n)$. $p[n]$ is the digital impulse response of the end-to-end filter resulting from cascading both matched filters with the prefilter. $q[n]$ is the digital impulse response of the end-to-end filter resulting from cascading one matched filter, the one in the receiver, with the prefilter. Frequency responses of filters with impulse responses $p[n]$ and $q[n]$ can be found in Appendix G.

The Gardner detector produces timing estimates at the symbol rate. With $n = 2k$ (only keep the detector's output with even indices), the timing estimates, which are denoted by $z[2k] \equiv z(2kT_s)$, are given by

$$z[2k] = \mathcal{R}e\left\{y[2k-1] \times [y[2k] - y[2k-2]]^*\right\}, \tag{F.4}$$

where $2kT_s$ and $(2k-2)T_s$ are the correct sampling times (i.e. eye is maximally opened) for detecting transmitted symbols k and $k-1$, $y[2k] \equiv y(2KT_s)$ and $y[2k-2]$ are complex decision variables, $y[2k-1]$ is the sample between $y[2k]$ and $y[2k-2]$, "*" denotes the complex conjugate operator, and $\mathcal{R}\{\cdot\}$ represents the real part. Since

$T = 2T_s$, (F.4) can be also be written as

$$z(kT) = \mathcal{R}e\left\{y((k-1/2)T) \times [y(kT) - y((k-1)T)]^*\right\}. \tag{F.5}$$

From (F.2) $y((k-\Delta)T), \Delta = \{0, 1/2, 1\}$ can be expressed as

$$y((k-\Delta)T) = s_{k-\Delta} + \eta_{k-\Delta}, \tag{F.6}$$

where

$$\begin{aligned} s_{k-\Delta} &= \sum_{l=-\infty}^{+\infty} (a[l] + jb[l])p((k-\Delta-l)T),\ \Delta = \{0, 1/2, 1\}, \\ \eta_{k-\Delta} &= \sum_{l=-\infty}^{+\infty} w_{2l}q((k-\Delta-l)T) + w_{2l+1}q((k-\Delta-1/2-l)T), \end{aligned} \tag{F.7}$$

where $p(t)$ is the underlying continuous-time signal of $p[n]$, $q(t)$ is the underlying continuous-time signal of $q[n]$, $w_{2l} \equiv w(2lT_s)$, and $w_{2l+1} \equiv w((2l+1)T_s)$.

In the case of perfect timing the mid-samples are zero, and $s_{k-1/2} = 0$. From (F.5) and (F.7) the Gardner's detector output reduces to

$$z(kT) = \mathcal{R}e\left\{\eta_{k-1/2} \times [s_k - s_{k-1} + \eta_k - \eta_{k-1}]^*\right\}. \tag{F.8}$$

This expression is rewritten in the form $z(kT) = z_I(kT) + z_Q(kT)$, where

$$\begin{aligned} z_I(kT) &= \eta_{I,k-1/2} \times [s_{I,k} - s_{I,k-1} + \eta_{I,k} - \eta_{I,k-1}], \\ z_Q(kT) &= \eta_{Q,k-1/2} \times [s_{Q,k} - s_{Q,k-1} + \eta_{Q,k} - \eta_{Q,k-1}], \end{aligned} \tag{F.9}$$

by decomposing s_k into its real part, $s_{I,k}$, and its imaginary part, $s_{Q,k}$, and decomposing η_k into its real part, $\eta_{I,k}$, and its imaginary part, $\eta_{Q,k}$.

The sequences, $a[l]$ and $b[l]$ are independent, zero-mean, and with equal variance, σ_d^2. The Gaussian noise is independent of the data. Under these conditions the terms $z_I(kT)$ and $z_Q(kT)$ are independent with equal variance. Their power spectral

densities, respectively denoted by $S_{z_I}(e^{j\Omega T})$ and $S_{z_Q}(e^{j\Omega T})$, are identical, and the power spectral density, $S(e^{j\Omega T})$, is simply equal to

$$\begin{aligned} S(e^{j\Omega T}) &= S_{z_I}(e^{j\Omega T}) + S_{z_Q}(e^{j\Omega T}) \\ &= 2 \times S_{z_I}(e^{j\Omega T}). \end{aligned} \tag{F.10}$$

As in Section 2.5, an expression for $S_{z_I}(e^{j\Omega T})$ is derived by evaluating an ensemble average in the frequency domain. This ensemble average is given by

$$S_{z_I}(e^{j\Omega T}) = \lim_{N \to +\infty} \frac{1}{2N+1} E\left\{ |Z_I^t(e^{j\Omega T})|^2 \right\}, \tag{F.11}$$

where $E\{\cdot\}$ denotes the expectation operator, $Z_I^t(e^{j\Omega T})$ is the Discrete Time Fourier Transform (DTFT) of $z_I^t(kT)$, and $z_I^t(kT)$ is $z_I(kT)$ truncated to $2N+1$ symbols. "Truncation to $2N+1$ symbols" means that the infinite sums in (F.7) are replaced by finite sums from $-N$ to $+N$. We have from (F.9)

$$Z_I^t(e^{j\Omega T}) = \mathrm{DTFT}\left\{\eta_{\mathrm{I,k-1/2}}^{\mathrm{t}}\right\} \otimes \left[\mathrm{DTFT}\left\{\mathrm{s}_{\mathrm{I,k}}^{\mathrm{t}} - \mathrm{s}_{\mathrm{I,k-1}}^{\mathrm{t}}\right\} + \mathrm{DTFT}\left\{\eta_{\mathrm{I,k}}^{\mathrm{t}} - \eta_{\mathrm{I,k-1}}^{\mathrm{t}}\right\}\right],$$

where

$$\mathrm{DTFT}\left\{\eta_{\mathrm{I,k-1/2}}^{\mathrm{t}}\right\} = \sum_{l=-N}^{+N} \left[w_{I,2l} Q(e^{j\Omega T}; \frac{T}{2}) e^{-j\Omega T l} + w_{I,2l+1} Q(e^{j\Omega T}; 0) e^{-j\Omega T(l+1)} \right],$$

$$Q(e^{j\Omega T}; \Delta T) = \mathrm{DTFT}\left\{\mathrm{q((k-\Delta)T)}\right\}, \ \Delta = \{0, 1/2\},$$

$$\mathrm{DTFT}\left\{\mathrm{s}_{\mathrm{I,k}}^{\mathrm{t}} - \mathrm{s}_{\mathrm{I,k-1}}^{\mathrm{t}}\right\} = \sum_{l=-N}^{+N} a[l] P(e^{j\Omega T}) \left[e^{-j\Omega T l} - e^{-j\Omega T(l+1)}\right],$$

$$P(e^{j\Omega T}) = \mathrm{DTFT}\left\{\mathrm{p(kT)}\right\},$$

$$\text{DTFT}\left\{\eta^{\text{t}}_{\text{I,k}} - \eta^{\text{t}}_{\text{I,k}-1}\right\} = \sum_{l=-N}^{+N}\Big[w_{I,2l}Q(e^{j\Omega T};0)\left(e^{-j\Omega Tl} - e^{-j\Omega T(l+1)}\right) + w_{I,2l+1}Q(e^{j\Omega T};\frac{T}{2})\left(e^{-j\Omega Tl} - e^{-j\Omega T(l+1)}\right)\Big].$$

Since $|Z^t_I(e^{j\Omega T})|^2 = Z^t_I(e^{j\Omega T})(Z^t_I(e^{j\Omega T}))^*$, then $S_z(e^{j\Omega T})$ is given by

$$\begin{aligned}
&\lim_{N\to+\infty}\frac{2}{2N+1}E\left\{\frac{1}{4\pi^2}\int_{-\pi}^{\pi}\sum_{l=-N}^{N}\left[e^{-j\theta_1 l} - e^{-j\theta_1(l+1)}\right]\right.\\
&\times\left[a[l]P(e^{j\theta_1}) + w_{I,2l}Q(e^{j\theta_1};0) + w_{I,2l+1}Q(e^{j\theta_1};\frac{T}{2})\right]\\
&\times\sum_{k=-N}^{N}\left[w_{I,2k}Q(e^{j(\Omega T-\theta_1)};\frac{T}{2})e^{-j(\Omega T-\theta_1)k} + w_{I,2k+1}Q(e^{j(\Omega T-\theta_1)};0)e^{-j(\Omega T-\theta_1)(k+1)}\right]d\theta_1\\
&\times\int_{-\pi}^{\pi}\sum_{m=-N}^{N}\left[e^{j\theta_2 m} - e^{j\theta_2(m+1)}\right]\left[a[m]P^*(e^{j\theta_2}) + w_{I,2m}Q^*(e^{j\theta_2};0) + w_{I,2m+1}Q^*(e^{j\theta_2};\frac{T}{2})\right]\\
&\times\left.\sum_{n=-N}^{N}\left[w_{I,2n}Q^*(e^{j(\Omega T-\theta_2)};\frac{T}{2})e^{j(\Omega T-\theta_2)n} + w_{I,2n+1}Q^*(e^{j(\Omega T-\theta_2)};0)e^{-j(\Omega T-\theta_2)(n+1)}\right]d\theta_2\right\}.
\end{aligned}\tag{F.12}$$

After extensive algebraic manipulations (F.12) reduces to

$$S(e^{j\Omega T}) = S_z^{s\times n}(e^{j\Omega T}) + S_z^{n\times n}(e^{j\Omega T}),$$

where

$$\begin{aligned}
S_z^{s\times n}(e^{j\Omega T}) &= \frac{\sigma_d^2\times\sigma_{wI}^2}{\pi}\int_{-\pi}^{\pi}(2-2\cos\theta)|P(e^{j\theta})|^2\left(|Q(e^{j(\Omega T-\theta)};\frac{T}{2})|^2 + |Q(e^{j(\Omega T-\theta)};0)|^2\right)d\theta,\\
S_z^{n\times n}(e^{j\Omega T}) &= S_z^{n_1^2}(e^{j\Omega T}) + S_z^{n_2^2}(e^{j\Omega T}) + S_z^{n_3^2}(e^{j\Omega T}),
\end{aligned}\tag{F.13}$$

with

$$S_z^{n_1^2}(e^{j\Omega T}) = 4\pi\sigma_{w_I}^4 \Big| Q(e^{j\Omega T};0)(1-e^{-j\Omega T}) \otimes Q(e^{j\Omega T};\frac{T}{2}) + Q(e^{j\Omega T};\frac{T}{2})(1-e^{-j\Omega T}) \otimes Q(e^{j\Omega T};0)e^{-j\Omega T} \Big|^2 \delta(\Omega T),$$

$$S_z^{n_2^2}(e^{j\Omega T}) = 8\sigma_{w_I}^4 \times \mathcal{I}m\left\{ Q(e^{j\Omega T};0)Q^*(e^{j\Omega T};\frac{T}{2})(1-e^{j\Omega T}) \right\} \otimes \mathcal{I}m\left\{ Q(e^{j\Omega T};0)Q^*(e^{j\Omega T};\frac{T}{2})(1-e^{j\Omega T}) \right\},$$

$$S_z^{n_3^2}(e^{j\Omega T}) = 4\sigma_{w_I}^4 \left([1-\cos\Omega T][|Q(e^{j\Omega T};0)|^2 + |Q(e^{j\Omega T};\frac{T}{2})|^2] \right) \otimes \left(|Q(e^{j\Omega T};0)|^2 + |Q(e^{j\Omega T};\frac{T}{2})|^2 \right),$$

where $\mathcal{I}m\{\cdot\}$ returns the imaginary part of its argument, and $\delta(\cdot)$ is the Dirac function.

Note that $S_z^{s\times n}(e^{j\Omega T})$ is the power spectrum of the signal times noise component, and $S_z^{n\times n}(e^{j\Omega T})$ is the power spectrum of the noise times noise component.

Equation (F.13) is further simplified by evaluating $P(e^{j\Omega T})$, $Q(e^{j\Omega T};T/2)$, and $Q(e^{j\Omega T};0)$.

The DTFT of $p[n]$, where the sampling rate is $2/T$, is given by (G.4). $P(e^{j\Omega T})$ is the DTFT of $p[n]$ after it has been down-sampled by 2 and is given by [61]

$$P(e^{j\Omega T}) = \frac{1}{2}\left(P\left(e^{j\omega/2}\right) + P\left(e^{j(\omega-2\pi)/2}\right)\right)|_{\omega=\Omega T}\,. \tag{F.14}$$

so from (G.4) with $(1-r)\pi < \Omega T < (1+r)\pi$

$$\begin{aligned} P(e^{j\Omega T}) &= \frac{1}{2}\left(\cos^2\left(\frac{1}{r}\left(\frac{\Omega T}{2}-\frac{\pi}{2}\right)\right)+\cos^2\left(\frac{1}{r}\left(\frac{2\pi-\Omega T}{2}-\frac{\pi}{2}\right)\right)\right) \\ &= \cos^2\left(\frac{\pi}{2r}\left(\frac{\Omega T}{\pi}-1\right)\right), \end{aligned} \tag{F.15}$$

and

$$P(e^{j\Omega T}) = \begin{cases} 0, & -(1-r)\pi \le \Omega T \le (1-r)\pi, \\ \cos^2\left(\frac{\pi}{2r}\left(\frac{\Omega T}{\pi}-1\right)\right), & (1-r)\pi < \Omega T < (1+r)\pi. \end{cases} \tag{F.16}$$

The DTFT of $q[n]$ denoted by $Q(e^{j\omega})$, where $\omega = \Omega\frac{T}{2}$, is determined using (G.2) and (G.3) to find

$$Q(e^{j\omega}) = \begin{cases} 0, & |\omega| \le (1-r)\frac{\pi}{2}, \\ \sqrt{\left[1+\cos\left(\frac{\pi}{2r}\left(\frac{|2\omega|}{\pi}+r-1\right)\right)\right]} & \\ \times\left[1+\cos\left(\frac{\pi}{2r}\left(\frac{|2\omega|}{\pi}-r-1\right)\right)\right], & (1-r)\frac{\pi}{2} \le |\omega| \le (1+r)\frac{\pi}{2}, \\ 0, & (1+r)\frac{\pi}{2} \le |\omega| < \pi. \end{cases} \tag{F.17}$$

$Q(e^{j\Omega T})$ is the DTFT of $q[n]$ after it has been down-sampled by 2 and is given by [61]

$$Q(e^{j\Omega T}) = \frac{1}{2}\left(Q\left(e^{j\omega/2}\right)+Q\left(e^{j(\omega-2\pi)/2}\right)\right)|_{\omega=\Omega T}. \tag{F.18}$$

So from (F.17) after some simplifications it is found that

$$Q(e^{j\Omega T}) = \begin{cases} 0, & -(1-r)\pi \le \Omega T \le (1-r)\pi, \\ \cos\frac{\Omega T-\pi}{2r}\left(\sqrt{1-\sin\frac{\Omega T-\pi}{2r}}\right. & \\ \left.+\sqrt{1+\sin\frac{\Omega T-\pi}{2r}}\right), & (1-r)\pi < \Omega T < (1+r)\pi. \end{cases} \tag{F.19}$$

Now we have

$$Q(e^{j\Omega T};\frac{T}{2}) = \frac{1}{2}\left(e^{-j\omega/2}Q\left(e^{j\omega/2}\right) - e^{-j\omega/2}Q\left(e^{j(\omega-2\pi)/2}\right)\right)|_{\omega=\Omega T}\,. \tag{F.20}$$

and

$$Q(e^{j\Omega T};\frac{T}{2}) = \begin{cases} 0, & -(1-r)\pi \le \Omega T \le (1-r)\pi, \\ \cos\dfrac{\Omega T-\pi}{2r}\left(\sqrt{1-\sin\dfrac{\Omega T-\pi}{2r}}\right. & \\ \left. -\sqrt{1+\sin\dfrac{\Omega T-\pi}{2r}}\right)e^{-j\Omega T/2}, & (1-r)\pi < \Omega T < (1+r)\pi. \end{cases} \tag{F.21}$$

Equations (F.16), (F.19) and (F.21) are used in (F.13) to yield (4.2).

G.

Derivation of the Gardner detector's S-curve

An equation for the Gardner detector's S-curve that is valid for any band-limited signaling pulse, $p(t)$, is Equation (25) in [16], which reads

$$-2j(\frac{1}{T})\left(e^{j2\pi\varepsilon T/T}\frac{1}{2\pi}\int_0^{2\pi/T} P_A(j\Omega)P_A(j(\frac{2\pi}{T}-\Omega))\sin\frac{\Omega T}{2}d\Omega\right.$$
$$\left.+\ e^{-j2\pi\varepsilon T/T}\frac{1}{2\pi}\int_{-2\pi/T}^{0} P_A(j\Omega)P_A(j(-\frac{2\pi}{T}-\Omega))\sin\frac{\Omega T}{2}d\Omega\right)\times 2\sigma_d^2, \qquad \text{(G.1)}$$

where $P_A(j\Omega)$ is the Fourier transform of $p(t)$, εT is the timing offset, and $2\sigma_d^2$ is the variance of the transmitted symbols, $a[k]+jb[k]$. The signaling pulse $p(t)$ is the impulse response of the end-to-end filter resulting from cascading the matched filters in the transmitter and the receiver as well as the prefilter.

In Appendix F the digital signaling pulse, $p[n]$, was defined as $p[n]=h[n]\otimes h[n]\otimes g[n]$, where $g[n]$ was the impulse response of the prefilter defined in (F.3), and $h[n]$ was the square-root raised cosine impulse response, $h(t)$, that is sampled at $2/T$.

The DTFT of $p[n]$ denoted by $P(e^{j\omega})$, where $\omega=\Omega\frac{T}{2}$, is determined as follows. In this analysis, $h[n]$ is scaled such that $h[n]\otimes h[n]$ yields a discrete impulse response that corresponds to the raised cosine impulse response when it is sampled at $2/T$.

From (B.1) in Appendix B the DTFT of $h[n] \otimes h[n]$ is then given by

$$H(e^{j\omega}) = \begin{cases} 2, & |\omega| \leq (1-r)\frac{\pi}{2}, \\ \left[1 + \cos\left(\frac{\pi}{2r}\left(\frac{|2\omega|}{\pi} + r - 1\right)\right)\right], & (1-r)\frac{\pi}{2} \leq |\omega| \leq (1+r)\frac{\pi}{2}, \\ 0, & (1+r)\frac{\pi}{2} \leq |\omega| < \pi. \end{cases} \quad \text{(G.2)}$$

From (F.3) and (G.2) the DTFT of $g[n]$ is given by

$$G(e^{j\omega}) = \begin{cases} 0, & |\omega| \leq (1-r)\frac{\pi}{2}, \\ \left[1 + \cos\left(\frac{\pi}{2r}\left(\frac{|2\omega|}{\pi} - r - 1\right)\right)\right], & (1-r)\frac{\pi}{2} \leq |\omega| \leq (1+r)\frac{\pi}{2}, \\ 2, & (1+r)\frac{\pi}{2} \leq |\omega| < \pi. \end{cases} \quad \text{(G.3)}$$

The DTFT of $p[n]$ is $P(e^{j\omega}) = H(e^{j\omega})G(e^{j\omega})$. From (G.2) and (G.3) after some simple algebraic manipulations it is found that

$$P(e^{j\omega}) = \begin{cases} 0, & |\omega| \leq (1-r)\frac{\pi}{2}, \\ \cos^2\left(\frac{1}{r}\left(|\omega| - \frac{\pi}{2}\right)\right), & (1-r)\frac{\pi}{2} \leq |\omega| \leq (1+r)\frac{\pi}{2}, \\ 0, & (1+r)\frac{\pi}{2} \leq |\omega| < \pi. \end{cases} \quad \text{(G.4)}$$

The Fourier transform of the continuous-time impulse response, $p(t)$, is required to determine an expression for the Gardner detector S-curve equation using (G.1). The Fourier transform of $p(t)$ is $P_A(j\Omega) = \frac{T}{2}P(e^{j\omega})|_{\omega=\Omega(T/2)}$, and from (G.4)

$$P_A(j\Omega) = \begin{cases} 0, & |\Omega| \leq (1-r)\frac{\pi}{T}, \\ \frac{T}{2}\cos^2\left(\frac{\pi}{2r}\left(\frac{|\Omega T|}{\pi} - 1\right)\right), & (1-r)\frac{\pi}{T} \leq |\Omega| \leq (1+r)\frac{\pi}{T}, \\ 0, & (1+r)\frac{\pi}{T} \leq |\Omega| < \frac{2\pi}{T}. \end{cases} \quad \text{(G.5)}$$

From (G.5),

$$\begin{aligned}
\int_0^{2\pi/T} P_A(j\Omega)P_A(j(\frac{2\pi}{T}-\Omega))\sin\frac{\Omega T}{2}d\Omega &= \int_{(1-r)\pi/T}^{(1+r)\pi/T}\frac{T}{2}\cos^2\left(\frac{\pi}{2r}\left(\frac{\Omega T}{\pi}-1\right)\right)\\
&\quad\times\frac{T}{2}\cos^2\left(\frac{\pi}{2r}\left(1-\frac{\Omega T}{\pi}\right)\right)\sin\frac{\Omega T}{2}d\Omega\\
&= \frac{T^2}{4}\int_{(1-r)\pi/T}^{(1+r)\pi/T}\cos^4\left(\frac{\pi}{2r}\left(\frac{\Omega T}{\pi}-1\right)\right)\sin\frac{\Omega T}{2}d\Omega\\
&= \frac{24\sin\pi r/2}{(64-20r^2+r^4)T},\\
\int_{-2\pi/T}^{0} P_A(j\Omega)P_A(j(-\frac{2\pi}{T}-\Omega))\sin\frac{\Omega T}{2}d\Omega &= -\frac{24\sin\pi r/2}{(64-20r^2+r^4)T}, \qquad \text{(G.6)}
\end{aligned}$$

and from (G.1) the S-curve equation is

$$\begin{aligned}
&-j\frac{24\sin\pi r/2}{\pi(64-20r^2+r^4)}\left(e^{j2\pi\varepsilon T/T}-e^{-j2\pi\varepsilon T/T}\right)\times 2\sigma_d^2\\
&= \frac{96\sigma_d^2\sin\pi r/2}{\pi(64-20r^2+r^4)}\sin\frac{2\pi\varepsilon T}{T}. \qquad \text{(G.7)}
\end{aligned}$$